UNIVERSITY OF CALIFORNIA

Santa Barbara

Heterogenous Inorganic Bond-Breaking Catalysts: Applications in Biomass Conversion and Photochemical Small Molecule Delivery.

A dissertation submitted in partial satisfaction of the

requirements for the degree Doctor of Philosophy

in Chemistry

by

Christopher Michael Bernt

Committee in charge:

Professor Peter C. Ford, Chair

Professor Alison Butler

Professor Trevor W. Hayton

Professor R. Daniel Little

September 2017

The dissertation of Christopher Michael Bernt is approved.

_____

Alison Butler

_____

Trevor W. Hayton

_____

R. Daniel Little

_____

Peter C. Ford, Committee Chair

September 2017

Heterogenous Inorganic Bond-Breaking Catalysts: Applications in Biomass Conversion and Photochemical Small Molecule Uncaging.

ACKNOWLEDGEMENTS

I would like to acknowledge my funding sources during the course of my graduate studies. I would like to thank the UC Regents for the Regents Special Fellowship and the National Science Foundation for funding the Center for Sustainable Use of Renewable Feedstocks (NSF CHE-1240194).

My thanks also go to my fellow Ford Group members and other student researchers during my tenure as a graduate student for being a great group of colleagues and in many cases good friends. In particular, I would like to thank those who also contributed to the research represented in this dissertation: Elizabeth Levy and Peter Burks for all of their effort and input on the carbon disulfide uncaging project, and Giovanni Bottari, Megan Chui, and Jacob Barret for their camaraderie, ideas, and contributions to the biomass conversion research. I would also like to acknowledge my academic mentors, including all of the investigators involved with CenSURF, Katalin Barta for the collaboration and accommodation in the Netherlands, Alexei Iretskii for being himself, and the members of my dissertation committee: Dr. Butler, Dr. Hayton and Dr. Little. I would also like to acknowledge my advisor and mentor, Dr. Ford for all of his help, patience, and guidance.

Of course, I would never have made it to a graduate program, let alone through one without the support and encouragement of my family, especially my parents John and Andrea. Finally, I would like thank Kristine Pacheco, who has stood by my side through this whole process, for helping me push through the tough times and for sharing in the good ones (and I'm glad Hilda was here to help us both out this last year).

VITA OF CHRISTOPHER MICHAEL BERNT

September 2017

Education

2011 - 2017 Ph.D. Chemistry - University of California Santa Barbara
Awards: UC Regents Special Fellow, Center for Sustainable Use of Renewable Feedstocks Fellow, Phi Lambda Upsilon award for academic achievement, Nomination for Excellence in Teaching Award.

2005 - 2011 Post-Baccalaureate Biochemistry - San Francisco State University

1999 - 2003 B.A. Applied Mathematics & B.A. Psychology - Dartmouth College

Research Experience

2011 - (2016) **UC Santa Barbara Department of Chemistry and Biochemistry**
Advisor: Peter C. Ford. Inorganic chemistry, biomass conversion, kinetics, catalysis, photochemistry. Characterization of copper doped porous metal oxide catalysts for lignin disassembly. Used chromatographic product analysis and global fitting of kinetics data to identify kinetic and thermodynamic parameters. Identified primary contributors to product proliferation and generated strategies to increase product selectivity. Developed quantum-dot catalyzed photochemical oxidation of dithiooxalate into carbon disulfide and carbon dioxide.

2005 - 2011 **San Francisco State University Department of Chemistry and Biochemistry** *Advisor: Raymond Esquerra. Biochemistry, enzymology.* Probed ligand rebinding kinetics of nitric oxide synthase mutants and isoforms using flash photolysis and kinetics analysis of three dimensional, time resolved, spectral data.

Publications

First Author

"Mapping relative reactivities for aromatic models of lignin disassembly over Cu-doped porous metal oxides" Christopher M. Bernt, Giovanni Bottari, Jacob Barrett, Susannah L. Scott, Katalin Barta, and Peter C. Ford. *Catalysis Science & Technology,* **2016**, *6,* 2984 – 2994.

"Photocatalytic carbon disulfide production via charge transfer quenching of quantum dots" Christopher M. Bernt, Peter T. Burks, Anthony W. DeMartino, Agustin E. Pierri, Elizabeth S. Levy, David F. Zigler, and Peter C. Ford. *Journal of the American Chemical Society*, **2014**, *136* (6), 2192–2195.

Contributing Author

"Probing the Lignin Disassembly Pathways with Modified Catalysts Based on Cu-Doped Porous Metal Oxides" M. Chui, G. Metzker, C. M. Bernt, A. T. Tran, A. C. B. Burtoloso, P. C. Ford. *ACS Sustainable Chemistry and Engineering*, **2017**, 5, 3158-3169.

"Enhancing Aromatic Production from Reductive Lignin Disassembly: in situ O-methylation of Phenolic Intermediates." Jacob Barrett, Yu Gao, Christopher M. Bernt, Megan Chui, Anthony Tran, Marcus Foston, Peter C. Ford. *ACS Sustainable Chemistry and Engineering*, **2016**, *4*, 6877-6886.

Presentations

Invited Talks

"On the Activation Parameters for Model Lignin Linkages over a Promising Cu-Doped Porous Metal Oxide Catalyst" C M. Bernt, H. Maneesuwan, M. Chui, K. Barta, P. C. Ford., Talk at the 20th Annual ACS Green Chemistry and Engineering Conference, Portland, OR June **2016**

"Understanding and enhancing the selectivity of reductive lignin disassembly over doped porous metal oxides" C. M. Bernt, J. Barrett, M. Chui, G. Bottari, H. Maneesuwan, K. Barta, A. Iretski, S. L. Scott, P. C. Ford., Talk at the 250th ACS National Meeting, Div. of Envr. Chem. Boston, MA August **2015**

Contributed Presentations and Posters

"Exploring the Activation Parameters for Lignin Model Compounds over a Cu-Doped Porous Metal Oxide Catalyst" Poster at 251st ACS National Meeting, *Div. of Catal. Sci. and Tech., San Diego, CA March **2016***

"Probing the mechanism and structure of a lignin reducing copper doped porous metal oxide catalyst" Poster at 248th ACS National Meeting, *Div. of Inorg. Chem., San Francisco, CA August **2014***

"Dithiooxalates as a novel class of photo-cleavable quantum dot surface ligands" C. M. Bernt, P. Burks, E. Levy, P. C. Ford, Presentation at UCSB Chemical Sciences Student Seminar. Santa Barbara, CA Fall **2013**

"CdSe Quantum Dots giving Dithiooxalate a Break" C. M. Bernt, P. Burks, E. Levy, P. C. Ford, Presentation at Southern California Inorganic Photochemistry Conference. Fall **2013**

"Photochemical Release of Carbon Disulfide" C. M. Bernt, P. Burks, P. C. Ford, Presentation at Southern California Inorganic Photochemistry Conference. Fall **2012**

University Teaching Experience

2011-2017 ***UC Santa Barbara***

Teaching Associate: Instructor of record for one quarter of general chemistry lecture (chem 1A). Topics covered atoms and compounds, general chemical reactions, solution and gas stoichiometry, equilibria, acid-base chemistry, and buffers.

Graduate Teaching Assistant: Led four sections of general chemistry (chem 1BL) and two quarters of physical chemistry (chem 116B and chem 116C) labs. Discussion leader for two sections of inorganic chemistry (chem 173B).

Special Program Instructor: Designed and taught a short inquiry-based workshop for both the UCSB School for Scientific Thought and the Summer Institute in Mathematics and Science.

2005-2011 ***San Francisco State University, College of Science and Engineering***

Summer Science Institute: Co-created a program designed to prepare underserved students for the study of health-related sciences. Planned specific lessons and lead a team of other teachers to help design a curriculum for an eight-week program focusing on basic chemistry and mathematics. Taught for two summer sessions and mentored students throughout the school year.

Chemistry Boot Camp: For four summers, designed and taught an intensive three-day general chemistry course to help prepare incoming post-bac students for the rigors of college level chemistry.

Lab courses: Taught nine semesters of general chemistry labs, one semester of organic chemistry and one semester of general biology lab.

Discussion Sections: Prepared and taught lessons for supplemental discussion courses: six semesters in general chemistry and for four in general biology.

Tutoring: Worked as a tutor for the SFSU Math Department. Provided individualized tutoring to undergraduate students of all levels with a specialization in statistics.

Academic Service and Outreach

Graduate Students for Diversity in Science (Hospitality chair 2012-2014) - Organized food and lodging for a graduate student run program to encourage students from under-represented populations to consider graduate school.

Research Internships in Science and Engineering – Mentored undergraduate students during summer research program.

Sci-Trek - Assisted with inquiry-based learning science modules at local elementary schools.

School for Scientific Thought - Re-designed and taught a short course on catalysis and green chemistry to high school students interested in careers in science.

Summer Institute in Mathematics and Science - Designed and taught a short course on catalysis and green chemistry to incoming undergraduate students.

Science as a Career Outreach Program Experiment - Visited local high schools and gave a presentation on my background and research to encourage students to pursue further education in science.

Graduate Student Recruitment – Served on the student committee that assisted in the design and execution of the visitation experience for incoming graduate students.

CenSURF Webmaster – Helped maintain and setup the website for the Center for Sustainable use of Renewable Feedstocks.

ABSTRACT*

Heterogenous Inorganic Bond-Breaking Catalysts: Applications in Biomass Conversion and Photochemical Small Molecule Uncaging.

by

Christopher Michael Bernt

The cleavage of chemical bonds has a number of applications including the refinement of natural feedstocks and the controlled delivery of specific chemicals. This work describes two such examples, unified in that the cleavage is facilitated by inorganic, heterogenous catalysts. The first study describes the efforts to understand the reactivity of copper doped porous metal oxides (CuPMO), a promising lignocellulose disassembly catalyst, which cleanly converts lignin as well as lignocellulose composites, such as sawdust, to organic liquids with little or no formation of tars or chars. The second part examines the photo-oxidation of dithioxalates to produce carbon disulfide, a potentially therapeutic small molecule, in a controlled manner.

In both cases, product analysis was a key component of the study and underscored the potential in each system.

Despite its ability to cleanly disassemble lignocellulose in supercritical methanol, CuPMO also catalyzes less desirable aromatic ring hydrogenations and various methylations that dramatically increase the complexity of the product stream. In order to determine the reaction rates relevant to the reductive disassembly of lignin by this catalyst system, a quantitative experimental evaluation of model reactions was performed. These helped to quantitatively assess the rates of desirable and less desirable chemical steps that define the overall product selectivities. Global fitting analysis methods were used to map the temporal evolution of key intermediates and products and to elucidate networks that provide guidelines regarding the eventual fates of reactive intermediates in this catalysis system.

Phenolic compounds were shown to display multiple reaction pathways, but substrates such as benzene, toluene, and alkyl- and alkoxy-substituted aromatics were considerably more stable under these conditions. These results indicate that modifying this catalytic system in a way that controls and channels the reactivity of phenolic intermediates should improve selectivity toward producing valuable aromatic chemicals from biomass-derived lignin. To this end we demonstrated that the O-methylating agent dimethyl carbonate can intercept the phenol intermediate formed from hydrogenolysis of the model compound benzyl phenyl ether. Trapping the phenol as anisole thus gave much higher selectivity towards aromatic products.

Following up on the reactivity study was an investigation into the dependencies of the temporal product evolution for model compounds over copper doped porous metal oxides in supercritical-methanol. These investigated 1-phenylethanol (PPE), benzyl phenyl ether (BPE), dihydrobenzofuran (DHBF), and phenol for operating temperature ranges from 280 –

330 °C. The first three model compounds represent the β-O-4 and α-O-4 linkages in lignin as well as the furan group commonly found in the β-5 linkage. Phenol was investigated due to its key role in product proliferation. In general, the apparent activation energies (E_a's) for ether hydrogenolysis proved to be much smaller than that for the hydrogenation of phenol, a major side reaction leading product proliferation. Thus, temperature tuning may be a useful strategy to preserve product aromaticity as demonstrated by the more selective conversion of BPE and PPE at the lower temperatures. Rates of methanol reforming over this catalyst system were also studied over the temperature range 280 – 320 °C, since MeOH reforming to produce reducing equivalents is an integral component of this catalytic system. In the absence of substrate, the gaseous products H_2, CO, and CO_2 were formed in ratios stoichiometrically consistent with catalyzed methanol reformation and water gas shift reactions. The latter studies suggest that the H_2 production ceases to be rate limiting early in batch reactor experiments, but also suggest that overproduction may also lead to product proliferation.

The second part of this work describes the successful attempt to photochemically release carbon disulfide motivated by the potentiality of its therapeutic effects. In this study carbon disulfide is generated via oxidative cleavage of 1,1dithiooxalate (DTO) photosensitized by CdSe quantum dots (QDs). Irradiation of DTO−QD conjugates leads to λ_{irr} independent photooxidation with a quantum yield of ∼4% in aerated pH 9 buffer solution that drops sharply in deaerated solution. Excess DTO is similarly decomposed, indicating labile exchange at the QD surfaces and a photocatalytic cycle. Analogous photoreaction occurs with the O-tert-butyl ester tBuDTO in nonaqueous media. It is proposed that oxidation is initiated by hole transfer from photoexcited QD to surface DTO and that these substrates are a promising class of photocleavable ligands for modifying QD surface coordination.

TABLE OF CONTENTS

Appendix A. Supplemental Information for Chapter II

Appendix B. Supplemental Information for Chapter III

Appendix C. Supplemental Information for Chapter IV

Appendix D. Supplemental Information for Chapter V

Chapter I: Introduction to Lignocellulose Disassembly Over Copper Doped Porous Metal Oxides*

1.1 Sustainability and Lignin

Lignocellulose, the principal component of woody biomass, is a non-edible and sustainable feedstock that has the potential to be a renewable resource for producing commodity chemicals and fuels.[1-7] However, practical applications require an integrated approach to maximize atom and electron economy in extracting the energy and material contained therein. With this in mind, it is notable that a major constituent, lignin, (15-40% of lignocellulose depending on the plant type and origin)[1,3] remains underutilized.[8]. Biorefineries for "2nd generation" ethanol fuel production typically focus on the carbohydrates, and the lignin fraction, owing to its chemical recalcitrance and heterogeneity, is mostly burned to produce low-grade heat.[1] This is also the case with the production of paper goods from lignocellulose. Thus, designing selective pathways to convert lignin to chemicals and/or liquid fuels should add considerable value to biomass conversion schemes. Lignin has high potential as a carbon-neutral source of aromatic chemicals and successful commodification of lignin would add value to intentionally planted lignocellulosic crops and to agriculture and forest wastes.[1] It is estimated[1,9] that 62 Mt residual lignin will be generated annually by 2022 from US-mandated ethanol production alone. This is on the same scale as BTX (benzene, toluene and xylenes) production from fossilized carbon.[10] While BTX could be a drop-in target for

* Major Components of this chapter are reproduced from the following reference with permission from the Royal Society of Chemistry: C. M. Bernt, G. Bottari, J. A. Barrett, S. L. Scott, K. Barta, P. C. Ford, "Mapping reactivities of aromatic models with a lignin disassembly catalyst. Steps toward controlling product selectivity" *Catal. Sci. Tech.* **2016**, *6*, 2984-2994

biomass conversion, lignin disassembly will also lead to functionalized aromatics that have the potential to serve as the building blocks for new materials.[11,12] Effective utilization of lignin remains a major intellectual challenge[1-3] that is drawing increasing interest from the chemical community.[13-20]

1.2 Properties and Structure of Lignin

Lignocellulose is about 70-80% carbohydrates, with the balance largely being lignin. Notably, lignin has the highest proportional carbon content of the major lignocellulose components and is unique among biomass in general in its frequency of aromatic units and relatively high energy density.

Lignin is a complex, heterogeneous polymer (see figure 1.1) formed biologically by free radical initiated polymerization of aromatic monolignols (principally p-coumaryl, coniferyl and sinapyl alcohols) in ratios that depend upon the source.[21] The principal linkages are aryl-ether bonds, although the monolignols are occasionally crosslinked by C-C bonds. The types of bonds are systematically identified by the linkages based on the structure of the constituent monolignols (see figure 1.2) and very widely in their frequency depending on the type of bond on lignin source. Of these linkages, by far the most common is the β-O-4 linkages, representing up to 50% of the bonds in lignin. The next most abundant are biphenyl (3-20%), β-5 (4-10%), and α-O-4 (3-5%) linkages.[7,21-23] Developing selective methodologies to cleave such linkages while preserving the aromatic functionality during lignin disassembly has been a major goal of the Ford Group and other laboratories.[3,5,12,14-20,24-29]

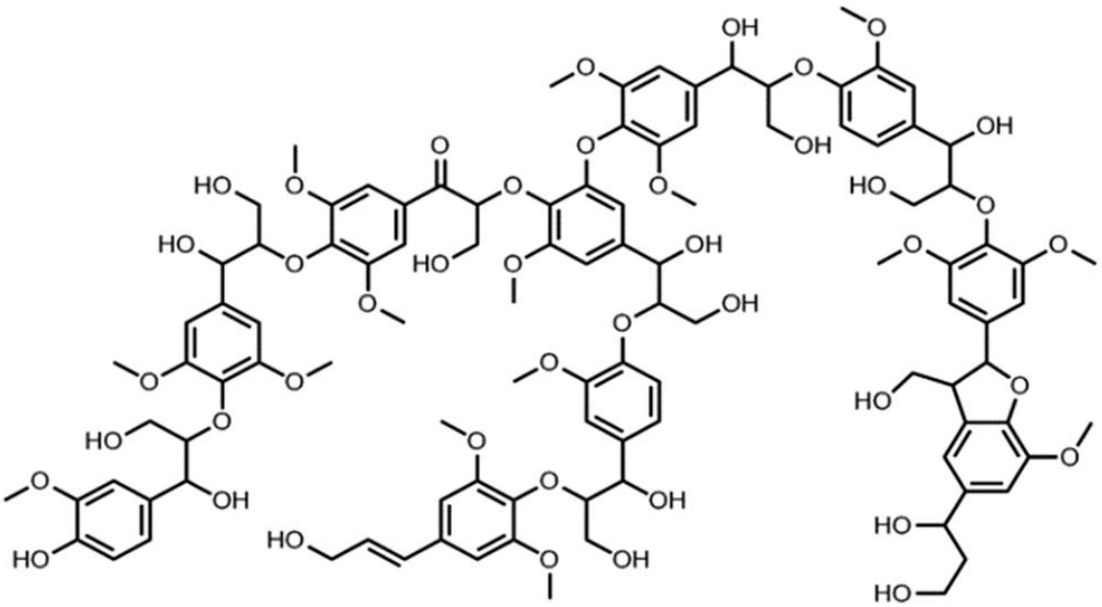

Figure 1.1: *A representative structure for a lignin fragment based on structural data by Sannigrahi et al.[7] and Stewart et al.[22]*

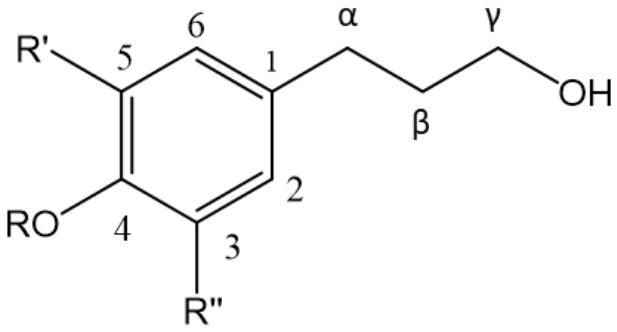

Figure 1.2: *Numbering system for naming linkages in lignin. For example, the β-O-4 linkage would be the ether formed between the second carbon on the propyl chain of one monolignol to the oxygen para to the propyl chain on a second monolignol.*

1.3 Porous Metal Oxides as Sustainable Lignin Disassembly Catalysts

The Ford group previously demonstrated the clean reductive disassembly of organosolv lignin to organic liquids without formation of intractable chars or tars.[30] This process is heterogeneously catalyzed by a copper-doped porous metal oxide (Cu20PMO) that is prepared by calcining a 3:1 Mg^{2+}:Al^{3+} hydrotalcite in which 20% of the Mg^{2+} had been replaced by Cu^{2+}. The reaction is carried out in a batch reactor in super-critical methanol (sc-MeOH). The same catalytic system also liquefies cellulose and, remarkably, disassembles lignocellulosic materials such as sawdust or wood chips to organic liquids with little or no char formation.[26,31] A relatively complex mixture of aliphatic alcohols and ethers is obtained from the carbohydrate fraction, while a similarly complex mixture of propylcyclohexanol derivatives is generated from the lignin.[30,31] The latter products are attributed to the hydrogenolysis of various phenyl ethers, with competing and subsequent hydrodeoxygenation (HDO) and hydrogenation of alkenes and aromatic rings. The methanol medium provides the reducing equivalents[26,30-32] via alcohol reforming[33] and the water-gas shift reaction,[34] both catalyzed by the CuPMO to generate a gas phase consisting of H_2 and CO plus some CO_2 and small amounts of methane. Less desirable side-reactions in this medium are ring methylations. These processes and the composition of the gas phase products have been previously described in greater detail.[26,30-32]

The importance of the copper in these catalysts was demonstrated in earlier studies with pine sawdust.[31] While this substrate was readily converted to organic liquids by the Cu20PMO in sc-MeOH, the products are largely char and unreactive biomass under similar conditions with a Mg/Al hydrotalcite-derived PMO catalyst not containing copper. Analogous results were found when no catalyst was added.

Cu20PMO has been shown to be effective in the H_2 hydrogenation of candlenut lignin to aromatic products[24] and for the reduction of 5-hydroxymethylfurfural to tetrahydrofuran derivatives.[35,36] A related study demonstrated disassembly of organosolv lignin using a copper-doped magnesium-aluminum mixed metal oxide catalyst in supercritical ethanol.[37] However, it is clear that improved selectivity to generate product streams composed of a limited number of aromatic chemicals would significantly enhance the value of lignin as a renewable feedstock.

The efficacy of the CuPMO catalyzed lignin disassembly in scMeOH inspired the probe into the hydrogenolysis of various aryl ether models with the goals of elucidating both the relative rates for reactions of characteristic lignin linkages and of identifying the intermediate species responsible for product proliferation. Such information will provide guidelines for defining reaction conditions that improve the selectivity and valorization of the product stream from lignin and other renewable biomass substrates.

1.4 References for Introduction to Lignocellulose Disassembly

1. J. Ragauskas, G. T. Beckham, M. J. Biddy, R. Chandra, F. Chen, M. F. Davis, B. H. Davison, R. A. Dixon, P. Gilna, M. Kel-ler, P. Langan, A. K. Naskar, J. N. Saddler, T. J. Tschaplinski, G. A. Tuskan and C. E. Wyman, "Lignin Valorization: Improving Lignin Processing in the Biorefinery" *Science*, **2014**, *344*, 709.

2. C. O. Tuck, E. Perez, I. T. Horvath, R. A. Sheldon and M. Poliakoff, "Valorization of Biomass: Deriving More Value from Waste" *Science*, **2012**, *337*, 695–699.

3. J. Zakzeski, P. C. A. Bruijnincx, A. L. Jongerius and B. M. Weck-huysen, "The Catalytic Valorization of Lignin for the Production of Renewable Chemicals" *Chem. Rev.*, **2010**, *110*, 3552–3599.

4. P. Azadi, O. R. Inderwildi, R. Farnood and D. A. King, "Liquid fuels, hydrogen and chemicals from lignin: A critical review" *Renewable Sustainable Energy Rev.*, **2013**, *21*, 506–523.

5. Y.-C. Lin and G. W. Huber, "The critical role of heterogeneous catalysis in lignocellulosic biomass conversion" *Energy Environ. Sci.*, **2009**, *2*, 68 –80.

6. T. Werpy and G. Petersen, *Top Value Added Chemicals from Biomass Volume II – Results of Screening for Potential Candidates from Biorefinery Lignin*, Pacific Northwest National Laboratory and the National Renewable Energy Laboratory, **2007**.

7. P. Sannigrahi, A. J. Ragauskas and G. A. Tuskan, "Poplar as a feedstock for biofuels: a review of compositional characteristics" *Biofuels, Bioprod. Biorefin.*, **2010**, *4*, 209–226.

8. A. J. Ragauskas, C. K. Williams, B. H. Davison, G. Britovsek, J. Cairney, C. A. Eckert, W. J. Frederick Jr., J. P. Hallett, D. J. Leak, C. L. Liotta, J. R. Mielenz, R. Murphy, R. Templer, T. Tschaplinski, "The path forward for biofuels and biomaterials" *Science* **2006**, *311*, 484−489.

9. R. Lal, "Soils and sustainable agriculture: a review" *Agron. Sustainable Dev.*, **2008**, *28*, 15-22.

10. Global Aromatic Chemicals (Benzene, Toluene & Xylene) Market 2014. http://www.researchandmarkets.com/research/ 6xr4ck/global_aromatic, (accessed Jan 29, **2015**).

11. A. G. Pemba, M. Rostagno, A. L. Tanner and S. A. Miller, "Cyclic and spirocyclic polyacetal ethers from lignin-based aromatics" *Polym. Chem.*, **2014**, *5*, 3124–3221.

12. H. Luo, I. M. Klein, Y. Jiang, H. Zhu, B. Liu, H. L. Kenttamaa, M. M. Abu-Omar, "Total utilization of miscanthus biomass, lignin and carbohydrates, using earth abundant nickel catalyst" *ACS Susatinable Chem. Eng.* **2016**, *4*, 2316-2322.

13. B. Sedai, C. Díaz-Urrutia, R. T. Baker, R. Wu, L. A. Silks and S. K. Hanson, "Aerobic oxidation of β-1 lignin model compounds with copper and oxovanadium catalysts" *ACS Catal.*, **2013**, *B*, 3111–3122.

14. S. Van den Bosch, W. Schutyser, R. Vanholme, T. Driessen, S.-F. Koelewijn, T. Renders, B. De Meester, W. J. J. Huijgen, W. Dehaen, C. M. Courtin, B. Lagrain, W. Boerjan and B. F. Sels, "Reductive lignocellulose fractionation into soluble lignin derived phenolic monomers and dimers and processable carbohydrate pulps" *Energy Environ. Sci.*, **2015**, *8*, 1748–1763.

15. R. Ma, W. Hao, X. Ma, Y. Tian and Y. D. Li, "Catalytic Ethanolysis of Kraft Lignin into High-Value Small-Molecular Chemicals over a Nanostructured alpha-Molybdenum Carbide Catalyst" *Angew. Chem., Int. Ed.*, **2014**, *53*, 7310–7315.

16. J. Zhang, Y. Chen and M. A. Brook, "Reductive Degradation of Lignin and Model Compounds by Hydrosilanes" *ACS Sustainable Chem. Eng.*, **2014**, *2*, 1983–1991.

17. A. K. Deepa and P. L. Dhepe, "Lignin Depolymerization into Aromatic Monomers over Solid Acid Catalysts" *ACS Catal.*, **2015**, 5, 365–379.

18. A. Rahimi, A. Ulbrich, J. J. Coon and S. S. Stahl, "Formic-acid induced depolymerization of oxidized lignin to aromatics" *Nature*, **2014**, *515*, 249–252.

19. Y. Jiang, Z. Li, X. Tang, Y. Sun, X. Zeng, S. Liu and L. Lin, "Depolymerization of cellulolytic enzyme lignin for the production of monomeric phenols over raney Ni and acidic zeolite catalysts" Energy Fuels, **2015**, *29*, 1662–1668.

20. M. R. Sturgeon, M. H. O'Brien, P. N. Ciesielski, R. Katahira, J. S. Kruger, S. C. Chmely, J. Hamlin, K. Lawrence, G. B. Hunsinger, T. D. Foust, R. M. Baldwin, M. J. Biddy and G. T. Beckham, "Lignin depolymerisation by nickel supported layered-double hydroxide catalysts" *Green Chem.*, **2014**, *16*, 824 –835.

21. W. Boerjan, J. Ralph and M. Baucher, "Lignin Biosynthesis" *Annu. Rev. Plant Biol.*, **2003**, *54*, 519–546.

22. J. J. Stewart, T. Akiyama, C. Chapple, J. Ralph and S. D. Mansfield, "The effects on lignin structure of overexpression of ferulate 5-hydroxylase in hybrid poplar" *Plant Physiol.*, **2009**, *150*, 622–635.

23. P. M. Froass, A. J. Ragauskas, J. Jiang, "Chemical Structure of Residual Lignin from Kraft Pulp" *J. Wood Chem. Technol.* **1996**, *16*, 347−365.
24. K. Barta, G. R. Warner, E. S. Beach, P. Anastas, P. "Depolymerization of organosolv lignin to aromatic compounds over Cu-doped porous metal oxides" *Green Chem.* **2014**, *16*, 191-196.

25. J. A. Barrett, Y. Gao, C. M. Bernt, M. Chui, A. T. Tran, M. B. Foston, P. C. Ford, "Enhancing aromatic production from reductive lignin disassembly: in situ O-methylation of phenolic intermediates" *ACS Sustainable Chem. Eng.* **2016**, *4*, 6877-6886.

26. K. Barta, P. C. Ford, "Catalytic conversion of nonfood woody biomass solids to organic liquids" *Acc. Chem. Res.* **2014**, *47*, 1503-1512.

27. M. Chui, G. Metzker, C. M. Bernt, A. T. Tran, A. C. Burtoloso, P. C. Ford, "Probing the lignin disassembly pathways with modified catalysts based on Cu-doped porous metal oxides" *ACS Sustainable Chem. Eng.* **2017**, *5*, 3158-3169.

28. Y.-B. Huang, L. Yan, M.-Y. Chen, Q.-X. Guo, Y. Fu, "Selective hydrogenolysis of phenols and phenyl ethers to arenes through direct C-O cleavage over ruthenium-tungsten bifunctional catalysts" *Green Chem.* **2015**, *17*, 3010-3017.

29. V. Molinari, C. Giordano, M. Antonietti, D. Esposito, "Titanium nitride-nickel nanocomposite as heterogenous catalyst for the hydrogenolysis of aryl ethers" *J. Am. Chem. Soc.* **2014,** *136*, 1758-1761.

30. K. Barta, T. D. Matson, M. L. Fett'ig, S. L. Scott, A. V. Iretskii, P. C. Ford, "Catalytic Disassembly of an Organosolv Lignin via Hydrogen Transfer from Supercritical Methanol" *Green Chem.*, **2010**, *12*, 1640.

31. T. D. Matson, K. Barta, A. V. Iretskii, P. C. Ford, "One-Pot Catalytic Conversion of Cellulose and of Woody Biomass Solids to Liquid Fuels" *J. Am. Chem. Soc.*, **2011**, *133*, 14090–14097.

32. G. S. Macala, T. D. Matson, C. L. Johnson, R. S. Lewis, A. V. Iretskii, P. C. Ford "Hydrogen Transfer from Supercritical Methanol Over a Solid Base Catalyst: a Model for Lignin Depolymerization" *ChemSusChem.*, **2009**, *2*, 215–217.

33. S. Lee, *Methanol Synthesis Technology*, CRC Press, Boca Raton, Florida, **1990**.

34. A. A. Gokhale, J. A. Dumesic, M. Mavrikakis, "On the Mechanism of Low-Temperature Water Gas Shift Reaction on Copper" *J. Am. Chem. Soc.*, **2008**, *130*, 1402–1414.

35. T. S. Hansen, K. Barta, P. T. Anastas, P. C. Ford, A. Riisager "One-pot reduction of 5-hydroxymethylfurfural via hydrogen transfer from supercritical methanol" *Green Chem.*, **2012**, *14*, 2457–2461.

36. A. J. Kumalaputri, G. Bottari, P. M. Erne, H. J. Heeres, K. Barta “Tunable and Selective Conversion of 5-HMF to 2, 5-Furandimethanol and 2, 5-Dimethylfuran over Copper-Doped Porous Metal Oxides” *ChemSusChem*, **2014**, *7*, 2266 –2275.

37. X. Huang, T. I. Koranyi, M. D. Boot, E. J. M. Hensen “Catalytic Depolymerization of Lignin in Supercritical Ethanol” *ChemSusChem*, **2014**, *7*, 2276–2288.

Chapter II: Methods for Biomass Conversion Research

2.1 Materials

The majority of chemicals used for these studies were purchased from Sigma-Aldrich, Acros, or TCI and used as supplied (see appendix A1 for list of chemicals). Typically, the methanol used for disassembly reactions was dried over molecular sieves prior to use. Several bottles of benzyl phenyl ether (BPE) were supplied discolored, presumably by the halogenated byproducts of its synthesis.[1] In these cases, the BPE was dissolved in a dilute solution of sodium hydroxide then precipitated from this solution by the dropwise addition of water. The precipitate was filtered to afford a white powder indicative of a cleaner BPE stock. 2-phenoxy-1-phenylethanone, 2-phenoxy-1-phenylethan-1-ol and organosolv lignin were prepared from procedures adapted from published protocols as described in the following sections.

***2.1.1 synthesis of 2-phenoxy-1-phenylethanone*:** The syntheses of 2-phenoxy-1-phenylethanone (equation 2.1) and 2-phenoxy-1-phenylethanol were adapted from the protocol described by J. M. Nichols et. Al.[2] A worksheet summarizing this adaptation can be found in appendix A2.

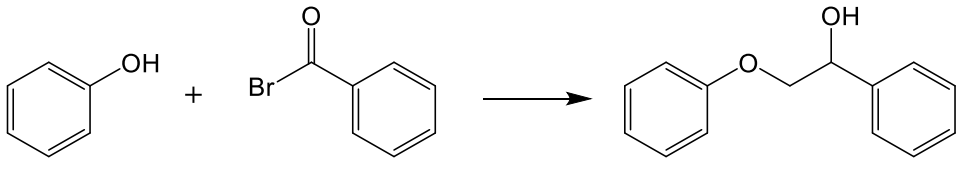

(2.1)

In a typical preparation 17.5 g (ca. 127 mmol) of potassium carbonate was mixed into 200 mL of acetone in a 1000 mL round-bottom flask equipped with a magnetic stir bar. A 19.5 g (ca.

98 mmol) portion of 2-bromoacetophenone was added to the flask and stirred until dissolved and then 10 g (ca. 106 mmol, or 9.4 mL of liquid) of phenol was then added. A reflux condenser was attached and the solution was heated to a gentle reflux (B.P. ~ 56 °C) then refluxed overnight. The following day the solution was allowed to cool and then filtered. The solid was discarded and the yellow filtrate was transferred to a separate vessel and dried under vacuum to collect a yellow solid. This solid was then recrystallized to improve purity by dissolving in a minimal amount of warm ethanol and subsequently cooling in an ice bath. The resultant pale-yellow crystals are collected and washed with ice cold ethanol. The resultant product was 2-phenoxy-1-phenylethan-1-one.

2.1.2 syntheses of 2-phenoxy-1-phenylethan-1-ol: In a typical preparation, a 6.37g (30 mmol) sample of 2-phenoxy-1-phenylethan-1-one was dissolved in 136 mL of tetrahydrofuran (THF) and 34 mL of water was added for a final solution v:v ratio of 4:1 THF:H_2O. After this step, 2.3 g of the reducing agent, sodium borohydride, was weighed out and added to this mixture portion wise. During this addition, gentle bubbling was observed which is a positive indication of the production of hydrogen and freshness of the reducing agent. After all of the sodium borohydride was added, the solution was stirred at room temperature for three hours. After 3 h, the remaining sodium borohydride was quenched with 200 mL of a saturated (mg/ml) ammonium chloride solution. This solution was further diluted with 200 mL of water and the total mixture was extracted 3x200 ml with diethyl ether. (Note, the ether layer is on top so you'll need to save the aqueous layer in a beaker, collect the ether layer in a separate beaker, and pour the aqueous layer back into the separatory funnel for each extraction.) The combined ether fractions were then washed twice with 100 mL of brine and

then dried over magnesium sulfate. This solution was filtered to remove the drying agent, and the solvent was removed under vacuum to afford colorless crystals.

2.1.3 Preparation of Methanosolv Lignin: The organic extraction of lignin was based on the methods by described Barta et al. referencing those originally developed by Harris et al.[4,5] In a typical largescale preparation, approximately one kilogram of poplar wood chips was placed in a 19 L bucket and pretreated to remove extractives (e.g. terpenes). The pretreatment was performed by adding 16 L of a 1:1 toluene: ethanol solution to the wood chips and allowing to soak for 24 hours at room temperature. The pretreated woodchips were separated by filtration and dried in air for four days. After drying, 4.5 L of methanol and 12 mL of concentrated hydrochloric acid were added to a 12 L round-bottom flask equipped with a reflux condenser and overhead stirrer, set to 200 rpm. While stirring, 600 g of the dried, pretreated woodchips were added over the course of 3 hours and then the mixture was heated to gentle reflux. After one day, the stirring speed was reduced to 150 rpm and the reaction was allowed to proceed for an additional 7 days. Upon completion, the resultant brown solution was filtered to remove the spent woodchips, and washed with 2.5 L of methanol. This solution was reduced to 1.5 L under vacuum and subsequently cooled in ice to form a brown precipitate. This precipitate was filtered, washed with cold water, and dried in a vacuum chamber with phosphorous pentoxide to yield the final methanosolv lignin.

2.2 Synthesis of Copper Doped Porous Metal Oxide Catalyst (Cu20PMO)

The general procedure to produce the copper doped porous metal oxide catalyst started (Cu20PMO) with the synthesis of the hydrotalcite (HTC) precursor via a co-precipitation method followed by drying and calcining to obtain the final catalyst used in these studies. These techniques were adapted from those described by Cosimo et al. and subsequently modified by Macala et al.[6,7] For ease of reproduction, a worksheet summarizing the preparation of CuPMO can be found in appendix A3.

The CuPMO precursor was a 3:1, Mg^{2+}: Al^{3+} hydrotalcite where 20% of the magnesium has been replaced by copper (CuHTC). In a typical synthesis of the CuHTC, a solution of sodium carbonate was prepared by dissolving 6.62 g in 300 mL of water in a 1000 mL flask. A stir bar was added to this flask and it was heated to 60 °C. While heating, a solution of the metal nitrates was prepared by dissolving 37.5 mmol of copper(II) nitrate monohydrate, 62.5 mmol of aluminum nitrate nonahydrate and 150 mmol of magnesium nitrate hexahydrate in approximately 150 mL of water. Finally, a solution of 200 mmol of sodium hydroxide in 200 mL of water was prepared.

The solution of nitrates was added dropwise to the sodium carbonate solution while stirring continuously. As the nitrates were added a blue flocculate began to form and the pH of the solution decreased. During the addition of the nitrate salts, the pH was kept between 9 and 10 by addition of the sodium hydroxide solution as needed. After all the nitrate solution was added, which took approximately 90 minutes, the mixture was loosely covered with

plastic paraffin film (Parafilm) and left at 60 °C overnight. Note, that while a typical preparation was aged overnight, this step ranged from 4 hours to several days with no noticeable variance in catalyst activity.

Following aging, the HTC was removed from heat and collected by filtration. The filtered HTC was re-suspended in a solution of sodium carbonate and allowed to wash for several hours help remove any residual nitrate. Following the sodium carbonate wash the catalyst was again filtered and subsequently washed with 3 x 300 mL of water. After this final wash, the catalyst was placed in a crucible and dried at 110 °C overnight. It should be noted that the catalyst should be dried for at least 4 hours and longer drying times seem to have no adverse effect other than making the dried HTC more difficult to grind into powder. The dried CuHTC was then ground using a mortar and pestle until it formed a fine, uniform, light blue powder. The CuPMO for each experiment was prepared by freshly calcining the CuHTC by heating at 460 °C overnight. Typically, the calcination process resulted in a roughly 40-60% decrease in mass from the parent CuHTC. Un-doped PMO catalysts used in control studies were prepared by calcination of 3:1 Mg^{2+}:Al^{3+} hydrotalcite purchased from Sigma.

2.3 Disassembly Reaction Procedure

2.3.1 Composition of Reaction Solutions: In order to minimize data variance due to measurement uncertainty, the disassembly reactions in these studies were carried out on aliquots taken from stock solutions. Stock solutions were prepared with a ratio of 1 mmol of model substrate or 1 g of methanosolv lignin and 20 μL (~103 μmol) of n-decane per 3 mL of methanol. The n-decane was included as an internal standard based on the assumption that it is unreactive with the catalyst system. A typical preparation would consist of 20 mL of stock solution to provide for six reaction solutions of 3 mL each plus a small amount extra to analyze directly to provide experimental starting concentrations.

2.3.2 Reactions in Mini-Autoclave Reactors: Catalytic disassembly of lignin model compounds was performed in high pressure mini-reactors following the general protocol described by previous members of the Ford Group.[5,7,8] The miniature autoclave reactors were composed of Swagelok components consisting of a ¾ inch, stainless steel union (part ID: SS-1210-6) capped by two ¾ inch, stainless steel plugs (part ID: SS-1210-P). One of the joints was welded shut to prevent accidental leakage when opening the reactors. In early studies samples of the catalyst (50 mg or 100 mg), the organic substrate (1 mmol) and the internal reference decane (20 μL) plus methanol (3 mL, dried over sieves) were measured directly into the reactors. The bulk of the experiments were done by measuring out the desired mass of catalyst into each reactor, and then adding 3 mL of the reaction stock solution. The filled reactors were then tightly sealed using either a toque wrench or two hand wrenches. For experiments that tracked the mass balance of the solvent, the complete vessels were weighed using an analytical balance before and after adding the reaction mixture. The reactors were

then placed into a pre-heated, custom fabricated, aluminum heating block which was either on a hot plate with a thermocouple or in a temperature controlled furnace. A standard reaction temperature was in the range of 280-330 °C. After the designated reaction time, ranging from 15 minutes to 18 hours, a specific reaction was quenched by rapidly cooling the mini-autoclave in a room temperature or ice-chilled water bath. For kinetics studies the reactors were cooled in a room temperature water bath or an ice bath. In studies which included solvent mass balance, the reactors were instead cooled with a high-speed fan to avoid erroneous addition of mass from the water bath. Reactors were weighed using an analytical balance after they had cooled to room temperature to ensure that there had been no change in the total mass.

2.3.3 Reactions in High Pressure Parr Reactors: Experiments carried out on a larger scale used stock solutions prepared with the same ratios as the smaller scale reactions and were carried out in either 25 mL or 100 mL Parr reactors. These reactions were operated at a similar time scale and temperature range as the mini-autoclave reactions. In order to insure a smooth transition to supercritical conditions, these reactions were charged with 5 atm of hydrogen prior to the experiment. It is also notable that a few of these reactions were run with Teflon O-rings, which is not advisable since the typical reaction temperature is near the maximum operating temperature of Teflon. At higher temperatures, graphite O-rings are preferred.

2.4 Gas Capture and Analysis

2.4.1 Mini-Autoclave Gas Capture Apparatus: For the analysis of gas in these studies samples were taken either from a sampling port in the par reactor or from a special apparatus for collection and volumetric measurement of gasses from the mini-autoclave reactors. This device consisted of an in-house fabricated, aluminum vessel chamber with a vent port, a connecting tube with a sampling port, and a simple water displacement apparatus (see figure 2.1). The aluminum vessel chamber was comprised of two halves: a bottom half designed to hold the reaction vessel in place with a rubber o-ring on the outside to prevent loss of gasses, and a top half which fit the top joint of the reactor which also had a hole to the vent port and a square protrusion on the outside so that the top portion could be turned with a wrench. The mini-autoclave reactors would be placed in this chamber and torque applied to the top half would unseal the vessel while directing the gas to the vent port for collection. This apparatus allowed for measurement of total volume of gas produced when allowed to come to atmospheric pressure, as well as sampling of the gas for analysis by GC/TCD. Since the sampling port was before the displacement setup, it was assumed that there was minimal water contamination and loss of dissolved gasses for the GC/TCG measurement. In the experiments with methanol only, the reactors were resealed and weighed on an analytical balance after venting the gas.

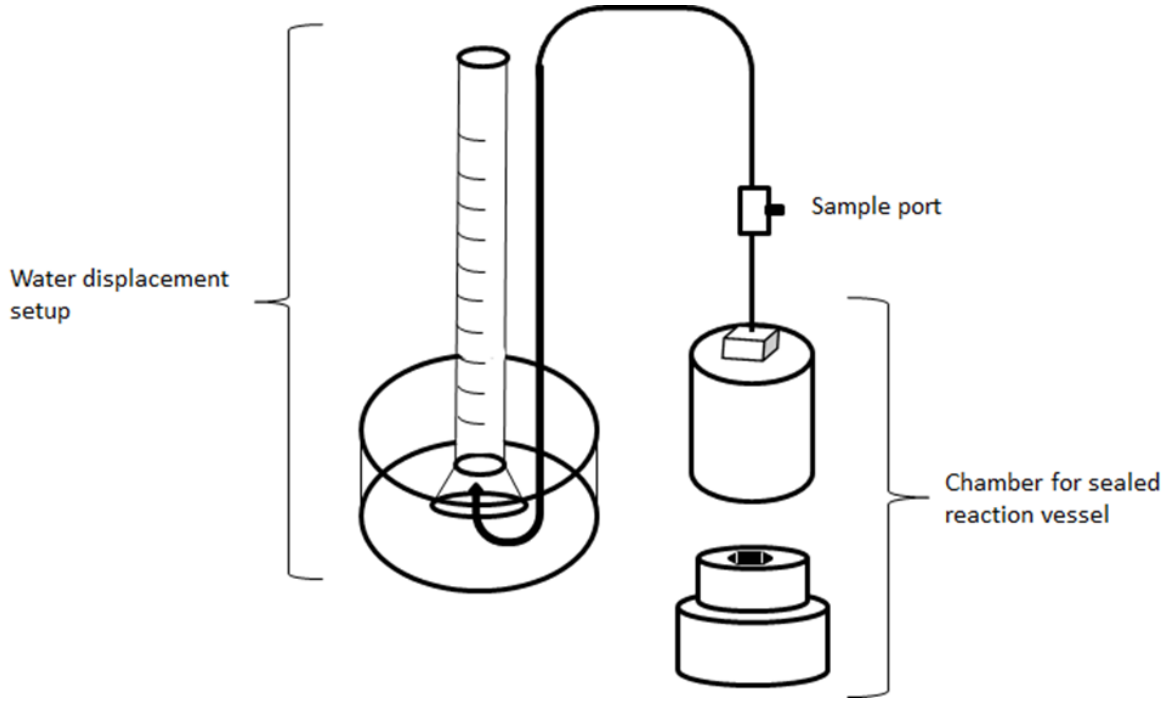

Figure 2.1: *Schematic of gas capture apparatus: Sealed autoclave reactors were placed in vessel chamber. The sealed chamber was then used to open the inner vessel, releasing gas into the connected water displacement apparatus.*

2.4.2 Gas Chromatography with Thermal Conductivity Detector for Gas Analysis:

Gas composition analysis was performed on an Agilent/HP 6890N (G1530N) gas chromatograph equipped with a thermal conductivity detector (TCD). This GC/TCD instrument was equipped with Supelco Carboxen 1010 PLOT column. This was a 30 m x 0.53 mm fused silica capillary column designed for the separation of permanent gasses and light hydrocarbons. For the GC method 100-500 µL samples were injected at a temperature of 225 °C in split mode with a 200:1 ratio and pressure flow control mode at 104.8 kPa, 276 mL/min total flow, 1.4 mL/min column flow, a linear velocity of 32 cm/sec and a purge flow of 3.0 mL/min. The temperature program started with a hold at 50 °C for 2 min. followed by a 25 °C/min ramp up to 300 °C where the temperature was held for 2 minutes. <quantification>

2.5 Solution Workup and Analysis

2.5.1 Separating Reaction Solution from Catalyst by Centrifugation: After cooling and any gas measurements, the liquid and solid contents of each individual reaction vessel were initially separated for liquid analysis in one of two ways. In initial experiments, the contents of a reaction vessel were transferred to a disposable 15 mL centrifuge tube and the reactor was washed out with MeOH (4 mL), which was combined with the original contents. The tube was centrifuged at a RCF of 6500 g for 15 minutes to separate the liquid and solid fractions. The liquid contents were collected from the tube and the remaining solid was resuspended in another 3 mL of methanol. This additional MeOH was intended as a wash to extract residually adsorbed substrate and soluble products (the earlier studies with organosolv lignin and lignocellulose composites as substrates[5,8] showed negligible or no gain in the mass of the recovered catalyst after such treatment indicating little organic residue, including chars, on the Cu20PMO).This suspension was centrifuged again at 6500 g for 15 minutes, and the second liquid fraction was combined with the first for product analysis. Samples for GC/FID analysis were taken directly from this combined solution, and further diluted by an approximate factor of 3 for GC/MS analysis. It should be noted that the pellet from this technique is loosely packed, and occasionally the final solutions would show some fine particulates on the bottom of the storage vial. While there is no evidence this residual effected the product analysis, such contaminants are best avoided to ensure the quality of GC based measurements.

2.5.2 Separating Reaction Solution from Catalyst via Syringe: The centrifuge method was switched in later experiments to increases processing speed and decrease the probability of small catalyst particulates being present in the analyte solution. For the alternate method, the contents of a reactor were poured into a disposable 10 mL luer lock syringe equipped with a 0.2-micron filter and a plug of glass wool. The remaining contents of the reactor vessel were washed out to give a total volume of 5-6 mL in the disposable syringe. The contents were filtered through the syringe. The liquid portion used directly for GC/FID analysis and was further diluted for GC/MS analysis. While this may have raised some concern about any products that may be loosely bound to the catalyst, there was no detectable difference in analytes between using the syringe filter method and the centrifuge method of reaction solution separation. For experiments that used GPC and/or NMR analysis the total solution was diluted further up to a volume of 10 mL. A 5 mL fraction of this dilution was removed and dried under vacuum to prepare for NMR analysis, 3 mL was used for GPC analysis and the remaining 2 mL for GC analysis. GPC samples were re-dissolved in THF and NMR samples were re-dissolved in $CDCl_3$.

2.5.3 Product Identification Using GC/MS: Compounds were identified using one of several different gas chromatographs equipped with a mass spectrometer (GC/MS). At UCSB two different instruments were used. The first of these was a Shimadzu GC-2010 equipped with a Shimadzu GCMS-QP2010 mass spectrometer. On this instrument 1μL samples were injected at a temperature of 225 °C in split mode with a 200:1 ratio. This GC-MS was equipped with an 30 m x 0.25 mm Agilent DB-1 column with a 0.25 μm lining. The GC program was run

in pressure flow control mode at 40 kPa, 162.3 mL/min total flow, 0.79 mL/min column flow, a linear velocity of 32.5 cm/sec and a purge flow of 3.0 mL/min. The temperature program started with a hold at 60 °C for 2 minutes followed by a 25°C/min ramp up to 200° - 300° C (depending on size and volatility of suspected analytes) where the temperature was held for 4 minutes. The corresponding MS program had an ion source temperature at 250 °C, interface temperature at 230 °C and recorded from 2.0 to 11.6 minutes during the GC program.

Also used was an HP 5970 GC/MS running in electrospray ionization (ESI) mode. The instrument was equipped with a J&W DB-5ms 30m GC column, with 0.25 mm ID and 0.25 µm film thickness. The GC program was run in pressure flow control mode at 40 kPa, 162.3 mL/min total flow, 0.79 mLmin column flow, a linear velocity of 32.5 cm/sec and a purge flow of 3.0 mL/min. The temperature program started with a hold at 60 °C for 2 minutes followed by a 25°C/min ramp up to 200°C where the temperature was held for 4 minutes. The corresponding MS program had an ion source temperature at 250°C, interface temperature at 230°C and recorded from 2.0 to 11.6 minutes during the GC program.

2.5.4 Quantitative Peak Determination Using GC/FID: The bulk of GC-FID measurements were conducted on an Agilent/HP 6890N (G1530N) gas chromatograph equipped with a flame ionization detector (FID). This GC/FID instrument was operated with two different columns. When used with a 30 m × 0.25 mm Agilent DB-1 + DG column, with a 0.25 µm dimethylpolysiloxane lining and a guard column, 0.5–2 µL samples were injected at a temperature of 225 °C in split mode with a 200 : 1 ratio. With this column, the GC program was run in pressure flow control mode at 104.8 kPa, 276 mL min^{-1} total flow, 1.4 mL min^{-1}

column flow, a linear velocity of 32 cm s^{-1} and a purge flow of 3.0 mL min^{-1}. The temperature program started with a hold at 50 °C for 2 min followed by a 25 °C min^{-1} ramp up to 200 °C where the temperature was held for 2 min. When used with a 30 m × 0.25 mm Agilent DB-5 column with a 0.25 μm (5%-phenyl)-methylpolysiloxane lining, 0.5–2 μL samples were injected at a temperature of 250 °C in split mode with a 20:1 ratio. With this column, the GC program was run in pressure flow control mode at 68.1 kPa, 27.6 mL min^{-1} total flow, and a 0.70 mL min^{-1} column flow. The FID detector was set at 250 °C with 30 mL min^{-1} H_2 and 350 mL min^{-1} air flow. The temperature program started with a hold at 45 °C for 6 min followed by a 4 °C min^{-1} ramp up to 175 °C where the temperature was held for 10 min.

Further quantitative measurements were performed on a Hewlett Packard 5890 GC with a customized split MS/FID. The GC was equipped with a 60 × 0.25 mm i.d. and 0.25 μm Restek RTX-1701 film capillary column and a 1:1 split ratio to the MS and flame ionization detectors. The temperature of the injector and FID detector were set at 250 °C and 285 °C, respectively. The GC oven temperature program started from 40 °C (10 min) and was then increased up to 250 °C with a heating rate of 10 °C min^{-1}.

2.5.5 Average Molecular Weight Determinations by Gel Permeation Chromatography: Gel permeation chromatography was used to look for the formation of aggregates in model study experiments and to monitor the disassembly of organosolv lignin. For analysis of model compound reaction mixtures, a Waters Alliance HPLC System was used. This was equipped with a 2690 Separation Module with Agilent PGEL (5 μm) and MIXED-D 300 mm × 7.5 mm columns, a Waters model 2410 differential refractometer and model 2998 photodiode array

detector. For the analysis of model compounds the HPLC was equipped with a Polymer Standards Service SDV column (5 μm). polymer size. This instrument was equipped with a Polymer Standards Service SECcurity RI detector and run with 1 mL/min flow. NMR

2.6 Treatment of Quantitative GC Data

Final concentrations of analytes in GC studies were derived using different approaches based on whether the data was collected via GC/MS or GC/FID. In both cases decane was used as a reference and an internal standard. Control experiments under standard reaction conditions indicated negligible change in decane for up to 24 hours. Standard curves for decane were created for each instrument used in this study. The total amount of each compound at the end of a reaction was calculated using equation 2.2 which accounts for changes in solvent volumes over the course of the experiment and GC preparation.

$$nmol_{analyte} = \left(\frac{\boldsymbol{A}_{analyte}}{\boldsymbol{rf}_{analyte}}\right)\left(\frac{Decane_{theoretical}}{Decane_{measured}}\right) \quad \textbf{(2.2)}$$

A is the integrated area of the peak associated with the given analyte, **rf** is the nanomolar response factor (nmol/μL) of the given analyte for the instrument and method used, and the theoretical decane is the amount added to each vessel prior to the reaction. When analysis was performed by GC/MS, standard curves were generated using the area of the GC/MS response for each target molecule. Unless specifically noted, these were the **rf** values used in equation 2.2.

For experiments using the GC/FID, the quantities of most products were calculated using the concept of effective carbon number (ECN). This is an approximation originally described by Sternberg et al.[9] This approximation is based on the mechanism of the FID response; the response is generally proportional to the carbon content of a given compound but can be modulated by bond structure and oxygen content.[9,10] The magnitude of the ECN is proportional to a given compound's response on the detector, and hence the ratio of ECN between two compounds is directly related to the ratio of the two compounds' molar response. Rearranging equations described by Scanlon et al.[10] and applying a basic definition of a molar response factor (equation 2.3) gives equation 2.4.

$$[Compound] = \left(\frac{\boldsymbol{A}_{compound}}{\boldsymbol{rf}_{compound}}\right) \quad \textbf{(2.3)}$$

$$\boldsymbol{rf}_{analyte} = (\boldsymbol{rf}_{decane})\left(\frac{\boldsymbol{ECN}_{analyte}}{\boldsymbol{ECN}_{decane}}\right) \quad \textbf{(2.4)}$$

The calculated effective carbon numbers and response factors relative to decane used for these studies are given in appendix A4 and based on theoretical ECN contributions provided by Sternberg and Scanlon.[9,10] This study used these values to calculate the analyte quantities for FID experiments when a specific standard curve for the given analyte was unavailable. The material balance was calculated from the moles of products determined for a given time point divided by the moles of substrate present at the start of the experiment (based on GC response).

2.7 Global Kinetics Analysis

2.7.1 Design of Reaction Networks: The initial design of reaction networks was based on the most parsimonious application of previously observed PMO catalyzed reactivities: hydrogenation, hydrodeoxygenation, C-O bond hydrogenolysis and methylation. Reactions were assumed to be first order with respect to the reactant at each step. Refinements to the model were based on the results of global fitting to the proposed models. For example, if a model returned a poor fit for one of the products of a reaction step the model was adjusted to examine other reasonable pathways.

2.7.2 Global Fitting Technique and Software: Global fitting was performed using DynaFit version 4 on a desktop computer.[11] Generally, global fitting uses a non-linear least squares approach. In the case of these studies DynaFit generates simultaneous progress curves for all species in the proposed network using an algorithm based on the system of differential equations provided by the network. The rate constants in the given reaction network were then optimized by the software such that the progress curves best matched the experimental data.

***2.7.3 Discussion on Descriptive Statistics for Global Fitting of Kinetics Data*:** Global kinetics fitting of non-linear data with several parameters makes formal statistical analysis a complex proposition. However, the goal was to utilize the simplest, chemically reasonable model and descriptive statistics to describe the observed product evolution and to show that the kinetics parameters obtained are self-consistent over the range of compounds studied.

The R^2 values (coefficient of determination) of the individual fits can provide insight into how much of the data is actually explained, and the lowest R^2 values for global fitting across these studies was greater than 0.85. This can be classically interpreted to mean that at least 85% of the variance in product distribution as a function of time is explained by the pseudo-first order fits. In the case of highly varied reactivities between species, this was sufficient to identify major trends in the data.

2.8 Methods References

1. H. Becker, W. Berger, G. Domschke, *Organicum. Practical Handbook of Organic Chemistry* Addison Wesley Pub. Co. **1973**, 208-210.

2. J. M. Nichols, L. M. Bishop, R. G. Bergman, J. A. Ellman, "Catalytic Bond Cleavage of 2-Aryloxy-1-arylethanols and Its Application to the Depolymerization of Lignin-Related Polymers" *J. Am. Chem. Soc.* **2010**, *132*, 12554-12555.

3. J. I. Cosimo, V. K. Diez, M. Xu, E. Iglesia, C. R. Apesteguia, "Structure and Surface and Catalytic Properties of Mg-Al Basic Oxides" *J. Catal.* **1998**, *178*, 499-510.

4. E. E. Harris, J. D'Ianni and H. Adkins, "Reaction of hardwood lignin with hydrogen" *J. Am. Chem. Soc.*, **1938**, *60*, 1467–1470.

5. K. Barta, T. D. Matson, M. L. Fettig, S. L. Scott, A. V. Iretskii, P. C. Ford, "Catalytic Disassembly of Organosolv Lignin via Hydrogen Transfer from Supercritical Methanol" *Green Chem.*, **2010**, *12*, 1640-1647.

6. J. I. Cosimo, V. K. Diez, M. Xu, E. Iglesia, C. R. Apesteguia, "Structure and Surface and Catalytic Properties of Mg-Al Basic Oxides" *J. Catal.* **1998**, *178*, 499-510.

7. G. S. Macala, T. D. Matson, C. L. Johnson, R. S. Lewis, A. V. Iretskii, P. C. Ford, "Hydrogen Transfer from Supercritical Methanol over a Solid Base Catalyst: A Model for Lignin Depolymerization" *Chem. Sus. Chem.*, **2009**, *2*, 215-217.

8. T. D. Matson, K. Barta, A. V. Iretskii and P. C. Ford, "One-Pot Catalytic Conversion of Cellulose and of Woody Biomass Solids to Liquid Fuels" *J. Am. Chem. Soc.*, **2011**, *133*, 14090–14097.

9. J.C. Sternberg, W.S. Gallaway, and D.T.L. Jones, "The mechanism of response of flame ionization detectors" *Gas Chromatography.* N. Brenner, J.E. Callen, and M.D. Weiss, eds. Academic Press, New York, **1962**, 231-67.

10. J. T. Scanlon, D. E. Willis, "Calculation of Flame Ionization Detector Relative Response Factors Using the Effective Carbon Number Concept." *J. Chromatogr. Sci.* **1985**, *23*, 333-340.

11. P. Kuzmic, "Program DYNAFIT for the Analysis of Enzyme Kinetic Data: Application to HIV Proteinase" *Anal. Biochem.*, **1996**, *237*, 260-273.

Chapter III: Mapping the Reactivity Network of CuPMOs with Lignin Model Compounds†

3.1 Introduction for Reactivity Studies

As discussed in chapter 1, copper doped porous metal oxides have a remarkable aptitude for the clean catalysis of lignin generation. However, improving selectivity to generate product streams composed of a limited number of aromatic chemicals would significantly enhance the value of lignin as a renewable feedstock. With this goal in mind, Chapter III is concerned with reactivity studies of various small molecules (Figure 3.1) that have structures and functional groups representative of the key reactive intermediates anticipated during lignin disassembly by Cu-PMO catalysts in sc-MeOH.[1] (Figure 3.2) Global kinetics analysis of the resulting reaction pathways allows mapping the reaction networks for the expected intermediates. Such networks can provide valuable insight into the underlying disassembly mechanisms and side-reactions that strongly influence the selectivity of this catalytic process as well as guidelines for intercepting the responsible intermediates, hence improving selectivity. Gates and coworkers[2,3] used a different numerical method to generate analogous reaction networks for the platinum catalyzed reactions of H_2 with vaporized models for pyrolysis-derived bio-oils.[4-7]

---

†This chapter is reproduced from the following reference with permission from the Royal Society of Chemistry: C. M. Bernt, G. Bottari, J. A. Barrett, S. L. Scott, K. Barta, P. C. Ford, "Mapping reactivities of aromatic models with a lignin disassembly catalyst. Steps toward controlling product selectivity" *Catal. Sci. Tech.* **2016**, *6*, 2984-2994

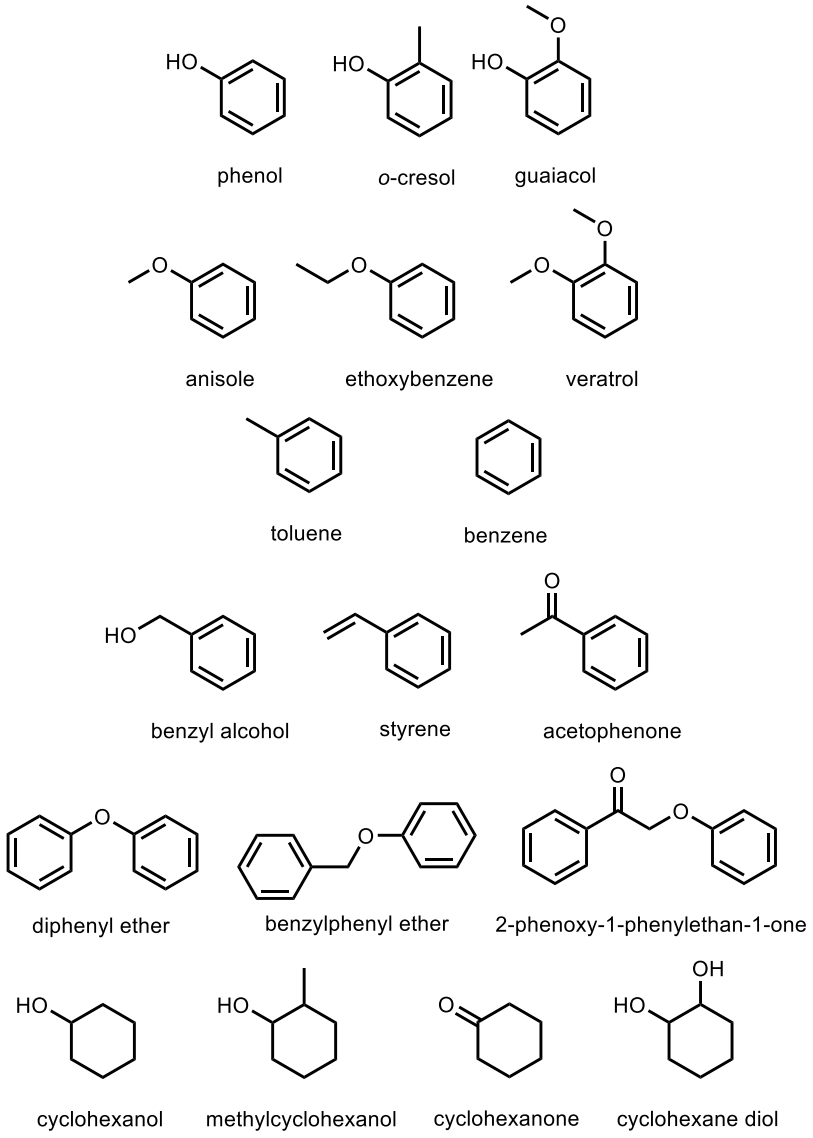

Figure 3.1: *Aromatic model compounds studied representing phenyl ether linkages and types of functional groups anticipated as intermediates in reductive lignin disassembly.*

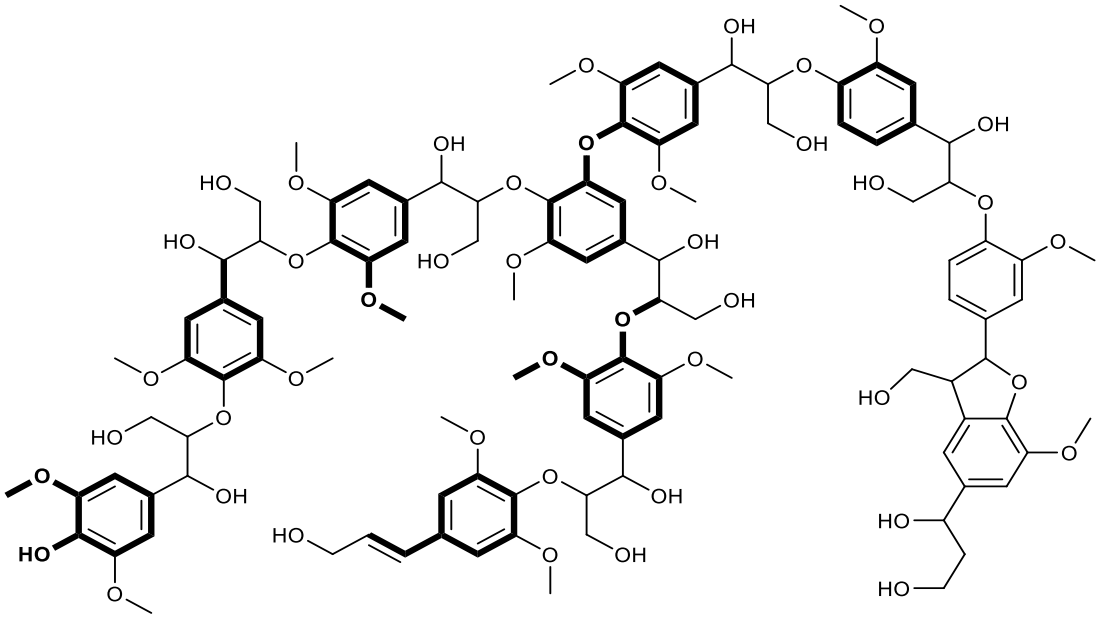

Figure 3.2: *A representative structure for a lignin fragment based on structural data by Sannigrahi et al.[8] and Stewart et al.[9] with some of the model compounds used in this study highlighted.*

Once the aryl-ether bonds in lignin are cleaved by hydrogenolysis or solvolysis during lignin disassembly over copper doped porous metal oxides (CuPMOs), a series of molecular intermediates are generated.[1,10] Expected cleavage products are phenolics with various substitution patterns on the aromatic ring including methoxy and oxidized aliphatic groups. In order to channel these intermediates into desirable and selective product streams, it is necessary to evaluate their reactivities under the conditions relevant to catalytic depolymerization. The simple models representative of those moieties (Figure 3.1) include mono-oxygenated (phenol and anisoles) and di-oxygenated (guaiacol and veratrol) aromatics that are common lignin motifs and disassembly intermediates, several other typical aromatic types (toluene, benzyl alcohol, styrene and acetophenone), as well as products of aromatic hydrogenation (cyclohexanol and cyclohexanone). Several di-aromatic model compounds

were also investigated in order to probe the rates of the sequential processes following aromatic ether hydrogenolysis. The results of these kinetics studies are used to develop quantitative reaction networks that show how product distributions are defined by the competing steps catalyzed under the conditions of lignin disassembly.

3.2 Methodological Considerations for Reactivity Studies

Reactions for these studies were carried out in methanol (3 mL), which becomes supercritical at reaction temperatures >240 °C in the 10 mL mini-reactors. In most cases, these batch reactors contained substrate (1.0 mmol), Cu20PMO catalyst (100 mg) and MeOH (3.0 mL). Decane (20 μL) was also added as an internal standard for quantification. A typical run involved 7-8 of these mini-reactors with identical quantities of catalyst, substrate and solvent that were heated together in an oven at the defined temperature (typically, 310 °C). At different time intervals, reactors quenched to room temperature in a water bath, and the products were analyzed using GC-MS fragmentation patterns for identification and GC-FID and GC-MS integrated areas for quantification as described in chapter II.

Under this catalytic system, the solvent contributes to the product mass by both methylation and hydrogenation, so it is more appropriate in this case to consider the molar material balance of substrate derived products. In this present study, the material balance over the course of catalysis was greater than 90% for most substrates, including the less reactive dimer diphenyl ether. The experiments with lower molar balance were those with phenolic substrates and those that lead to phenolics as major intermediates. In those cases, the product spread gave numerous small peaks that could be identified in most cases but were too small

to quantify reliably, so lower molar balances are largely attributed to product proliferation. Details for specific substrates are included in appendix B.

In the kinetics analysis, unaccounted products were treated as undefined product sinks. The temporal data thus obtained and summarized in appendix B were evaluated by global kinetics analysis using the DynaFit software[11] to give reactivity networks describing the interconnected catalytic pathways of different substrates and expected intermediates. The fits described in this study are sufficient to explain the defining trends in the observed data. In looking at consistency across studies, we can compare the rate constants and standard error (typically 20% or less) as determined by global fitting. In the case of reaction networks that share a reaction pathway (e.g. hydrogenation of phenol, starting with either phenol as a substrate or as a product of the guaiacol pathway) the values were indistinguishable within the experimental uncertainties. The parallel observation also held: pathways identified in as being significantly different in this study varied from each other in a magnitude greater than the individual errors. These results argue against major interferences of the catalytic rates of, or products from, specific substrates from the presence of other characteristic substrates among the systems studied.

3.3 Reactions of Aromatic Alcohols: Phenol, Cresol, and Guaiacol

The time course of major products from phenol over an 18 h period is shown in Figure 3.3 and summarized in appendix B1. After just 1 h at 310 °C, roughly half the phenol was consumed. After 3 h, this increased to 92%. The major products at this time point were methylcyclohexanol (25%), cyclohexanol (28%), anisole (9%) and 2-methylphenol (7%). Lesser products included dimethylphenols (3%), dimethylcyclohexanols (3%), 2-

methylanisole (2%), 2-methylcyclohexanone (1%), cyclohexanone (1%), methoxy-cyclohexane, methylcyclohexane, cyclohexane and others. For reaction times ≥ 9 h, the major product(s) were methylated cyclohexanols (MCHs), while anisole was the most abundant aromatic product.

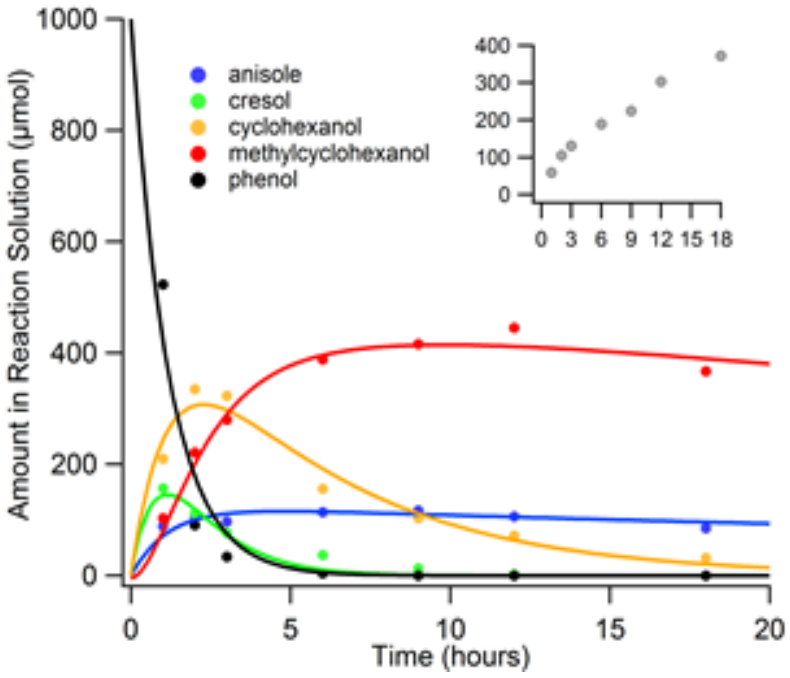

Figure 3.3: *Temporal evolution of products formed from phenol (1 mmol) in a batch reactor containing Cu20PMO in sc-MeOH (T = 310 °C). Inset: Sum of the other products not shown in parent graph (see appendix B). Material balance 78% after 6 h and 75% after 18 h.*

These products suggest that phenol is depleted via three primary reaction channels: (i) hydrogenation to cyclohexanol, (ii) methylation of the aromatic ring to give cresols (methylphenols) and (iii) methylation at oxygen to form anisole. Subsequent reactions convert the primary product cyclohexanol to MCHs (Scheme 3.1). Ring methylation is a common reaction for phenols,[12] and was shown to be a major pathway in earlier studies with the model compound dihydrobenzofuran (DHBF) under comparable conditions.[13]

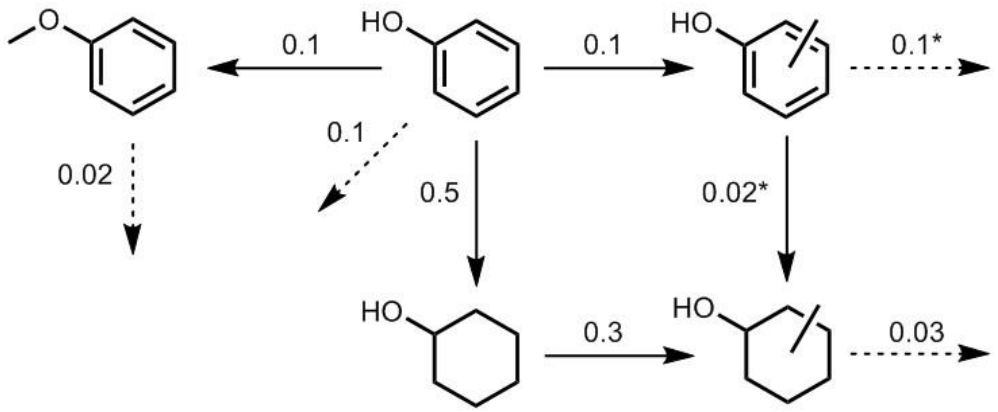

Scheme 3.1: *Reaction network for phenol: (1 mmol substrate, 100 mg Cu20PMO, 3 mL MeOH, 310 °C). Observed rate constants are shown for each step, in units of h^{-1}. Dashed lines indicate conversion to unidentified compounds. Asterisks indicate rate constants fixed based on independent investigation of reaction products.*

The reactivity of phenol under analogous conditions but with a PMO catalyst derived by calcining Mg/Al (3/1) hydrotalcite without copper was about twenty times slower. After 18 h, GC analysis showed that 68% of the phenol was still present, the remainder being anisole (12%), cresol (2%) some unidentified lower retention time (RT) species thought to be monomers (<1%) and higher RT products that were dimeric (5%) (see appendix B2). These products are consistent with the findings of Crocella et al.[12]

Global kinetics analysis of the temporal profiles for phenol reactions resulted in the reactivity network in scheme 3.1. As discussed later in this chapter, these results show that phenol is particularly susceptible to aromatic hydrogenation under the catalytic conditions. As shown in scheme 3.1, there are two likely routes to methylcyclohexanol from primary phenolic products: methylation of cyclohexanol and hydrogenation of cresol. To verify the rates of these secondary reactions, separate sets of experiments were carried out for cyclohexanol and for cresol. The results of the cyclohexanol experiment are described in section 3.7.

In the case of cresol, more than half (51%) was consumed after four hours. The results of the kinetics analysis are given in scheme 3.2 and the product details can be found in appendix B3. Of the total mixture after 4 h, dimethylphenol (xylenol) was the major product (33%) followed by methylcyclohexanol (6%) and methylmethoxybenzene (5%). These results indicate that ring methylation significantly slows the hydrogenation of the phenolic derivative. Thus, the principal products from the long-term reaction of phenol under the described conditions are MCHs formed by methylation of the cyclohexanol(s) resulting from phenol hydrogenation.

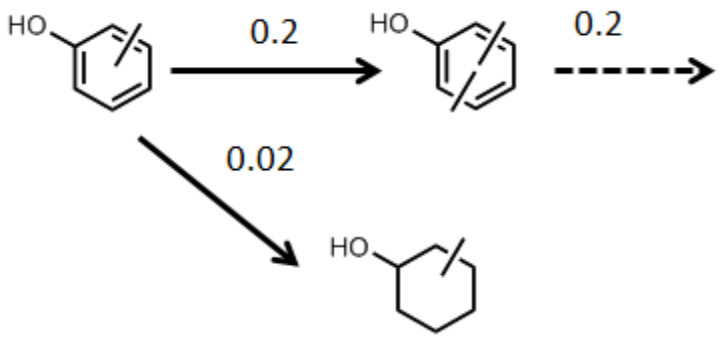

Scheme 3.2: *Reaction network for cresol: (1 mmol substrate, 100 mg Cu20PMO, 3 mL MeOH, 310 °C). Observed rate constants are shown for each step, in units of h^{-1}. Dashed lines indicate conversion to unidentified compounds.*

In analogy to phenol, guaiacol (2-methoxyphenol) displayed more complicated reaction sequences under these conditions. The most important initial steps were methylation of the phenolic oxygen to give veratrol (dimethoxybenzene), and hydrogenolysis of the C_{aryl}-OCH_3 bond to give phenol. After 3 h, guaiacol was largely (92%) consumed, with the major products being veratrol (18%), cyclohexanol (15%), cyclopentylmethanol (14%) and phenol (11%). Lesser products that are likely derived from those formed initially are cyclohexanediols (11%), methylcyclohexanols (5%), 2-methoxy-4-methylphenol (methyl anisole) (5%), dimethylcyclohexanol (4%), dimethylphenols (2%), 2-methoxycyclo-hexanone (3%), anisole (2%) as well as others (see appendix B4). Although not observed as an intermediate by GC-MS analysis, catechol is a likely intermediate species, given the appearance of both 1,2-cyclohexanediol and cyclopentylmethanol in the final reaction mixture consistent with mechanisms proposed by Deutsch and Shanks,[14] as well as by Lercher et al.[15] Scheme 3.3 illustrates the key steps for the substrate guaiacol, deduced by the kinetics analysis.

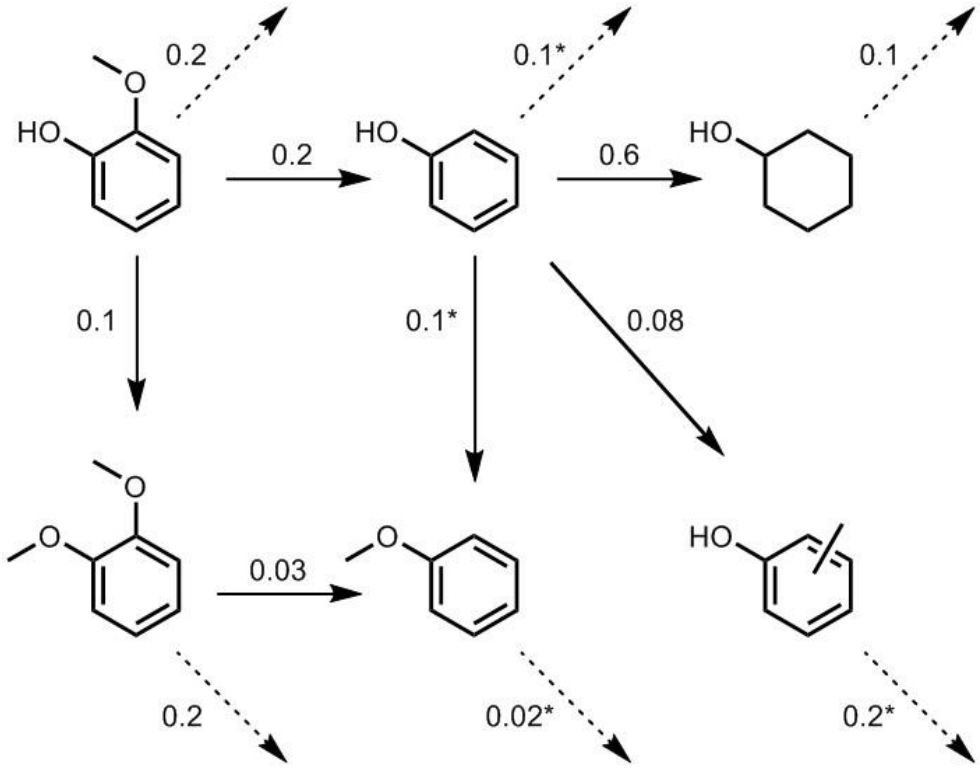

Scheme 3.3: *Reaction network for guaiacol: (1 mmol substrate, 100 mg Cu20PMO, 3 mL MeOH, 310 °C). Observed rate constants are shown for each step, in units of* h^{-1}*. Dashed lines indicate conversion to unidentified compounds. Asterisks indicate rate constants fixed based on independent investigation of reaction products.*

3.4 Reactions of Alkoxy Aromatics

Both anisole (methoxybenzene) and ethoxybenzene proved to be dramatically less reactive than phenol or guaiacol under typical catalysis conditions. Notably, ring hydrogenations were observed to a much smaller extent than with the phenolics, and the predominant pathway was aromatic ring HDO.

For anisole, only 5 % of the substrate was consumed in the first 3 h. Notably, the primary product (by far) was benzene, formed by C_{aryl}-OMe bond hydrogenolysis. The others (cyclohexanol, 2-methyl-cyclohexanol and methylcyclohexane) apparently result from CH_3-O bond hydrogenolysis followed by reactions of the intermediate phenol. At longer reaction times (6 h), a modest amount of the ring-hydrogenated methoxy-cyclohexane (~2%) was also observed (see appendix B5).

Similarly, ethoxybenzene showed preferential hydrogenolysis of the C_{aryl}-OEt bond, affording the HDO product benzene as the major product, and a low rate of ring hydrogenation (3% after 6 h). After 6 h, only 12% of this substrate was consumed. The products were benzene (6%), ethoxycyclohexane (3%), cyclohexanol (1%), 2-methyl-cyclohexanol (0.7%) and several unknowns (see appendix B6).

Veratrol (1,2-dimethoxybenzene) proved to be considerably more reactive than anisole; however, the principal pathway is aromatic hydrodeoxygenation (HDO) to give anisole and not ring hydrogenation. After 3 h, 52% was consumed; after 12 h, this rose to 97%. The predominant product was anisole (40% after 3 h), apparently formed via C_{aryl}-OMe bond

hydrogenolysis. The anisole yield peaked at ~12 h then diminished, very likely owing to slow hydrogenolysis to benzene and hydrogenation to methoxycyclohexane. Other products after 3 h included cyclohexanol (3%), 2-methylcyclohexanol (3%), benzene (2%), dimethyl-cyclohexanol (1%), methoxycyclohexane (1%) and cyclohexane (0.9%) (see appendix B7). Direct hydrogenation to 1,2-dimethoxycyclohexane was not observed. Scheme 3.4 illustrates the key steps for the substrate veratrol, as suggested by kinetics analysis.

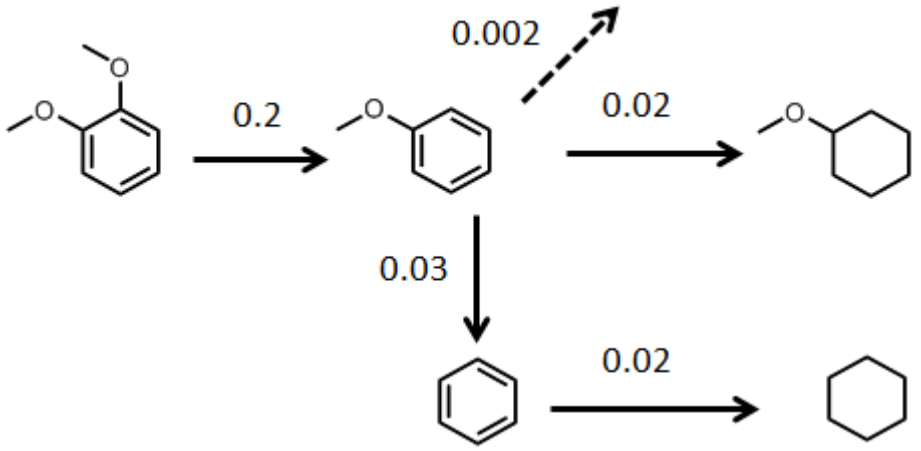

Scheme 3.3: *Reaction network for veratrol: (1 mmol substrate, 100 mg Cu20PMO, 3 mL MeOH, 310 °C). Observed rate constants are shown for each step, in units of h^{-1}. Dashed lines indicate conversion to unidentified compounds.*

3.5 Simpler Aromatics and Those with Pendant Functional Groups

The oxygen-free aromatics benzene and toluene displayed very little reactivity under the conditions effective for catalytic lignin disassembly. For example, when toluene was the substrate, 99% remained after 3 h at 310 °C. Methylcyclohexane (1%) was the only product detected. Benzene was similarly unreactive (2% conversion to cyclohexane after 3 h).

In contrast, benzyl alcohol proved to be quite reactive (full conversion after 3 h), but primarily toward HDO, as illustrated in eq. 3.1. Toluene was the principal product (>98%), but small amounts of methylcyclohexane and cyclohexylmethanol were also found. While traces of an unidentified product were also seen, ring methylation clearly plays a very minor role and hydrodeoxygenation of the benzylic OH is the main pathway, in line with the earlier findings.[14]

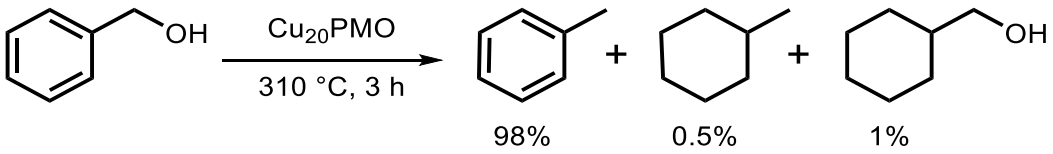

(3.1)

Styrene is also very reactive, but solely toward vinyl hydrogenation to give ethyl benzene selectively (>99% after 3 h). Traces (< 1%) of ethylcyclohexane were found, but no ring methylation products were detected

Under analogous conditions, acetophenone (acetyl-benzene) also gave full conversion after 3 h; the primary pathway was the formation of ethylbenzene (82%) (eq. 3.2), which likely took place via ketone hydrogenation to 1-phenylethanol, followed either by direct hydrogenolysis of the C-OH bond or by dehydration to styrene, then hydrogenation. Another

significant product was n-propylbenzene (16%), presumably the result of acetyl group methylation (perhaps via the enol isomer) followed by HDO. Interestingly, sec-butylbenzene was also identified as a minor (0.5%) product.

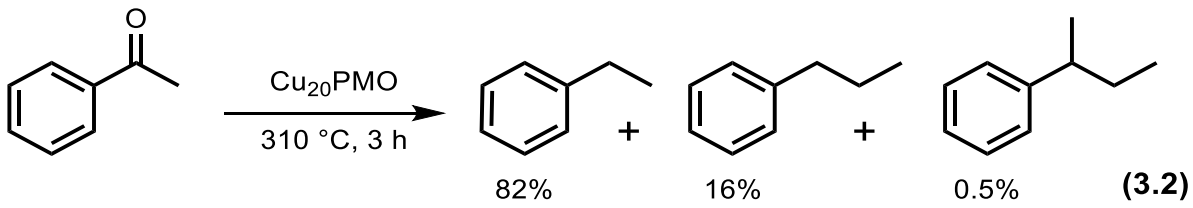

(3.2)

3.6 Model Compounds with Two Aromatic Rings

Three model compounds with two aromatic rings were investigated: diphenyl ether (DPE), benzyl phenyl ether (BPE) and 2-phenoxy-1-phenylethane-1-one (1).

DPE proved to be more reactive than anisole or ethoxybenzene, but much less so than phenol, guaiacol or veratrol. After 3 h, 23% was consumed. The first hydrogenolysis step of DPE would give equal amounts of benzene and phenol. Accordingly, benzene was 48% and phenol 4% of the breakdown products. The other products, cyclohexanol (28%), 2-methylcyclohexanol (15%) and much smaller quantities of anisole (2%), cyclohexane (1%) and dimethylcyclohexanol (1%), can largely be attributed to subsequent reactions of the phenol intermediate (scheme 3.4).

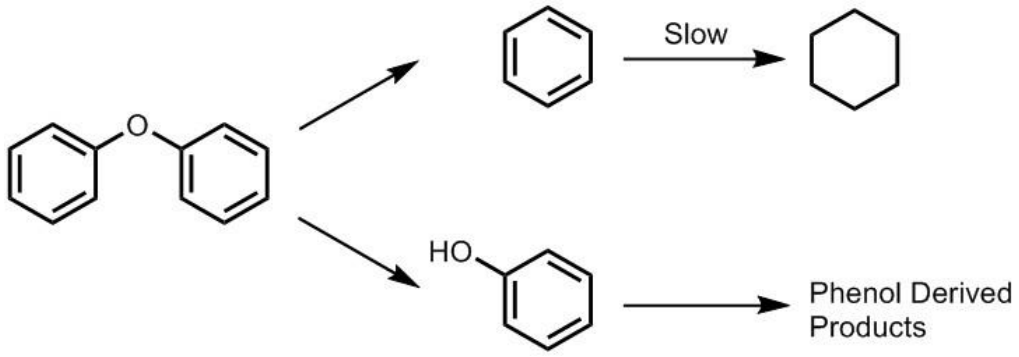

Scheme 3.4: *Observed reaction pathway for diphenyl ether (DPE).*

BPE proved much more reactive. With only 50 mg catalyst, this substrate was about 85% consumed after only 1 h, and none was left after 3 h. Carbon-oxygen bond hydrogenolysis of BPE should lead either to benzene plus benzyl alcohol or to toluene plus phenol, depending upon which C-O bond is cleaved.

The data summarized in Figure 3.4 (see appendix B8) show that toluene is formed immediately in nearly stoichiometric quantities, while the other principal (initial) product is phenol. Thus, the predominant first step is C_{benzyl}-O hydrogenolysis. As expected, the phenol is consumed by subsequent reactions (scheme 3.4) giving (mostly) non-aromatic products by the end of the reaction.

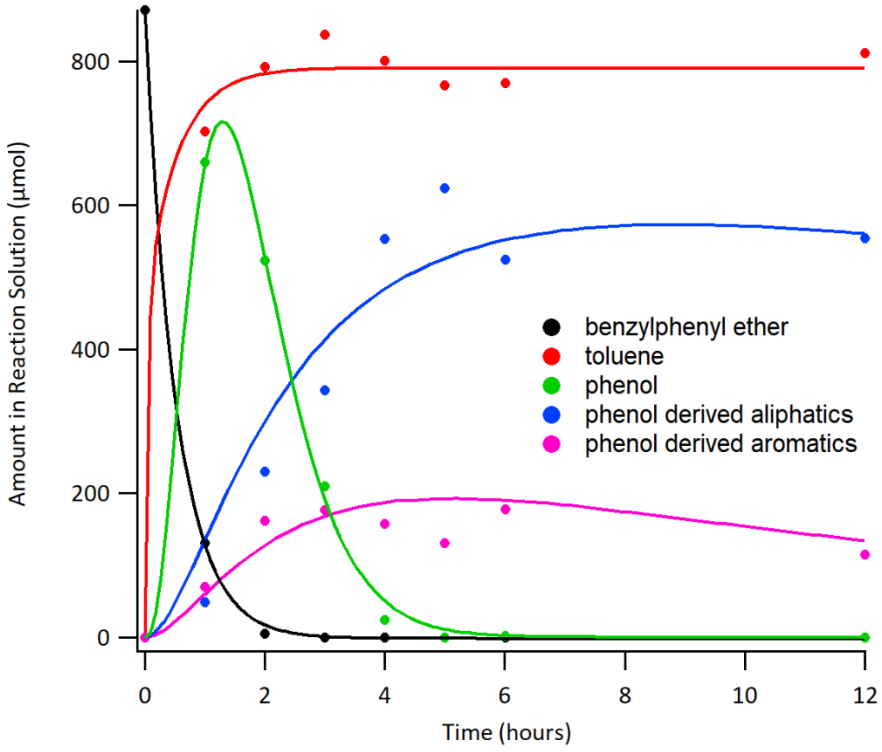

Figure 3.4: *Temporal evolution of products during Cu20PMO-catalyzed reactions of benzyl phenyl ether (ca. 1 mmol). Total material balance was 82% after 18 h.*

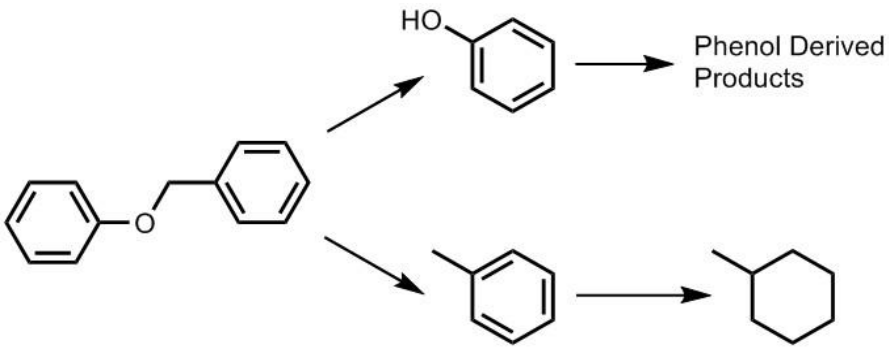

Scheme 3.4: *Observed reaction pathways for benzyl phenyl ether.*

As with phenol, the reactivity of benzyl phenyl ether under analogous conditions over 3:1 Mg/Al PMO proved to be considerably less than over Cu20PMO (see appendix B9). These reactions also indicated a very different product progression. Ether cleavage was an order of magnitude slower, with 41% of the BPE unreacted after 6 h. Thus, the clean ether hydrogenolysis, which is a hallmark of Cu20PMO, is indeed dependent upon the copper dopant. Surprisingly some toluene is formed, but unlike the case with CuPMO, this did not appear concurrently with the loss of the BPE. The later formation of toluene indicates that, in this case, it is clearly a secondary product. Longer RT products shown by GC-MS to be other dinuclear species were also formed. A possible mechanism could be analogous to the one described by Pelzer et al.,[16] where hydrolysis (made possible by residual water) converts BPE to phenol and benzyl alcohol. The poor material balance at longer reaction times and the higher molecular weight products are consistent with the pathways proposed by Pelzer et al. Given that the undoped PMO is ineffective in lignin disassembly, the origins of these secondary reactions were not pursued further. Since the magnitude of these reactions is considerably slower, they will also not have a significant effect in determining the most reactive species by global fitting kinetics. It is likely however, contribute to the < 15% variance over time not explained by this analysis (see discussion on fitting in chapter 2)

On turning to 2-phenoxy-1-phenylethane-1-one (**1**), the above studies offer some expectations regarding reaction pathways for this more complex substrate. Based on the results for acetophenone and of benzyl phenyl ether, one would expect the two fastest reactions for **1** (1000 µmol) to be carbonyl group hydrogenation to give 2-phenoxy-1-phenylethanol (**2**) (pathway (a) in scheme 3.5) and direct hydrogenolysis of the CH_2-O bond to give acetophenone and phenol (pathway b).

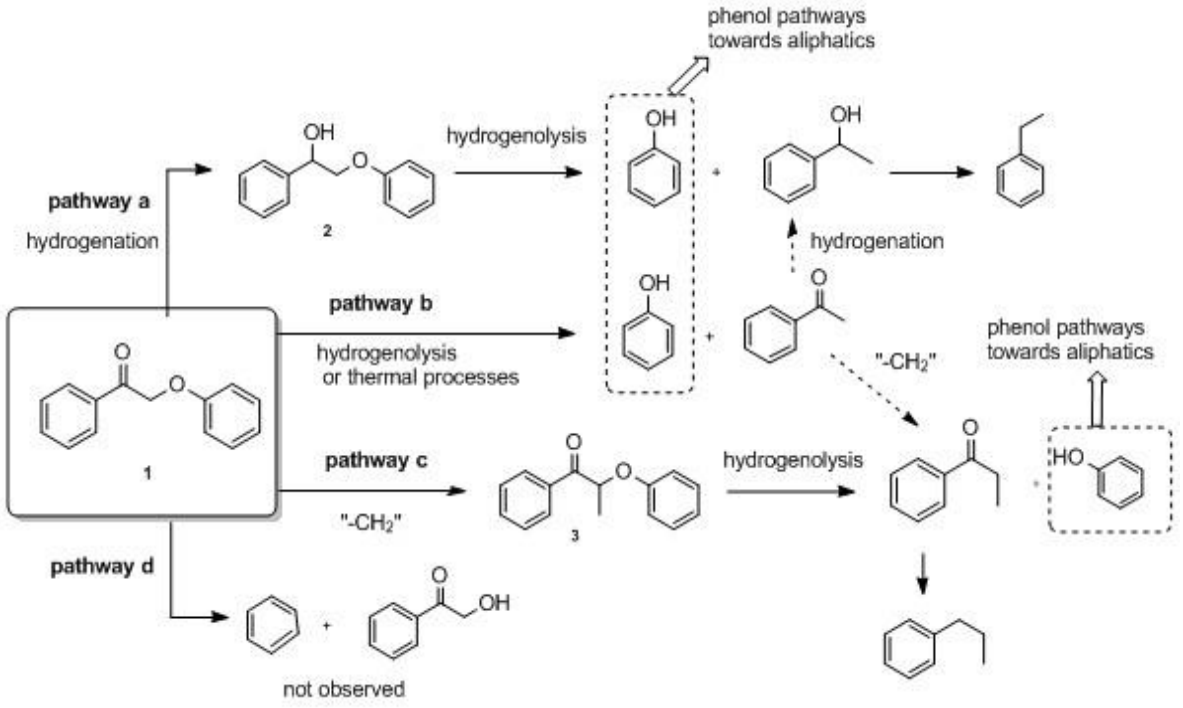

Scheme 3.5: *Likely steps in disassembly of 2-phenoxy-1-phenylethan-1-one (1).*

Subsequent hydrogenolysis of **2** would first give 1-phenyl ethanol plus phenol, and rapid HDO of the former would give ethylbenzene. Notably, ethylbenzene (600 mmol) represents the most plentiful product from **1** under these conditions (appendix B10), but it is notable that both pathway (a) and (b) predict this product given the expected reactivities of the respectively proposed 1-phenylethanol and acetophenone intermediates. The substantial quantities of 2-methylcyclo-hexanol (350 µmol) and cyclohexanol (250 µmol) products point toward phenol as a reactive intermediate.

Notably, the second most plentiful product after ethyl-benzene is propylbenzene (300 µmol, appendix B10), and this can best be explained by pathways (b) or (c). In pathway (b), the acetophenone intermediate might undergo methylation and subsequent HDO of the formed propyl-phenyl ketone. Indeed, this product was also observed when acetophenone was used

as substrate. Alternatively, it appears that **1** might undergo facile methylation of the methylene adjacent to the carbonyl (pathway c) to give compound **3**, in analogy to the reaction proposed for acetophenone. Once formed, **3** could undergo steps analogous to pathways (a) or (b) to give propylbenzene plus phenol-derived products.

Pathway (d), the scission of the phenyl ether bond to give benzene, would not be not expected given the reactivity pattern seen for benzyl-phenyl ether. This suggestion was confirmed by the observation of very little benzene in the product mixture (appendix B10); thus, (d) must play at most a minor role.

3.7 Aliphatic Alcohols and Ketones

The above di-aromatic model compounds as well as oxygenated simple aromatics have provided ring hydrogenation products, mainly cyclohexanol, which originates from phenol hydrogenation. Thus, the reactivities of such derivatives were further investigated to probe the origin of major products such as the methyl-cyclohexanols.

Cyclohexanol, the expected result of phenol hydrogenation, proved to be quite reactive. Analysis after 1 h reaction under the standard conditions found that 12% of that substrate was consumed; after 3 h, this increased to 36%. Methylated cyclohexanol was by far the dominant product initially formed (see figure 3.5 and appendix B11).

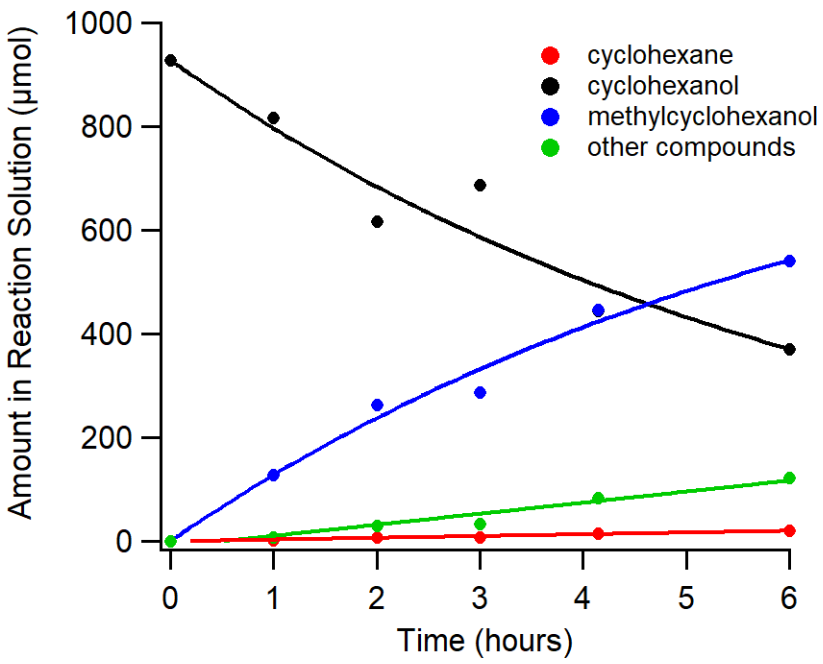

Figure 3.5: *Temporal evolution of products during Cu20PMO-catalyzed reactions of benzyl phenyl ether (ca. 1 mmol). Total material balance was 82% after 18 h.*

2-Methylcyclohexanol was somewhat less reactive than cyclohexanol with only 19% being consumed after 3 h. The principal products were dimethylcyclohexanols (13%) 2-methylcyclohexanone (3%), methylcyclohexane (1%), 2-methyl-1-methoxycyclohexane (0.6%) and unknowns (<2%).

The formation of a cyclohexanones as minor products in several cases suggests that the cyclohexanols undergo reversible dehydrogenation to the ketone analogs (eq. 3), followed by methylation at the β-carbon. If so, cyclohexanone itself should be very reactive toward ring methylation as well as to (reversible) ketone hydrogenation. This proved to be the case when cyclohexanone was used directly as the substrate. After 3 h, the starting material was mostly

consumed, and the product mixture contained 2-methylcyclohexanol (55%), cyclohexanol (22%) and dimethylcyclohexanols (13%) and the lesser products, 2-methylcyclohexanone (2%), methyl-cyclohexane (2%) and cyclohexane (1%).

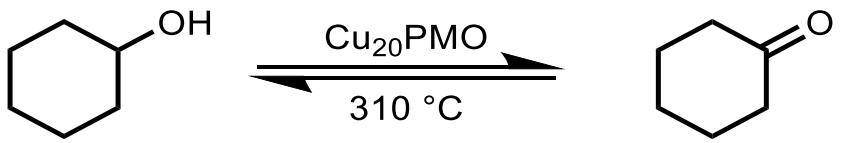

(3.3)

Not surprisingly, a mixture of cis- and trans-1,2-cyclohexanediol gave an even larger collection of products. Of particular interest was the ring contraction product cyclopentylmethanol (12%), which is possibly the result of a pinacol rearrangement.[39,40] The same product was seen when guaiacol was the substrate (see above).

3.8 Overview of Kinetics Results

Scheme 3.6 is a nearly comprehensive reactivity network, compiled from the most significant individual networks described above, while table 3.1 compares calculated rate constants in terms of reaction and substrate types (a more detailed network is given in appendix B12).

The k's determined for individual steps and measured for different initial substrates are statistically self-consistent. Not only does this allow for comparisons across the whole network, but it is also an indicator that any competitive effects to the observed kinetics under these conditions must be minimal. Such global quantification thus allows one to identify key pathways leading toward or away from the desirable aromatic products when this catalytic system is employed for lignin disassembly.

For example, hydrodeoxygenation via hydrogenolysis is quite fast with benzylic alcohols, but much slower with the cyclohexanols or phenol. For phenol, ring hydrogenation and methylation are the dominant pathways. In contrast, these are suppressed for anisole and ethoxybenzene to the point where slow HDO to the even less reactive benzene is the most significant reaction. Ring methylation of phenols contributes to product proliferation. However, since cyclohexanols are end-products of phenolic hydrogenation, the relatively fast methylations of the latter (via a cyclohexanone intermediate) have a major impact on product distributions.

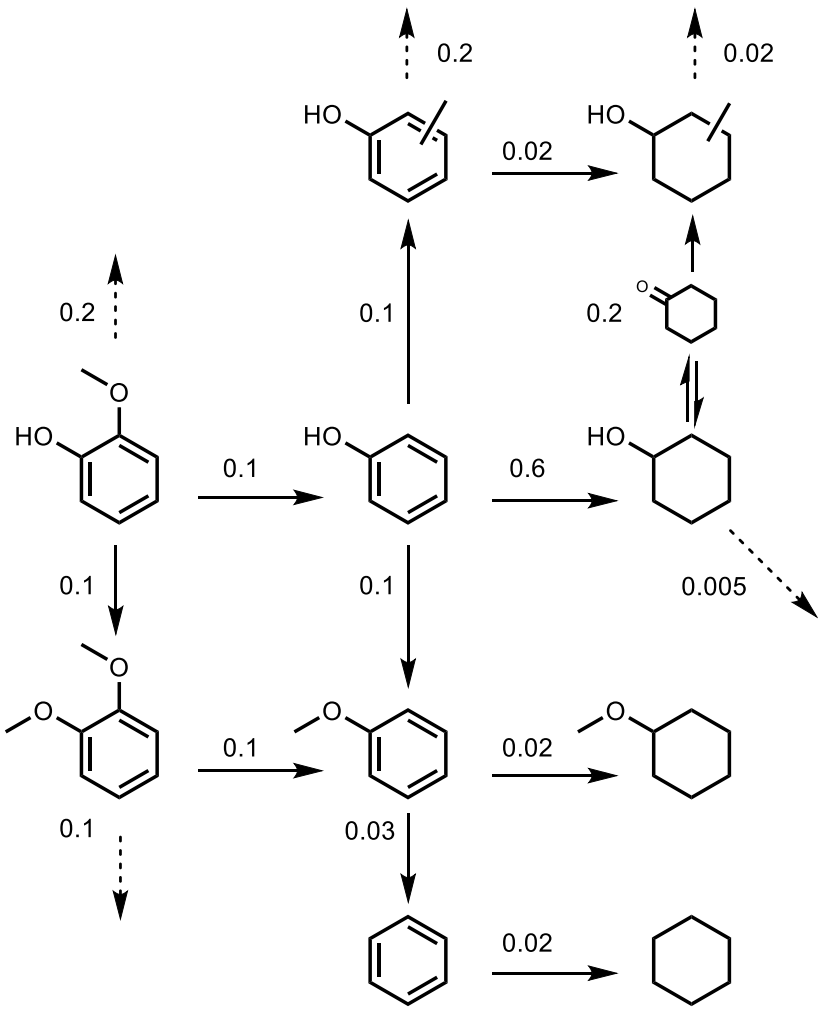

Scheme 3.6: *Reaction network for simple mono-aromatic lignin modelcompounds over Cu20PMO.*

Qualitative Rate	k_{obs} (h^{-1})	Reactions
Fastest	> 1.0	Benzyl phenyl ether hydrogenolysis
		Styrene hydrogenation
		Benzylic alcohol hydrodeoxygenation
Fast	0.75 - 0.2	Phenolic hydrogenation
		Cyclohexanol methylation
Slow	0.10 - 0.05	Phenolic methylation
		Cresol methylation
Slowest	<0.05	Other aromatic hydrogenation
		Aryl phenoxy hydrogenolysis
		Phenolic hydrodeoxygenation

Table 3.1: *Overview of k_{obs} trends observed with 1 mmol substrate, 100mg Cu20PMO, and 3 mL MeOH, at 310 °C.*

Since phenolic derivatives are inevitable outcomes of reductive lignin disassembly, one must address the facile ring hydrogenation and methylation of these species in order to enhance the yield of aromatics. Possible scenarios might include designing a HDO co-catalyst to be very active toward phenols,[34] modifying the catalyst composition to suppress phenolic hydrogenation, or chemically trapping such intermediates. The third approach was investigated by using dimethyl carbonate (DMC), a known methylating agent,[17-19] as a cosolvent.

The reaction with BPE as the substrate was run under otherwise typical conditions in a solution prepared with 2 mL MeOH and 1 mL DMC. After 1 h, the benzyl phenyl ether was 89% consumed, with the concurrent production of toluene, phenol and anisole (figure 3.6). Also found were traces of cresols and aliphatic compounds previously shown to be derived from phenol. By 6 h, the BPE was completely converted with the primary products being

toluene (900 µmol) and anisole (490 µmol); thus, O-methylation of phenol channeled the products away from ring hydrogenation.

The reactivity network in scheme 3.7 was drawn from the temporal evolution of products shown in figure 3.6. Thus, it is clear that the percentage of phenol-derived aromatics, mostly in the form of anisole, is dramatically higher than observed in methanol alone (figure 3.4) under otherwise comparable conditions.

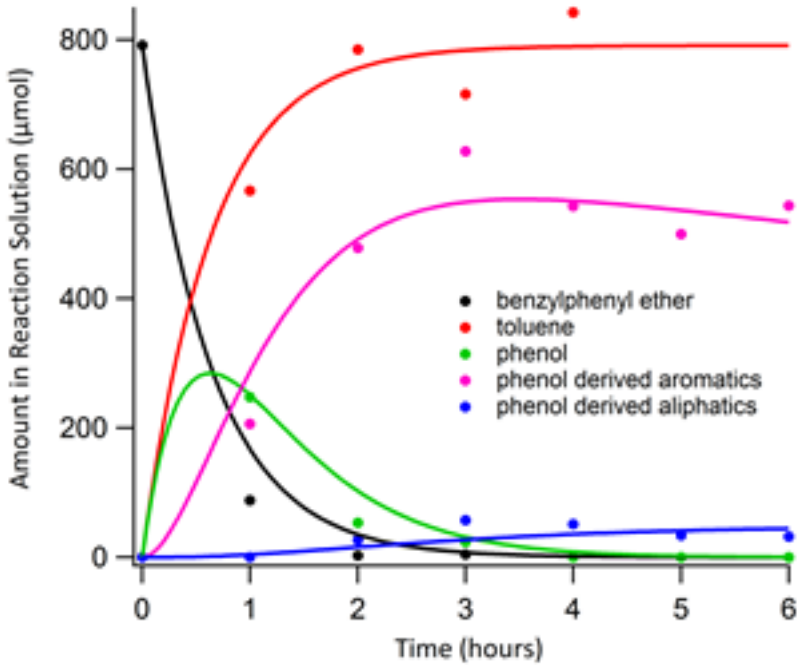

Figure 3.6: *Temporal product evolution for the reactions of benzyl phenyl ether in 2 : 1 MeOH: dimethyl-carbonate over Cu20PMO (300 °C). Material balance was 93% after 18 hours.*

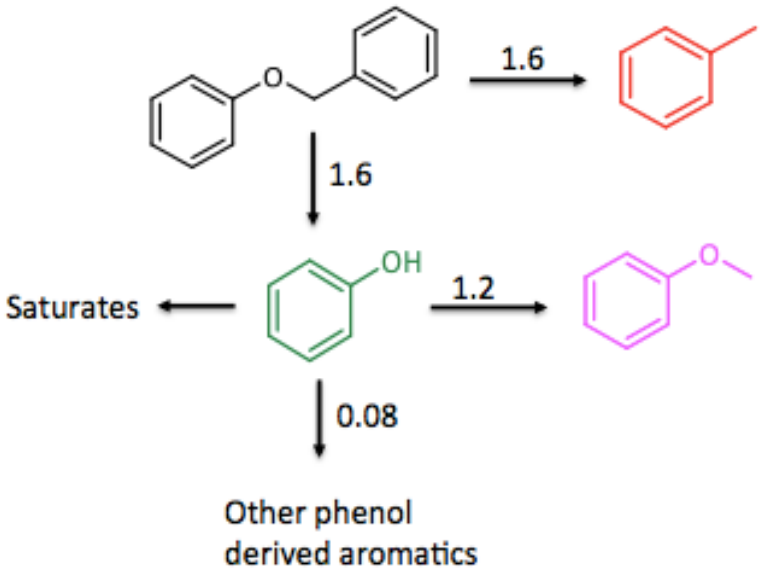

Scheme 3.7: *Reactivity network for benzyl phenyl ether with Cu20PMO in 2 : 1 MeOH:DMC (300 °C).*

Since the mini-reactor experiments summarized in figure 3.6 have less methanol (2 mL) than was used to gather the data described in figure 3.4, it was deemed it important to compare two systems containing the same quantities of MeOH. Figure 3.7 illustrates the product yields determined by GC-FID for the reactions of BPE over Cu20PMO after side-by-side reaction for 12 h under identical conditions, one with only 2 mL of MeOH as solvent the other with 3 mL of 2:1 MeOH:DMC. Clearly the aromatics yield proved dramatically higher in the latter case owing largely to the interception of the phenolic intermediates. Because the support is known to facilitate methylation by DMC, an analogous control was performed with Mg/Al PMO catalyst. The results from this control parallel those with benzyl phenyl ether reactions without DMC: the copper doped catalyst is significantly more efficient at ether cleavage and

inhibition of condensation products. The products that are apparent in this control do show a higher degree of o-methylation which is to be expected in the presence of DMC.

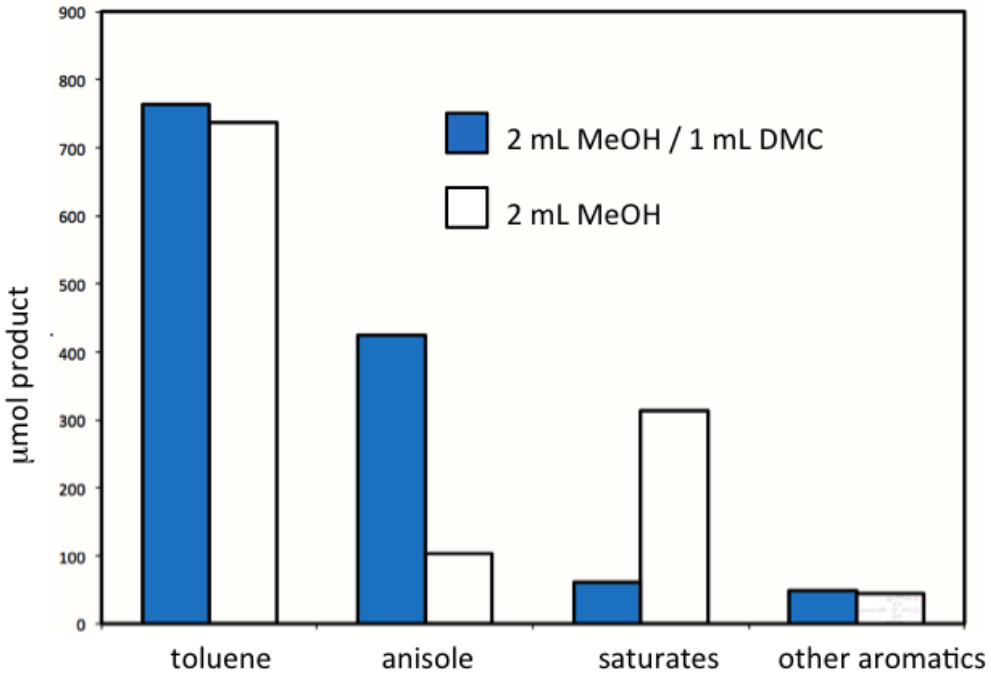

Figure 3.7: *Changes in product distribution upon using dimethyl carbonate as a cosolvent vs. using MeOH only. Products after 6 h reaction.*

3.9 Summary of Reactivity Studies

The model systems quantitatively elucidated here clearly demonstrate four key substrate reactions catalyzed by Cu20PMO under conditions where clean lignin and lignocellulose disassembly has been demonstrated.[1,10,20] Two of these are generally desirable, namely hydrogenolysis of aryl ether bonds and hydrodeoxygenation. The other two, aromatic hydrogenation and methylations of aromatic rings and of aliphatic carbons in positions adjacent to alcohol or ketone functionalities, lead to a proliferation of products, hence lower selectivity. Phenolic compounds, especially phenol, are susceptible to aromatic ring hydrogenation and methylation, thus are precursors to cyclohexanols that undergo subsequent

methylation. In contrast, simpler aromatics such as benzene and toluene are relatively unreactive under analogous conditions as is anisole, which primarily undergoes slow HDO to benzene.

In this context, we have demonstrated that intercepting phenolic intermediates by alkylating the aromatic -OH dramatically reduces product proliferation and aromaticity loss. While this was accomplished using DMC as a cosolvent, these observations clearly point toward strategies that will enhance selectivity by addressing phenolic reactivity. Given the complexity of lignin as a substrate, any such strategy will inevitably give multiple products; however, narrowing the distribution will improve the eventual success of biological or chemical funneling, hence the valorization of lignin.[4,21-24]

The essential role of copper in the methanol reforming that is the source of the reducing equivalents in the present system has been discussed previously.[1,10,20] However, the role of the supporting PMO is less well understood. Lewis acids have been shown to activate the aryl ether linkages to hydrogenolysis;[25,26] however, from these studies it is not clear how these would impact the other favorable and less favorable pathways of this catalytic system. For example, previous studies have demonstrated that mixed Mg/Al oxides catalyze phenol methylation.[17] Alternatively, methylation of the phenol oxygen, perhaps via catalysis by the acidic and basic sites at the support surface, would strongly affect overall reaction selectivity. Ongoing studies in our respective laboratories are addressing how the Cu-doped PMOs transform under the reaction conditions as well as how modifications of the support define reactivity and selectivity.

3.10 References for Reactivities Studies

1. K. Barta, P. C. Ford, "Catalytic Conversion of Non-food Woody Biomass Solids to Organic Liquids" *Acc. Chem. Res.,* **2014**, *47*, 1503−1512.

2. M. J. Girgis, B. C. Gates, "Reactivities, Reaction Networks, and Kinetics in High-Pressure Catalytic Hydroprocessing" *Ind. Eng. Chem. Res.,* **1991**, *30*, 2021-2058.

3. R. C. Runnebaum, T. Nimmanwudipong, D. E. Block, B. C. Gates, "Catalytic conversion of compounds representative of lignin-derived bio-oils: a reaction network for guaiacol, anisole, 4-methylanisole, and cyclohexanone conversion catalysed by Pt/gamma-Al2O3" *Catal. Sci. Technol.,* **2012**, *2*, 113-118.

4. J. Zakzeski, P. C. A. Bruijnincx, A. L. Jongerius, B. M. Weck-huysen, "The Catalytic Valorization of Lignin for the Production of Renewable Chemicals" *Chem. Rev.,* **2010**, *110*, 3552-3599.

5. Q. Bu, H. Lei, A. H. Zacher, L. S. Ren, J. Liang, Y. Wei, Y. Liu, J. Tang, Q. Zhang, R. Ruan, "A review of catalytic hydrodeoxygenation of lignin-derived phenols from biomass pyrolysis" *Bioresour. Technol.,* **2012**, *124*, 470–477.

6. X. Wang, R. Rinaldi, "Route for Lignin and Bio-Oil Conversion: Dehydroxylation of Phenols into Arenes by Catalytic Tandem Reactions" *Angew. Chem. Int. Ed.,* **2013**, *52*, 11499 –11503.

7. X. Wang, R. Rinaldi, "Exploiting H-transfer reactions with RANEY (R) Ni for upgrade of phenolic and aromatic biorefinery feeds under unusual, low-severity conditions" *Energy Environ. Sci.,* **2012**, *5*, 8244-8260.

8. P. Sannigrahi, A. J. Ragauskas, G. A. Tuskan, "Poplar as a Feedstock for Biofuels: A Review of Compositional Characteristics. Biofuels" *Bioprod. Bioref.* **2010**, *4*, 209-226.

9. J. J. Stewart, T. Akiyama, C. Chapple, J. Ralph, S. D. Mansfield, "The Effects on Lignin Structure of Overexpression of Feru-late 5-Hydroxylase in Hybrid Poplar" *Plant Physiol.,* **2009**, *150*, 622-635.

10. K. Barta, T. D. Matson, M. L. Fettig, S. L. Scott, A. V. Iretskii, P. C. Ford, "Catalytic Disassembly of an Organosolv Lignin via Hydrogen Transfer from Supercritical Methanol" *Green Chem.,* **2010**, *12*, 1640.

11. P. Kuzmic "Program DYNAFIT for the Analysis of Enzyme Kinetic Data: Application to HIV Proteinase" *Anal. Biochem.,* **1996**, *237*, 260-273.

12. V. Crocella, G. Cerrato, G. Magnacca, C. Morterra, F. Cavani, L. Maselli, S. Passeri, "Gas-phase Phenol Methylation of Mg/Me/O (Me=Al, Cr, Fe) Catalysts: Mechanistic Implications Due to Different Acid-Base and Dehydrogenating Properties" *Dalton Trans.*, **2010**, *39*, 8527-8537.

13. G. S. Macala, T. D. Matson, C. L. Johnson, R. S. Lewis, A. V. Iretskii, P. C. Ford, "Hydrogen Transfer from Supercritical Methanol Over a Solid Base Catalyst: a Model for Lignin Depolymerization" *Chem. Sus. Chem.*, **2009**, *2*, 215–217.

14. K. L. Deutsch, B. H. Shanks "Hydrodeoxygenation of Lignin Model Compounds Over a Copper Chromite Catalyst" *App. Cat.*, **2012**, *447*, 144– 150.

15. W. Song, Y. Liu, E. Baráth, C. Zhao, J. A. Lercher "Synergistic effects of Ni and acid sites for hydrogenation and C-O bond cleavage of substituted phenols" *Green Chem.*, **2015**, *17*, 1204-1218.

16. A. W. Pelzer, M. R. Sturgeon, A. J. Yanez, G. Chupka, M. H. O'Brien, R. Katahira, R. D. Cortright, L. Woods, G. T. Beckham, L. J. "Broadbelt, Acidolysis of the α-O-4 Aryl-Ether Bonds in Lignin Model Compounds: A Modeling and Experimental Study" *ACS Sustain. Chem. Eng.*, **2015**, *3*, 1339-1347.

17. R. Luque, J. M. Campelo, T. D. Conesa, D. Luna, J. M. Marinas, A. A. Romero, "Catechol O-Methylation with Dimethyl Carbonate Over Different Acid-Base Catalysts" *New. J. Chem.*, **2006**, *30*, 1228-1234.

18. M. B. Talawar, T. M. Jyothi, P. D. Sawant, T. Raja, B. S. Rao, "Calcined Mg-Al Hydrotalcite as an Efficient Catalyst for the Synthesis of Guaiacol" *Green Chem.*, **2000**, *2*, 266-268.

19. J. N. G. Stanley, M. Selva, A. F. Masters, T. Maschmeyer, A. Perosa, Reactions of p-coumaryl alcohol model compounds with dimethyl carbonate. Towards the upgrading of lignin build-ing blocks. *Green Chem.*, **2013**, *15*, 3195-3204.

20. T. D. Matson, K. Barta, A. V. Iretskii, P. C. Ford, "One-Pot Catalytic Conversion of Cellulose and of Woody Biomass Solids to Liquid Fuels" *J. Am. Chem. Soc.*, **2011**, *133*, 14090-14097.

21. A. J. Ragauskas, G. T. Beckham, M. J. Biddy, R. Chandra, F. Chen, M. F. Davis, B. H. Davison, R. A. Dixon, P. Gilna, M. Keller, P. Langan, A. K. Naskar, J. N. Saddler, T. J. Tschaplinski, G. A. Tuskan and C. E. Wyman, "Lignin Valorization: Improving Lignin Processing in the Biorefinery" *Science*, **2014**, *344*, 709.

22. C. O. Tuck, E. Perez, I. T. Horvath, R. A. Sheldon and M. Poliakoff, "Valorization of Biomass: Deriving More Value from Waste" *Science*, **2012**, *337*, 695–699.

23. P. Azadi, O. R. Inderwildi, R. Farnood and D. A. King, “Liquid fuels, hydrogen and chemicals from lignin: A critical review” *Renewable Sustainable Energy Rev.,* **2013**, *21*, 506–523.

24. J. G. Linger, D. R. Vardon, M. T. Guarnieri, E. M. Karp, G. B. Hunsinger, M. A. Franden, C. W. Johnson, G. Chupka, T. J. Strathmann, P. T. Pienkos and G. T. Beckham, “Lignin valorization through integrated biological funneling and chemical catalysis” *Proc. Natl. Acad. Sci. U. S. A.*, **2014**, *111*, 12013–12018.

25. A. C. Atesin, N. A. Ray, P.C. Stair, T. J. Marks, “Ether C-O Bond Hydrogenolyiss Using a Tandem Lanthanide Triflate/Supported Palladium Nanoparticle Catalyst System” *J. Am. Chem. Soc.*, **2012**, *134*, 14682-14685.

26. T. H. Parsell, B. C. Owen, T. M. Jarell, C. L. Marcum, L. J. Haupert, L. M. Amundson, K. I. Kenttamaa, F. Ribeiro, J. T. Miller, M. M. Abu-Omar, “Cleavage and Hydrodeoxygenation (HDO) of C-O Bonds Relevant to Lignin Conversion Using Pd/Zn Synergistic Catalysis” *Chem. Sci.*, **2013**, *4*, 806-813.

Chapter IV: Temperature Tuning the Catalytic Reactivity of Cu-Doped Porous Metal Oxides with Lignin Models

4.1 Introduction to Application of Temperature Controls to the CuPMO System

As discussed in chapter I, lignin is a complex biological macromolecule that is unique among biomass components in its frequency of aromatic units and relatively high energy density. The primary barrier to lignin utilization is the efficient, and sufficiently selective, breakdown of this complex material into chemical feedstocks that could be used for sophisticated fuels or synthetic precursors. Copper-doped porous metal oxides (CuPMOs) derived by calcination of copper-doped hydrotalcites (CuHTCs) are effective catalysts for the hydrogenolysis (HDG) and hydrodeoxygenation (HDO) of these materials to organic liquids in supercritical methanol (sc-MeOH).[1,2,3] The reducing equivalents needed are generated by the concurrent catalyzed reforming of MeOH. A key advantage is that these transformations occur without forming organic chars. However, the monomeric and oligomeric fragments initially formed were found to have undergone subsequent hydrogenation of aromatic rings as well as various methylation steps. The studies in chapter 3 demonstrated that phenolic byproducts that can result from the Cu20PMO catalyzed disassembly of lignin are particularly reactive toward undesirable side reactions leading to product proliferation[4]. Based on these results one can envision several approaches to improving the selectivity of lignin disassembly with the Cu20PMO catalyst. In this context, the Ford research group explored modifications of the solvent medium,[5] and of the catalyst[6] to address this issue. The investigations in this chapter further probe the reaction kinetics of Cu20PMO catalysts with several model

substrates, and the response of these reactions to temperature. The goal was to develop deeper understanding of what parameters can be modified to control product distributions, with particular emphasis on tuning the relative rates of the hydrogenolysis and hydrogenation processes. Also described is an investigation of the temperature dependence of the methanol reforming that is an essential component of this catalytic system.

4.2 Experimental Considerations for Temperature Dependent Studies

All studies were carried out using the catalyst Cu20PMO, which was prepared by calcining at 460 ^{o}C overnight (at least 12 h) a copper-doped 3:1 Mg:Al HTC, where 20% of the Mg^{2+} had been replaced by Cu^{2+} in the synthesis.[2,7] A typical run was carried out with 1 mmol of substrate and 50 mg of the Cu20PMO with 3 mL of dry methanol and an internal standard (decane) in a sealed 10 mL volume mini-reactor.[2] After a specified reaction time at the specified temperature, the reaction was quenched by rapidly cooling the reactor, after which the reactor was opened and the products analyzed by gas chromatography with flame ionization detection (GC-FID). Products were identified by comparing the retention times to those of known standards and quantified utilizing the effective carbon number (ECN) weighting factor to evaluate the area of GC-FID peaks relative to the internal standard.[8,9] Reaction rates were evaluated by global fitting analysis and apparent activation energies (E_a's) were obtained from plots of $\ln(k_i)$ vs 1/T. Further details of the analytical methods are discussed in chapter 2.

4.3 Temperature Dependent Hydrogenolysis of 2-phenoxy-1-phenylethan-1-ol

2-phenoxy-1-phenylethan-1-ol (PPE) is a model for the β-O-4 linkage in lignin (see chapter I, section 2). Catalytic disassembly over Cu20PMO was carried out for up to 90 min, with individual time points taken at 15, 30, 45, 60, and 90 min. These sets of reactions were investigated over the temperature range 280-320 °C at 10 degree intervals with the primary goal of determining the apparent E_a for hydrogenolysis of the β-O-4 linkage. The results were the expected hydrogenolysis products of phenol and 1-phenylethanol, the latter of which undergoes rapid and reversible dehydrogenation to acetophenone under these conditions owing to the alcohol reforming capabilities of this catalyst (Scheme 4.1). At longer reactions times or higher temperatures, secondary products produced by methylation, HDO and/or hydrogenation of these compounds were also observed.

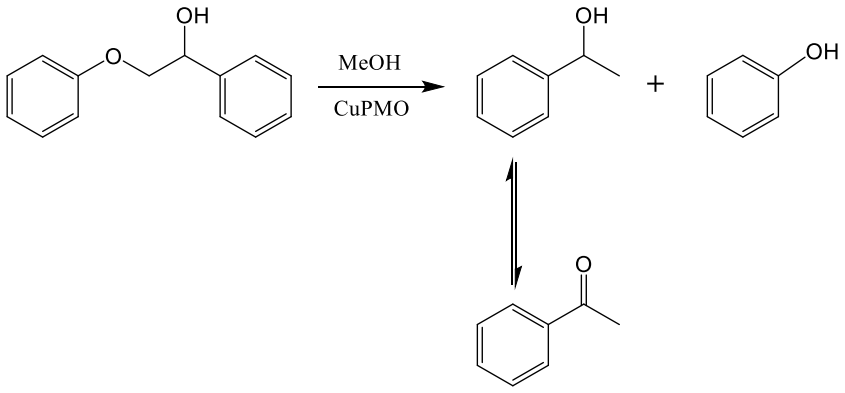

Scheme 4.1: *Observed primary products for the hydrogenolysis of PPE in supercritical methanol over Cu20PMO.*

The first notable feature of these experiments is that there was essentially no change in the PPE concentration for the first 15 min, with the exception the run carried out at 320 °C, where a measurable but small (<15%) of PPE consumption was observed (Figure 4.1, appendix C1). This lag period was attributed to the time it takes for these sealed reactors to come to the operating temperature once placed in the oven. Kinetics analyses of the primary hydrogenolysis pathways as well of secondary reactions therefore focused on processes occurring after this initial lag period.

At 280 °C, 84% of the PPE was consumed after 1 h (45 min after the 15 min lag period) with phenol, 1-phenylethanol and acetophenone constituting the major products (Appendix C1). Assuming that hydrogenolysis step shown in Scheme 1 is valid, then the initial products should be one equivalent each of phenol and 1-phenylethanol per PPE consumed. In this context, the phenol product after 1 h reaction at 280 °C represents 93% of that expected based on the consumption of PPE. Cresol, probably formed by methylation of constitutes another 4% (appendix C1). In contrast, the 1-phenylethanol and acetophenone represents 38% and 32% of that expected while identified products derived from methylation and HDO of these make up another 25%.

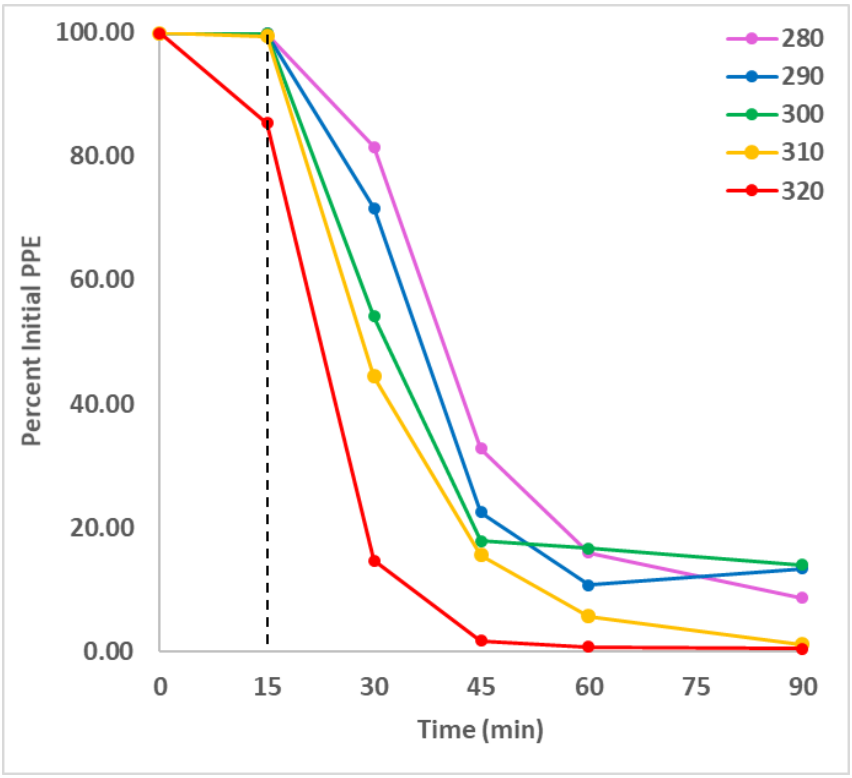

Figure 4.1: *Conversion of PPE during 90 min runs over Cu_{20}PMO at 280 to 320 ^{0}C. Over the first 15 mins there is little discernible change in PPE concentration for each of the reaction temperatures 280 to 310 ^{0}C, but at 320 ^{0}C, a small but measurable change (~15%) change was apparent over this time frame.*

Appendix C1 summarizes analogous data for PPE experiments carried out at 290, 300, 310 and 320 ^{o}C. Global kinetics analysis of the temporal evolution of reactant and products was applied at the different temperatures resulting in the first order rate constants for PPE hydrogenolysis k_{HDG} under these specific conditions. These fits take into account the observed lag period by starting the analysis at the 15 min time point. Over this temperature range, the apparent values of k_{HDG} for PPE ranged from 1.9 to 7.1 h^{-1} (appendix C2). Applying the Arrhenius equation to these temperature dependent rate constants gave an apparent E_a of 83 ± 18 kJ/mol (figure 4.2).

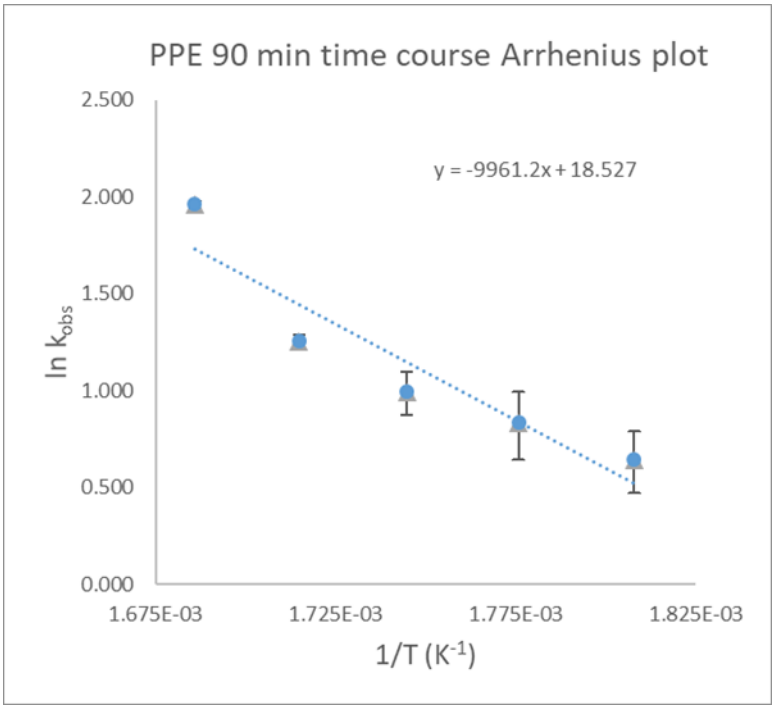

Figure 4.2: *Arrhenius plot for the hydrogenolysis of of PPE over the copper-doped porous metal oxide catalyst at 280-320 °C for shorter time runs (up to 90 min). From the slope, the apparent activation energy E_a was calculated to be 83 ± 18 kJ/mol*

4.4 Temperature Dependence of Reactions of Benzyl-Phenyl Ether

Catalytic disassembly of benzyl phenyl ether (BPE), a model for the α-O-4 linkages in lignin, was studied over two different time courses using the catalyst Cu_{20}PMO in sc-MeOH. Simple HDG of BPE should initially produce equimolar concentrations of toluene and phenol (eq. 4.1) These studies involved preparing a set of identical solutions in separate mini-reactors. For the "long" time course (6 h) reactions, data for individual time points were obtained by quenching a mini-reactor after progressive intervals differing by 1 h each. These studies were run at different temperatures (T) from 280 to 310 °C at 10-degree intervals. An analogous procedure was used for the "short" time course (120 min) reactions with individual time intervals of 30, 60, 90, and 120 min. For the shorter time course. the reactions were run at 280 to 320 °C at 10-degree intervals.

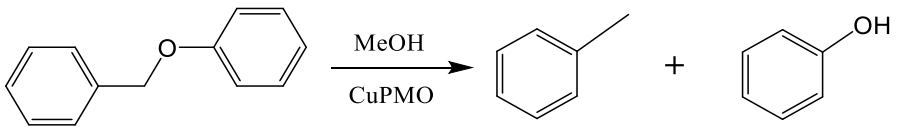

(4.1)

The 6 h time-course reactions exhibited the product evolution consistent with previous studies under analogous conditions.[4] Initial hydrogenolysis produced toluene in a stoichiometric 1:1 ratio (within error) to the BPE consumed as predicted by eq. 4.1. The phenol formed concurrently however, underwent ring hydrogenation to cyclohexanol or ring methylation to give cresol plus the much less favored O-methylation to produce anisole, which is relatively unreactive under these conditions.[4,5] The secondary products also underwent

successive hydrogenation and/or methylations to give products such as xylenol and methyl-cyclohexanol (see scheme 4.2).

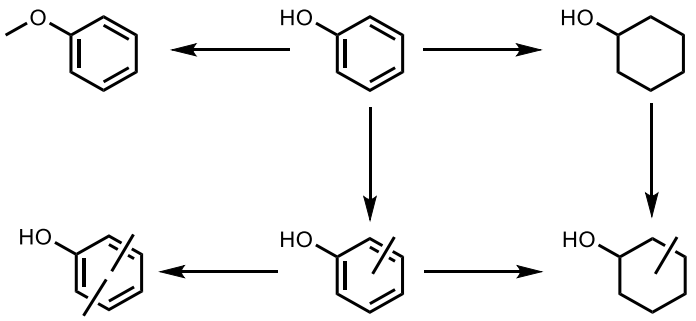

Scheme 4.2: *Observed reaction pathways for phenol in supercritical methanol Cu20PMO.*

Given the high reactivity of BPE toward hydrogenolysis, there were only small differences in BPE conversion at the different temperatures studied. After 1 h, 83% of the benzyl phenyl ether was consumed at 280 °C, while 87% was consumed at 290 °C, 91% at 300 °C, and 97% at 310 °C (figure 4.3). After 2 h, essentially all of the BPE was consumed at every temperature in this study. The evolution of the phenol-derived products from subsequent methylation and hydrogenation reactions (appendix C3) was more sensitive to the reaction conditions. At 2 h, the yield of phenol relative to the BPE consumed at 280, 290, and 310 °C was 82, 68, and 26%, respectively (figure 4.3). The shorter, 120 min time course experiments followed the pattern seen for the longer ones but provided data relevant to the initial hydrogenolysis of BPE to afford better analysis. (appendix C4). Global kinetics analysis of BPE consumption gave first order rate constants for hydrogenolysis k_{HDG} from 1.0 to 4.2 h^{-1} over the temperature range 280 to 320 °C. (appendix C5). The Arrhenius plot of these k_{HDG} values gave an apparent E_a of 91 ± 8.0 kJ/mol. (figure 4.4)

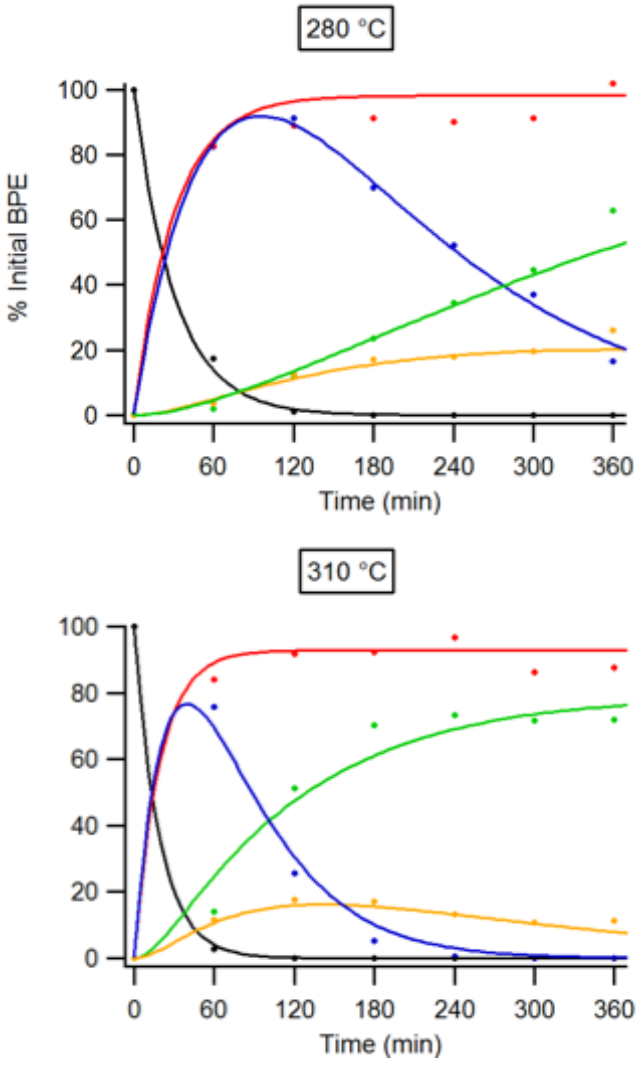

Figure 4.3: *Temporal evolution of BPE (Black), toluene (Red), phenol (Blue) phenol derived aromatics (yellow) and phenol derived aliphatics (green) products during 6 h runs of BPE over Cu_{20}PMO at 280 and at 310 ^{0}C. At both temperatures BPE is completely consumed after 2 h, however there are significantly more aromatics present when T = 280 ^{0}C*

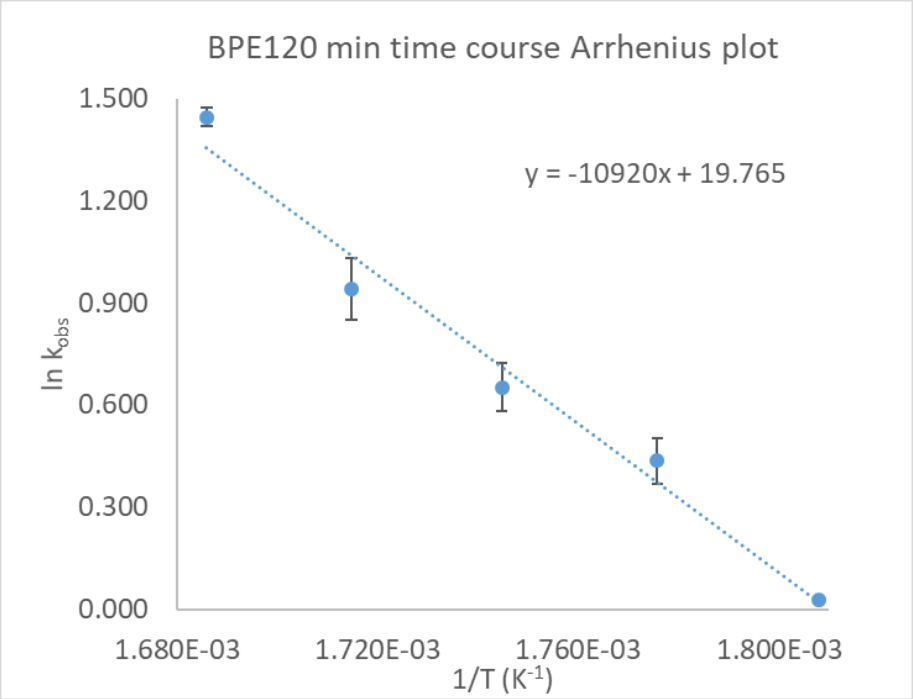

Figure 4.4: *Arrhenius plot for the conversion of benzyl phenyl ether (BPE) over the CuPMO catalyst at 280-320 °C for shorter time runs (up to 120 min). From the slope, the apparent activation energy* E_a *was calculated to be 91 ± 8 kJ/mol*

4.5 Temperature Dependence of Reactions of Phenol

The reactions of phenol were studied directly owing to its reactivity and its role as an initial product during the hydrogenolysis of BPE and PPE.[4,5] These studies were carried out for 2 h at 280-320 °C (in 10-degree intervals) with individual time points taken at 30, 60, 90, and 120 min. (appendix C6). The products of this investigation were consistent with pathways demonstrated in previous studies as shown above in scheme 4.2.[4] The rate constants for phenol hydrogenation k_{HYD}, O-methylation k_{OMe}, and aryl methylation k_{AMe} ranged from 0.023-0.70, 0.022-0.13, and 0.12-0.28 h^{-1}, respectively (appendix C7). Arrhenius plots gave apparent E_a values 228 ± 30, 108 ± 17, and 61 ± 6 kJ/mol for the subsequent phenolic ring hydrogenation, O-methylation, and aryl methylation, respectively (figure 4.5).

When compared to the reactivity of the α-O-4 and β-O-4 models BPE and PPE, ether hydrogenolysis displays considerably lower apparent E_a values (83 and 91 kJ/mol, respectively) than does the HYD pathway for phenol (228 kJ/mol). This result suggests that the relative rates of hydrogenolysis and phenol hydrogenation can indeed be affected by temperature controls.

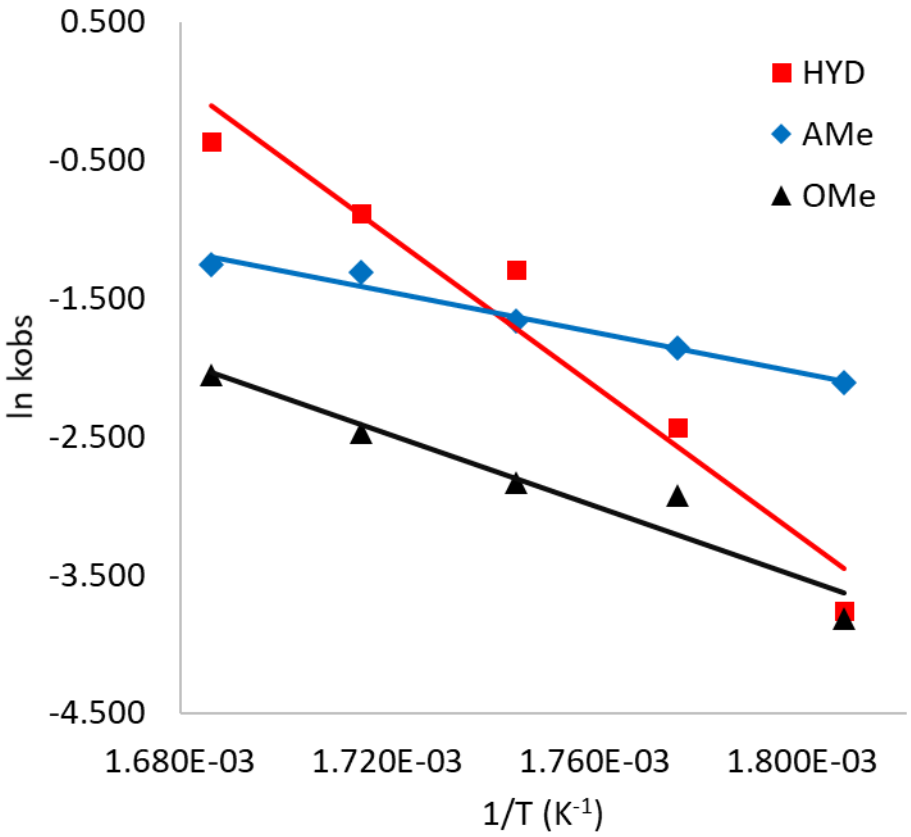

Figure 4.5: *Arrhenius plots for the competing hydrogenation (HYD), aromatic methylation (AMe) and O-methylation (OMe) of phenol over Cu_{20}PMO at 280-320 °C for shorter time runs (up to 90 min). Apparent activation energies are E_a(HYD) = 228 ± 30 kJ/mol, E_a(OMe) = 108 ± 17 kJ/mol and E_a(AMe) = 61 ± 6 kJ/mol.*

4.6 Temperature Dependence of Reactions of Dihydrobenzofuran

Catalytic disassembly of 1 mmol of dihydrobenzofuran (DHBF) over 50 mg of Cu_{20}PMO was carried out for up to 18 h, with individual time points taken at 1, 2, 3, 4, 6, 12 and 18 h. This reaction series was run at 290, 300, 320, and 330 °C. The longer time course and higher temperature range compared to BPE and PPE was reflective of the relative recalcitrance of DHBF compared to the other two models. As seen in previous studies, the initial product is the ring-opened 2-ethylphenol (EtPhOH) resulting from the hydrogenolysis of the alkyl C-O bond (scheme 4.3).[3]

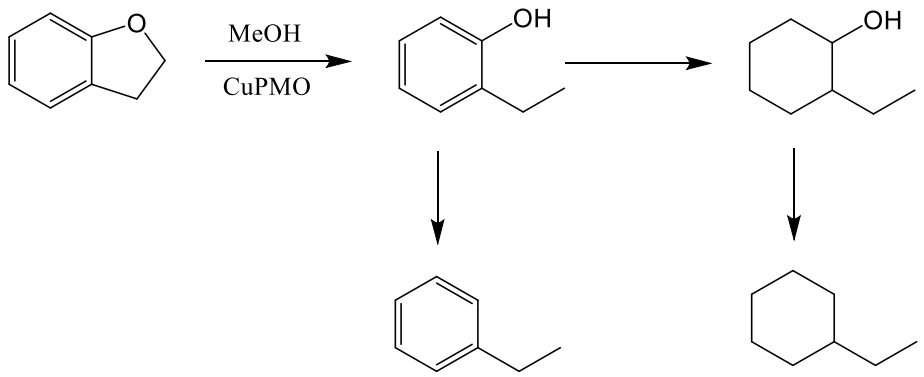

Scheme 4.3: *Observed primary products pathways for DHBF over 50 mg of Cu_{20}PMO in supercritical methanol.*

At 290 °C only 21% of the DHBF was converted after 6 h, while at higher temperature conversion over this time frame increased significantly with 70% conversion found at 320 °C. It was also possible to track the temperature dependence for the rates of the secondary reactions of the initial EtPhOH product, which underwent hydrodeoxygentation to ethylbenzene and hydrogenation to 2-ethylcyclohexanol (appendix C8 and C9). Small amounts of ethylcyclohexane were also observed, the apparent result of 2-ethylcyclohexanol

HDO. Arrhenius plots (figure 4.6) of the calculated rate constants for DHBF hydrogenolysis and subsequent reactions gave E_a(HDG) = 113 ± 13 kJ/mol and the apparent activation energies for EtPhOH hydrodeoxygenation and hydrogenation E_a(HDO) = 118 ± 11 and E_a (HYD) = 115 ± 12 kJ/mol. However, since EtPhOH hydrogenation is faster than DHBF hydrogenolysis with similar activation energies the slow HDG process is rate limiting at all the temperatures studied and that these E_a values are more likely a reflection of the HDG only.

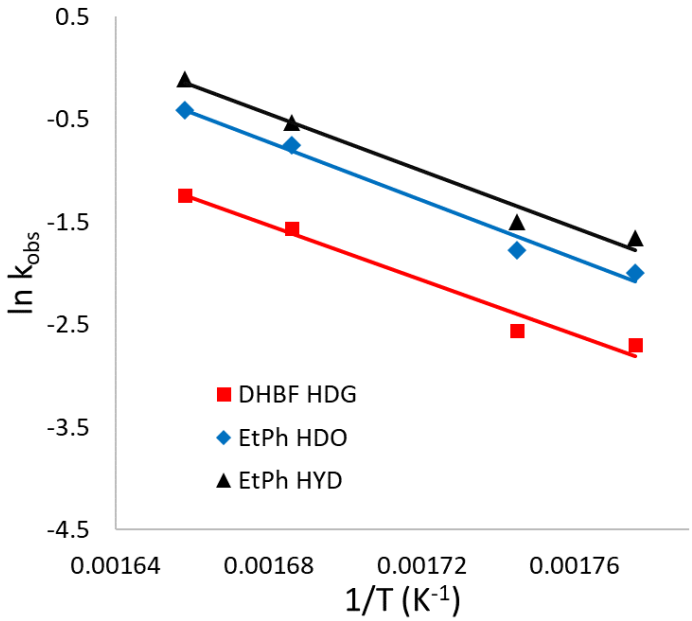

Figure 4.6: *Arrhenius plots for the conversion of dihydrobenzofuran (DHBF) and secondary reactions of 2-ethylphenol over the copper-doped porous metal oxide catalyst at 280-320 °C for shorter time runs (up to 90 min.) The apparent activation energies are for DHBF E_a(HDG) = 113 ± 13 and for ethyl phenol are E_a(HYD) = 115 ± 12 and E_a(HDO) = 118 ± 11 kJ/mol.*

4.7 Temperature Dependence of Methanol Reformation over Cu20PMO

The hydrogenolysis, hydrodeoxygenation and hydrogenation reactions for the substrates described above all depend on the formation of H_2 via methanol reforming over the Cu_{20}PMO catalyst. Given the somewhat different E_a values found for the hydrogenolysis of BPE, PPE and DHBF, it is apparent that methanol reformation itself is not rate limiting. Nonetheless, this step is still critical when considering the tuning of this catalyst since sufficient hydrogen is necessary to prevent char formation. In order to explore this matter, MeOH reformation over Cu20PMO was studied in the absence of substrate at different temperatures (280 to 320 °C in 10° intervals). In each case, the experiment was initiated with a fixed quantity of freshly calcined Cu_{20}PMO (50 mg) and 3.0 mL of MeOH in 10 mL volume mini-reactors. Individual time points were evaluated from 15 to 195 min at 30 min intervals, and the reaction dynamics were monitored by recording changes in the methanol mass, in the volume of gas produced and in the composition of the gas as evaluated by GC-TCD.

At each T studied, there was little or no change in methanol mass during the first 15 min in the reactor. This can be attributed in part to a lag period as the reactors equilibrate to the temperature of the furnace, as seen above with model compounds. Another possible (and not mutually exclusive) explanation for this lag period would be simultaneous transformation of the catalyst to a more active form. A paper in progress suggests that this is indeed the case, with the first few minutes demonstrating marked structural changes in the catalyst. After this 15 min lag period, MeOH mass loss was readily apparent, and the rate of such loss increased at the higher temperatures (figure 4.7). At the lower T's plots of MeOH mass loss versus time was roughly linear consistent with a heterogeneous catalyst operating at V_{max}. However, at higher temperatures, the MeOH mass loss appeared to level out at longer reaction times,

suggesting that, in these closed vessel batch reactions, the rate of back reaction, methanol formation, may be approaching that of the reforming processs.

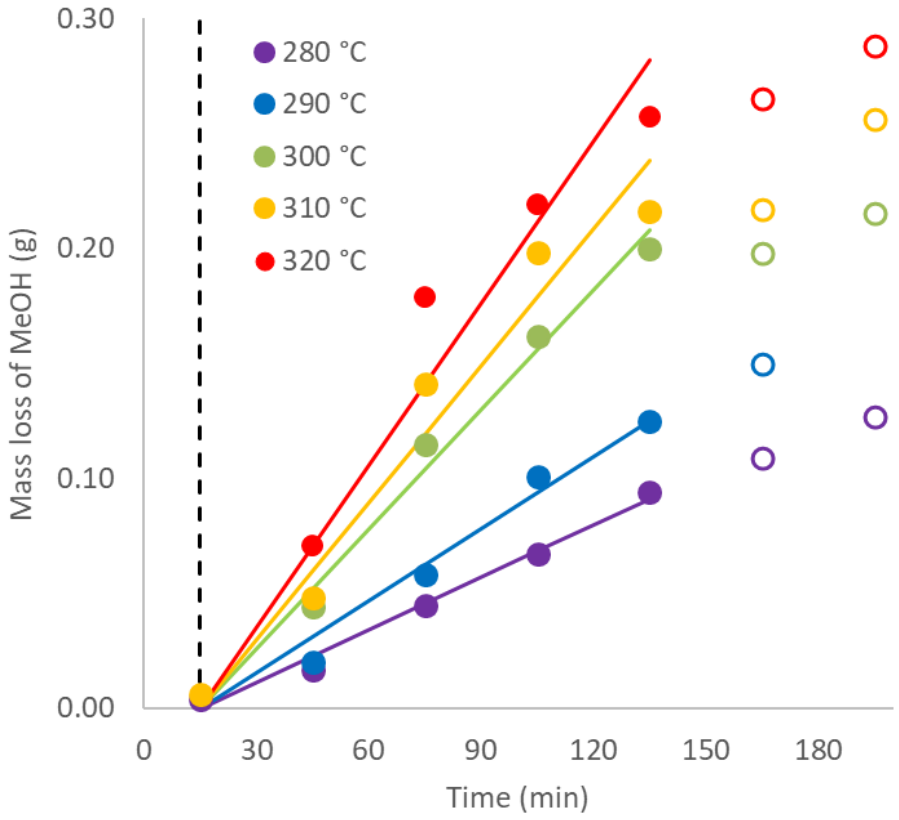

Figure 4.7: *Mass loss of methanol over Cu_{20}PMO (3 mL initial MeOH volume, 50 mg of catalyst) as a function of temperature (280, 290, 300, 310, and 320 °C). Solid markers indicate the time points that were used to calculate the TOF, with the fit lines indicated for each temperature. The open markers indicate time points not used in the fit. The dashed line emphasizes the 15 min time point where only minimal changes in MeOH mass was observed.*

Turnover frequencies (TOFs) were calculated at each T from the initial slopes of the plots in figure 4.7, giving values of 9.3, 12.7, 21.1, 24.2 and 28.6 moles MeOH consumption per mole total Cu in the catalyst per hour at 280, 290, 300, 310 and 320 °C, respectively. These values give an apparent E_a of 79 ± 10 kJ/mol for MeOH consumption.

The gas volumes generated follow a pattern similar to that for methanol consumption, namely a short lag period followed by a relatively linear period of gas production, then a slowing toward an apparent steady state. After reaction for 195 min., the volume of gas released at 295 K and 1.0 atm was 285, 355, 460, 530, and 570 mL for reactions studied at 280, 290, 300, 310 and 320 °C respectively. GC-TCD analyses was used to determine the compositions of these gas mixtures.

It is likely that MeOH reforming involves several steps, first dehydrogenation to give formaldehyde and one H_2, followed by conversion of formaldehyde into CO and another H_2. If water is present, such Cu-based catalysts will facilitate the water gas shift ($CO + H_2O == CO_2 + H_2$). A less desirable side reaction would be HDO of MeOH to CH_4 and H_2O, which we have previously reported to be a minor reaction in related systems.[3] Temperature effects on these pathways were evaluated by capturing the gas formed during a batch reaction experiment, measuring the total volume and determining the composition of aliquots by quantitative GC-TCD methods.

Figure 4.8 illustrates the evolution of the volumes and composition of the gases formed from methanol reforming in a batch reactor operating at 290 ^oC. The temporal gas volumes and compositions (H_2, CO, CH_4 and CO_2) are summarized in appendix C10 for each temperature. The gasses generated are largely H_2 and CO with the trend in CO production following that of H_2 and the H_2:CO ratio approaching ~2:1 at longer reaction times as expected

for the reforming of dry MeOH. Some CO_2 was also found, and this may be largely attributed to the water gas shift owing to the use of reagent CH_3OH that had not been dried rigorously. (Spurious H_2O contamination may be the cause of the anomalous amount of CO_2 generated in the experiment at 310 °C.) Methanol HDO would be another source of water, but this is clearly a minor side reaction given the small quantities of methane detected (appendix C10).

Figure 4.8 also demonstrates the internal consistency between the moles of gas generated and that expected from the methanol. The deviance from the expected ratio of hydrogen to the other gasses at earlier time points may be the result of incomplete conversion of formaldehyde to H_2 and CO; however, as noted above, the ratios are more closely linked to those expected later in the time course. Plots similar to Figure 4 for MeOH reforming at each temperature studied are displayed in appendix C10.

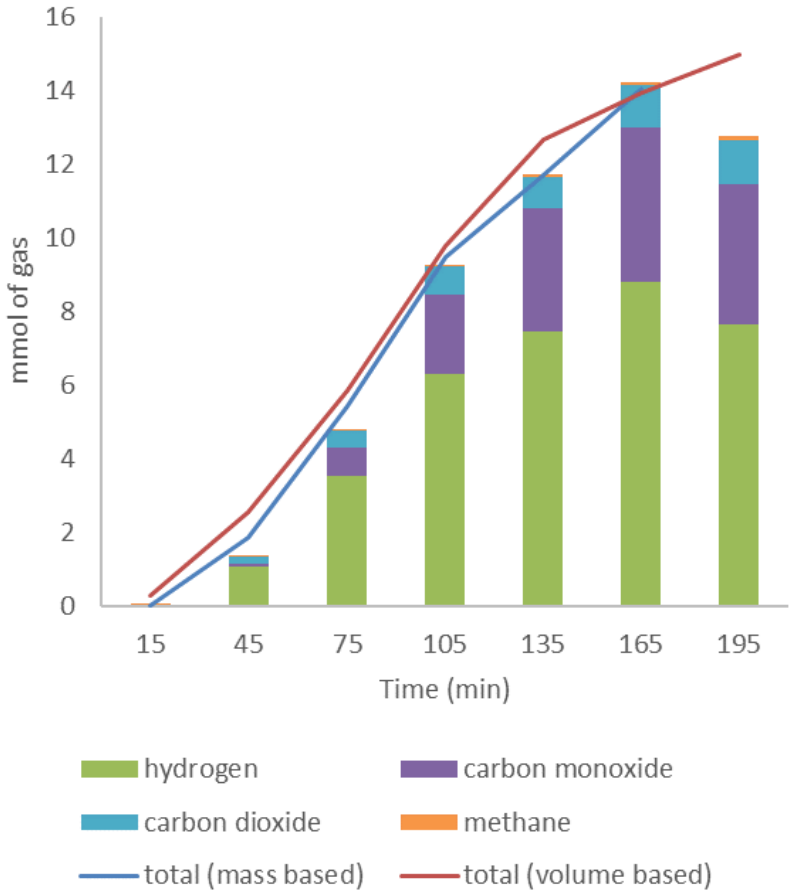

Figure 4.8: *Evolution of gaseous products from the conversion of methanol over* Cu_{20}*PMO at 290 °C. The stacked bars indicate the mmol of each gas in the total products as determined by GC-TCD. The lines indicate the theoretical total moles of gas based either the total captured volume and ideal gas law (red) or the mass loss of methanol assuming a 3:1 ratio of mol of gas produced per methanol consumed (blue).*

These studies show that production of H_2 via MeOH reforming over CuPMO and the approach to an equilibrium or steady state of the gaseous products occur on a similar time scale as the ether hydrogenolysis of the above models. The fact that first order assumptions fit well in interpreting the hydrogenolyses kinetics suggest that, while these tandem processes in the catalytic system are occurring on similar time scales, once sufficient H_2 is present, the HDG rates are not directly dependent on P_{H2}. Although the partial pressure of hydrogen increases significantly over a period of several hours, the quantity present even after a relatively short time frame is apparently sufficient to saturate the catalysis sites needed for hydrogenolysis. Furthermore, it is apparent that more hydrogen is produced than necessary for the desired ether hydrogenolysis. The excess H_2 may account for the high rates of phenolic hydrogenation. However, since excess hydrogen is needed in this system to suppress char formation, catalyst modifications or selective poisoning that simply lowers the rate of H_2 production may produce undesirable results. One could conceivably combine selective poisoning with an initial charge of hydrogen to the catalytic system to address this issue.

4.8 Summary of Temperature Tuning Studies

In summary, with regard to the α-O-4 and β-O-4 models BPE and PPE, ether hydrogenolysis displays considerably lower apparent Ea values than does the HYD pathway for the initial phenol product. On the other hand, DHBF ether hydrogenolysis has a comparable Ea at 113 kJ/mol but the individual rates were among the slowest observed in this study. The overall similarity of the observed E_a's for ether hydrogenolysis suggests a similar mechanism for these substrates, with the differences in overall rates and the trend in E_a matching the relative ether bond strengths in the individual model compounds.[22]

These studies demonstrate that lower operating temperatures and limited contact time can improve the selectivity towards aromatic products. At least from these batch reactor systems with model compounds, it is clear that one can enhance the aromatic composition of product streams by controlling reaction temperature. For example, at 290 °C the α-O-4 and the β-O-4 ether linkages in the models are largely cleaved by hydrogenolysis after 90 min, while there was relatively little hydrogenation and other secondary reactions of the initial aromatic products. However, although with genuine lignin, the β-O-4 and α-O-4 linkages between the mono-lignol fragments are the most common, there are other more recalcitrant linkages that would ensure that the products generated will be a mixture of monomers and small oligomers requiring additional processing.

With regards to the reformation of methanol to produce reducing equivalents of H_2, these studies demonstrate an observed E_a for the conversion of methanol of 80 kJ/mol. It was also observed that the continued production of H_2 during the first three hours did not affect the first order model for ether hydrogenolysis, suggesting that a sufficient concentration of H_2 is produced during the initial stages of the disassembly reactions to saturate the active sites in the catalyst. While a high rate of H_2 production is desirable to reduce char formation, it is likey that H_2 is overproduced in the batch reactions described in this study.

Notably, these studies clearly show that the distribution of products is dependent on the contact time with the catalyst. Combined with the potential for temperature and PH2 control, this points to the likely advantage of utilizing flow reactors to control the product distributions in the future.

4.9 References for Temperature Studies

1. K. Barta, P.C. Ford, "Catalytic conversion of nonfood woody biomass solids to organic liquids" *Acc. Chem. Res.* **2014**, *47*, 1503-1512.

2. G.S. Macala, T.D. Matson, C. L. Johnson, R. S. Lewis, A. V. Iretskii, P. C. Ford, "Hydrogen Transfer from Supercritical Methanol over a Solid Base Catalyst: A Model for Lignin Depolymerization" *Chem. Sus. Chem.* **2009**, *2*, 215-217.

3. T. D. Matson, K. Barta, A. V. Iretskii, P.C. Ford, "One-pot catalytic conversion of cellulose and of woody biomass solids to liquid fuels" *J. Am. Chem. Soc.* **2011**, *133*, 14090−14097.

4. C. M. Bernt, G. Bottari, J. A. Barrett, S. L. Scott, K. Barta, P. C. Ford, "Mapping reactivities of aromatic models with a lignin disassembly catalyst. Steps toward controlling product selectivity" *Catal. Sci. Tech.* **2016**, *6*, 2984-2994.

5. J. A. Barrett, Y. Gao, C. M. Bernt, M. Chui, A. T. Tran, M. B. Foston, P. C. Ford, "Enhancing aromatic production from reductive lignin disassembly: in situ O-methylation of phenolic intermediates" *ACS Sustainable Chem. Eng.* **2016**, *4*, 6877-6886

6. M. Chui, G. Metzker, C. M. Bernt, A. Tran, A. C. Burtoloso, P. C. Ford, "Probing the lignin disassembly pathways with modified catalysts based on Cu-doped porous metal oxides." *ACS Sustainable Chem. Eng.* **2017**, *5*, 3158-3169.

7. J. I. Cosimo, V. K. Diez, M. Xu, E. Iglesia, C. R. Apesteguia, "Structure and Surface and Catalytic Properties of Mg-Al Basic Oxides" *J. Catal.* **1998**, *178*, 499-510.

8. J. C. Sternberg, W. S. Gallaway, D.T.L Jones, "The mechanism of response of flame ionization detector" In ***Gas Chromatog-raphy***. N. Brenner, J.E. Callen, and M.D. Weiss, eds. Academic Press, New York, **1962**, 231-67.

9. J. T. Scanlon, D. E. Willis, "Calculation of Flame Ionization Detector Relative Response Factors Using the Effective Carbon Number Concept" *J. Chromatogr. Sci.* **1985**, *23*, 333-340.

10. K. Seonah, S.C. Chmely, M. R. Nimlos, Y. J. Bomble, T. D. Foust, R. S. Paton, G. T. Beckham, "Computational Study of Bond Dis-sociation Enthalpies for a Large Range of Native and Modified Lignins" *J. Phys. Chem. Lett.* **2011**, *2*, 2846-2852.

Chapter V: Photocatalytic Carbon Disulfide Uncaging via Charge Transfer Quenching of Quantum Dots*

5.1 Introduction to Photocatalytic Carbon Disulfide Production

Semiconductor quantum dots (QDs) exhibit size and composition dependent optical properties, strong absorption cross-sections, high photoluminescence (PL) quantum yields, and customizable solubility through surface ligand exchange.[1,2] These properties position QDs as attractive sensitizers for photodynamic therapy,[3] photo-activated drug delivery,[4,5] solar energy conversion[6] and photocatalysis.[7,8] This study describes the photocatalytic cleavage of 1,1-dithiooxalate (DTO) to CS_2 and CO_2 mediated by CdSe QDs. This process serves to "uncage" carbon disulfide (CS_2), a potentially therapeutic agent. Similar reactions are observed with the DTO ester tBuDTO, and the light activated cleavage of such ligands suggesting interesting strategies for the controlled modification of quantum dot surfaces.

There is suggestive evidence that carbon disulfide could be used for therapeutic applications. Carbon disulfide (CS_2) has similar physical properties to known bioregulatory small molecules such nitric oxide,[9-11] carbon monoxide,[12-14] and hydrogen disulfide.[15-18] Like these small molecules, CS_2 can readily form transition metal complexes.[19] Carbon Disulfide can also uniquely react with biological nucleophiles such as thiols and amines to form bridging sulfides or thiocarbamates.[20,21] Furthermore, CS_2 and its products have been shown to play a role in several biological systems. Thiocarbamates have been shown to inhibit nuclear factor

* This chapter reproduced with permission from "Photocatalytic carbon disulfide production via charge transfer quenching of quantum dots" Christopher M. Bernt, Peter T. Burks, Anthony W. DeMartino, Agustin E. Pierri, Elizabeth S. Levy, David F. Zigler, and Peter C. Ford. *Journal of the American Chemical Society*, **2014**, *136* (6), 2192–2195. Copyright 2014 American Chemical Society.

kappa-light-chain-enhancer of activated B cells (NF-κB),[22] a transcription factor essential to various physiological responses such as inflammation, immune response, cell growth, and apoptosis;[23,24] all of which are physiological roles of the previously mentioned small molecule bioregulators (NO, CO, H_2S).[11,14,16] Carbon disulfide has also been shown to interact dopamine-β-hydroxylase a vital enzyme responsible for the conversion of dopamine to norepinephrine. [25,26] Thiocarbamate complexes have also been proposed for use as an anti-cancer agent.[27] Besides these proposed therapeutic targets, other experimental results suggest an intrinsic role of CS_2 in mammals, specifically as a social learning cue in the diets of rodents.[28] As with NO, CO, and H_2S, carbon disulfide is a toxic species at higher concentrations. Like these small molecules it has neurological,[29] cardiovascular,[30] and reproductive[31] effects. Generally, this toxicity has been attributed to its aforementioned attraction to biological nucleophiles and summary protein crosslinking.[21] Interestingly, the reproductive toxicity has been related to interactions with the NO producing enzyme, Nitric Oxide Synthase.[31] Furthermore, carbon disulfide, resulting dithiocarbamates, or some other byproduct of CS_2 may be involved in several disease states such as cancer,[23] schizophrenia,[32] and HIV, a fact which might also suggest some intrinsic role at lower levels in a healthy individual.[22] The ability to balance the potential therapeutic and toxic and effects of carbon disulfide make the prospect of photochemical delivery an attractive option, allowing for dosage, spatial and temporal controls.

5.2 Synthesis of Dithiooxalate-Quantum Dot (DTO-QD) Conjugates

In these contexts, we probed DTO-QD conjugates as photochemical CS_2 precursors. These were readily prepared by exchanging DTO dianions for the myristate ligands (n-$C_{13}H_{27}CO_2^-$) originally terminating the QD surface.

5.2.1 Materials: Reagents for the synthesis of dithiooxalate ligands were reagent grade and used without further purification. Iron(III) chloride, sodium sulfide nonahydrate, 1,1,1-trichloracetic acid, benzyltriphenylphosphonium chloride, t-butyl-chloroacetate, sulfuric acid, and elemental sulfur were purchased from Sigma Aldrich. Dimethylformamide, diethyl ether, and triethylamine were purchased from EMD. Methanol was purchased from VWR. Potassium hydroxide was purchased from Fisher Scientific. Gold Shield ethanol (200 proof) was purchased from Rossville. For quantum dot syntheses, technical grade 1-octadecene, 99-100% myristic acid (n-$C_{13}H_{27}CO2H$) and 99% selenium dioxide were purchased from Sigma Aldrich. Cadmium myristate was synthesized as reported elsewhere[33] by precipitation from a methanolic solution of cadmium nitrate and myristic acid upon addition of sodium hydroxide. All other reagents used in quantum dot syntheses were technical grade and used without further purification.

5.2.2 Synthesis of CdSe quantum dots: The CdSe QDs were synthesized as reported elsewhere by Chen et al.[33] Briefly, to a 100 mL three-neck round bottom flask, 1 mmol (~0.57 g) cadmium myristate, 1 mmol (0.11 g) selenium dioxide, and 40 mL of 1-octadecene was added. The mixture was stirred at room temperature while purging with argon for ten minutes, then heated slowly (over 10 minutes) to ~110 °C, where it was kept, while purging with argon, until all precursors were soluble and the solution reached a transparent yellowish color. After precursor solubilization, the reaction temperature was heated rapidly to 220 °C, where it was

held for 1-10 minutes depending on the desired optical properties (i.e. particle size), followed by rapid cooling under compressed air flow to ~80°C when it was quenched by addition of 10-15 mL of n-butanol. The mixture transferred to a 500 mL beaker and then flocculated by adding 200-300 mL acetone. The CdSe QD pellet was isolated by centrifugation (3 min. at 7000 rpm) redissolved into ~20 mL of toluene then flocculated again with 100 mL of acetone. The QDs were further purified by repeating this procedure once more and were then stored in the dark in 20 mL of hexanes until further use.

5.2.3 Synthesis of potassium 1,1-dithiooxalate (DTO): The synthesis of 1,1-dithiooxalate as the potassium salt was adapted from a combination of the synthesis of 1,1-dithiobenzoic acid reported by Kuzer and Lawson[34] and the synthesis of potassium 1,1-dithiooxalate reported by Stork and Mattes.[35] Potassium hydroxide (2.50 g, 40.1 mmol) was dissolved in 20 mL of deoxygenated ethanol under argon flow. Half of the KOH solution was removed via syringe and H_2S was bubbled through the remaining 10 mL. The H_2S was generated in a separate flask by slowly dripping 6 M H_2SO_4 (ca. 10 mL) via dropping funnel onto 17.0 g of $Na_2S•9H_2O$ (70 mmol) with constant flow of argon. (*Caution: H_2S is very toxic as well as noxious and must not be released into the atmosphere*.) Excess H_2S was collected using a bubbler charged with a saturated $FeCl_3$ solution. (see figure 5.1) The H_2S generator was removed and the remaining KOH solution was added. After purging with argon for 30 min, the K_2S solution was heated to ca. 40 °C and 1.09 g of 1,1,1-trichloracetic acid (6.68 mmol) in 10 mL of ethanol was slowly added via dropping funnel while maintaining the temperature below 65 °C. The reaction solution was heated at gentle reflux for 30 min, then vacuum filtered following cooling to room temperature. The resulting yellow solid was rinsed with 3 x 30 mL of absolute ethanol and dried in vacuo to give a mixture of K_2 (DTO) and KCl with

carbon analysis indicating that the crude product was only about 40% of the former. The K_2(DTO)/KCl mixture was determined by ^{13}C-NMR (D_2O) to contain only the two carbons characteristic of the DTO anion. ^{13}C-NMR (D_2O): δ = 259, 181 ppm. The salt mixture was enriched in K_2(DTO) by slowly adding 3 equivalents of methanol to a saturated aqueous solution, filtering the precipitated KCl and removing the solvent from the filtrate. Two successive precipitations increased the K_2(DTO) content to 75%. The K_2(DTO) enriched salt mixture was recrystallized from 1:1 v/v MeOH/water, giving a highest attained purity of 97%. UV-Vis (pH 12 KOH solution): λ_{max} (ε in $M^{-1}cm^{-1}$) = 335 nm (15.0±0.1 x 10^3), 215 nm (~10^3). FTIR (KBr pellet): ν = 1583(vs), 1374(vs), 1020(vs), 772(s), 754(vs) cm^{-1}. The electronic absorption spectrum of K_2(DTO) was pH dependent, with significant loss in intensity of the 335 nm band with decreasing pH starting at pH 4. A pH titration curve indicates a pKa of ca.1.5 for 1,1-dithiooxalic acid.

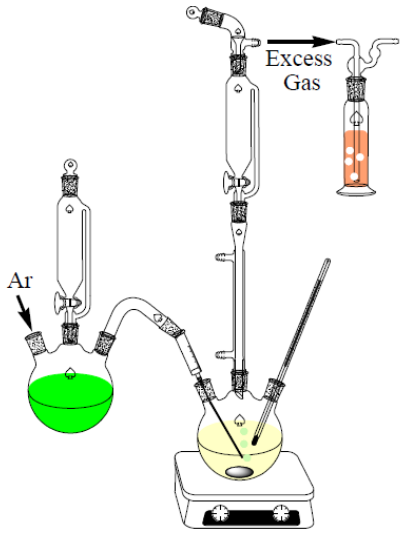

Figure 5.1: *Schematic of the apparatus used to for the synthesis of DTO. The leftmost flask was used for the generation of the toxic H2S gas. The excess H2S is trapped at the outlet of the apparatus by the FeCl3.*

5.1.4 Synthesis of O-t-butyl-1,1-dithiooxalate (tBuDTO): Following a reported method,[36,37] sulfur (1.92 g, 60.0 mmol) and 12.5 mL of triethylamine (90.0 mmol) were dissolved in 30 mL of deoxygenated dimethylformamide (DMF). After 50 min. 4.52 g of O-t-butyl-2-chloroacetate (30.0 mmol) was added in one portion, with vigorous stirring. The temperature of the reaction was kept between 20 and 30 °C using a water bath for 2 h. The reaction was filtered through a medium porosity frit filter to separate the $[NHEt_3]Cl$ that had precipitated from the reaction flask. The solids were then rinsed twice with 5 mL of DMF. The filtrate was added to 11.7 g of benzyltriphenylphosphonium chloride ($[BzPh_3P]Cl$, 30.0 mmol) dissolved in 30 mL of MeOH and crude $[BzPh_3P][tBuDTO]$ precipitated upon slow addition of 80 mL of water (ca. 50 min). After filtration, the plug of dark orange solid was washed by stirring in 200 mL of diethyl ether to remove excess DMF and water, filtered and the $[BzPh_3P][tBuDTO]$ salt was recrystallized twice from CH_2Cl_2/i-PrOH to give dark orange crystals that are readily dissolved in CH_2Cl_2 and $CHCl_3$, somewhat soluble in MeOH, EtOH and in mixed solvents (e.g. 1:2 CH_2Cl_2/EtOH). ^{1}H-NMR (CD_2Cl_2): δ = 6.98-7.82 (20H, m, Ar), 4.89 (2H, d, $^2J_{P\text{-}H}$ = 14.2), 1.41 (9H, s) ppm ^{13}C-NMR (CD_2Cl_2): ™ = 246.3 (CS_2), 170.4 (CO_2), 127-136 (multi. C_{Ar}), 117.6 (PCH_2-Ph, $^1J_{CP}$ = 88 Hz), 80.1 (C_{tBu}), 28.1 (Me_{tBu}) ppm. UV-Vis (MeOH): λ_{max} = 343 (14,600 $M^{-1}cm^{-1}$), 267 nm (4,280 $M^{-1}cm^{-1}$).

5.1.5 CdSe DTO ligand exchange: A pellet (~50 mg) of the CdSe QDs was extracted from the hexanes solution by flocculation via methanol and acetone and then dried under reduced pressure. The pellet was combined (in a 30 mL vial covered with aluminum foil) with 10 mL of DTO solution (~30 mM) in a water-methanol mixture (1:21 water to methanol) and stirred 10-12 h in the dark resulting in a reddish/orange precipitate. The precipitate was isolated by centrifugation (4 min at 4000 rpm), washed with ~5 mL chloroform (to remove

excess myristic acid), recollected via centrifugation, and suspended in ~10-15 mL of 50 mM sodium borate buffer (pH 9). Next, the solution was purified by washing twice with 15 mL DI water in 10,000 MWCO Millipore centrifugal filters. The final concentrated suspension was redissolved in 50 mM odium borate buffer because of the higher solubility in basic solution.

5.1.6 CdSe tBuDTO ligand exchange: A ~50 mg pellet of QDs was extracted from hexanes solution by flocculation via methanol and acetone and then dried under reduced pressure. The pellet was combined (in a 30 mL vial covered with aluminum foil) with 10 mL of an ~100 mM solution of *tBuDTO* in a chloroform and stirred 10-12 hours in the dark. Next, the chloroform was removed under reduced pressure resulting in a reddish-orange "cotton-candy" looking solid, which was suspended in methanol to wash away excess *tBuDTO* and centrifuged to collect the reddish QD pellet. The pellet was washed once more with methanol and then stored in chloroform. Spectral changes suggested the *tBuDTO* functionalized QDs were slightly soluble in methanol therefore some material was lost during the purification steps.

5.3 Characterization of QD-DTO Conjugates

Absorption spectra were recorded with a Shimadzu dual beam UV 2401 PC spectrophotometer. Spectra of the QDs prior to DTO ligand exchange were taken in toluene. Spectra recorded after DTO ligand exchange were taken with conjugates in pH 9 sodium 50 mM borate buffer solution and those after tBuDTO ligand exchange in chloroform. The spectra of solutions of DTO-QD conjugates were monitored with a Shimadzu UV-2401PC UV-Vis recording spectrophotometer under "dark conditions" with constant stirring. Absorbance values were stable under room temperature in pH 6 water and in pH 9 sodium borate buffer. Analogous stability was observed at 37 °C in pH 9 buffer.

Ligand exchange was evidenced by the solubility shift from organic to aqueous media as dianionic DTO replaced the hydrophobic myristate. Purified conjugates show a very strong UV absorption band (~335 nm) nearly the same as free DTO (λ_{max} ~335 nm, (λ_{max} = 1.5 x 10^4 M^{-1} cm^{-1} in aq. solution) and a QD exciton band red shifted by ~40 nm (figure 5.2, appendix D1). Similar red shifts in exciton absorptions have been seen when dithiocarbamates were exchanged onto semiconductor QD surfaces, and this effect was attributed to relaxation of exciton confinement in the QD-ligand conjugate owing to alignment of interfacial orbital energies.[38] Lastly, the strong QD PL was completely quenched. Aqueous solutions of the DTO-QD conjugates are stable in the dark for at least 6 h at 37 °C (figure 5.3) and indefinitely stable when stored in a refrigerator.

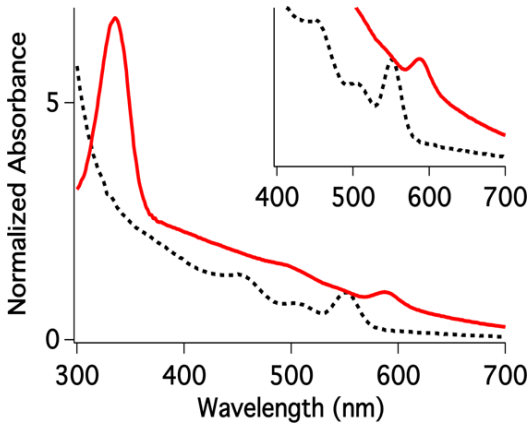

Figure 5.2: *Absorption spectrum of purified DTO-QD550 conjugates in pH 9 buffer (50 mM sodium borate) solution (solid line) and that of QD550 nanoparticles in toluene prior to ligand exchange (dashed line). Inset: Expanded view of the exciton peak shift. (QD subscript refers to exciton λ_{max} before ligand exchange, rounded to the nearest 10 nm)*

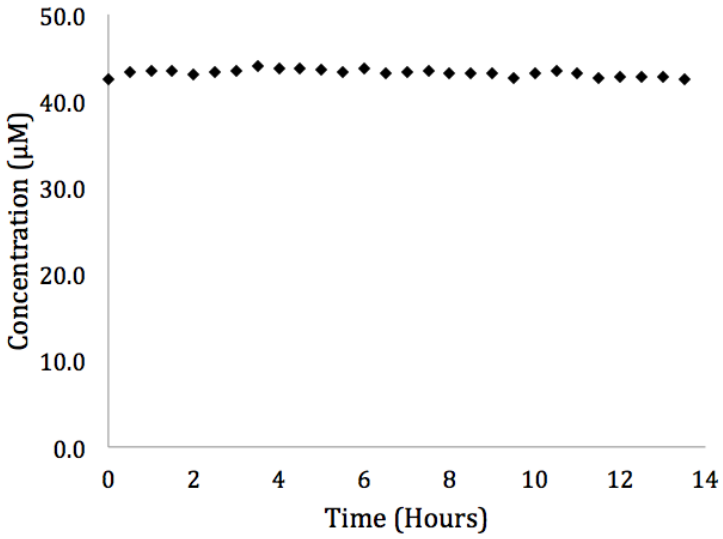

Figure 5.3: *Thermal stability in solution experiment: Concentration of DTO-QD_{551} conjugates in 50 mM sodium borate buffer (pH 9) at room temperature, kept in the dark over the course of 14 hours at 30 min intervals. Concentration is calculated from the absorption band at 335 nm using the technique described below in the quantum yield calculations section. Note that there is no significant change over this time period.*

5.4 Photolysis of Dithiooxalates at the Quantum Dot Surface

PL quenching in thiolate terminated QDs has been attributed to hole transfer from the conduction band to the surface bound ligands.[39] Such a mechanism, suggested that CdSe QDs could mediate DTO cleavage (equation 5.1).

$$S_2C\text{-}CO_2^{2-} \xrightarrow[\text{oxidant}]{h\nu,\ QD} CS_2 + CO_2 \qquad \textbf{(5.1)}$$

5.4.1 Continuous Wave Photolysis: Spectral changes during photolysis were measured using a Shimadzu UV-2401PC UV-Vis recording spectrophotometer and Photon Technology International (PTI) fluorimeter equipped with a 814 PMT detector. Quantitative photolysis was performed on an optical train that used lenses to focus the excitation beam into an area less than 1 cm^2. The UV light source was a high-pressure mercury arc lamp filtered for 365 nm using an band-pass filter and all other excitation wavelengths were performed using LUXEON® Star LEDs. The radiant power of the excitation source was measured using Molectron Detector Inc. Powermax 500A Laser Power Meter with a PM 10V1 volume absorbing probe. For UV light, the excitation power was also measured using ferrioxalate actinometry.

***5.4.2 Quantum yield calculations*:** Quantum yields for the photo-oxidation were based upon the calculated conversion of moles of 1,1-DTO per Einstein of absorbed light (equation 5.2).

$$\phi\ percent = \frac{\Delta\ DTO}{excitation\ photons\ absorbed} \cdot 100\% \qquad \textbf{(5.2)}$$

The quantum yields were calculated from photolysis periods with linear changes in quantity of ligand. The conversion DTO was based upon spectroscopic measurement of the peak centered at 335 nm. Solubility changes and the overlap of the ligand λ_{max} with the quantum dot absorbance confound a straightforward assignment of ligand concentration. To mitigate these a mathematical approximation was used to calculate the contribution of the ligand to the total absorbance. This approximation involved creating a line using the local absorbance minimum on the blue shifted side of the ligand peak and the absorbance at 400 nm. The difference between the absorbance of the ligand and the interpolated absorbance on this line at λ_{max} was used to calculate the ligand contribution to the total absorbance (figure 5.4).

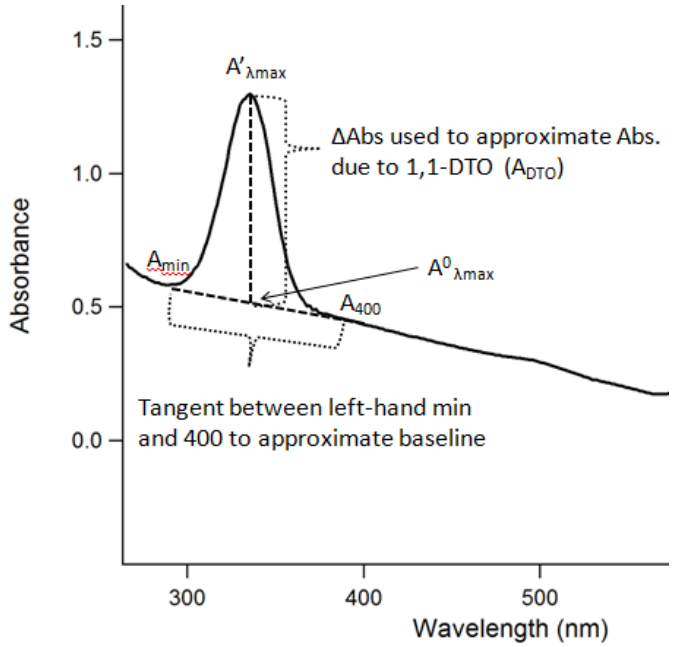

Figure 5.4: *Scheme used to calculate the concentration of DTO in solutions containing QDs.*

The ligand absorbance was then used to calculate the concentration and summarily the number of moles of ligand in the solution. This makes the approximation that binding to the surface doesn't change the ε_{335} of 1,1-DTO. (equations 5.3, 5.4, and 5.5)

$$mol\ DTO = [DTO]V \quad \textbf{(5.3)}$$

$$[DTO] = \frac{A_{DTO}}{\varepsilon_{\lambda max} l} \quad \textbf{(5.4)}$$

$$A_{DTO} = \lambda_{max}\left(\frac{A_{min}-A_{400}}{\lambda_{min}-\lambda_{m400}}\right) + \left[A_{400} - \lambda_{400}\left(\frac{A_{min}-A_{400}}{\lambda_{min}-\lambda_{m400}}\right)\right] \quad \textbf{(5.5)}$$

Visible light excitation was approximated to be mono-chromatic with a wavelength equal to the measured wavelength of maximum emission for the given LED (see figure 5.5).

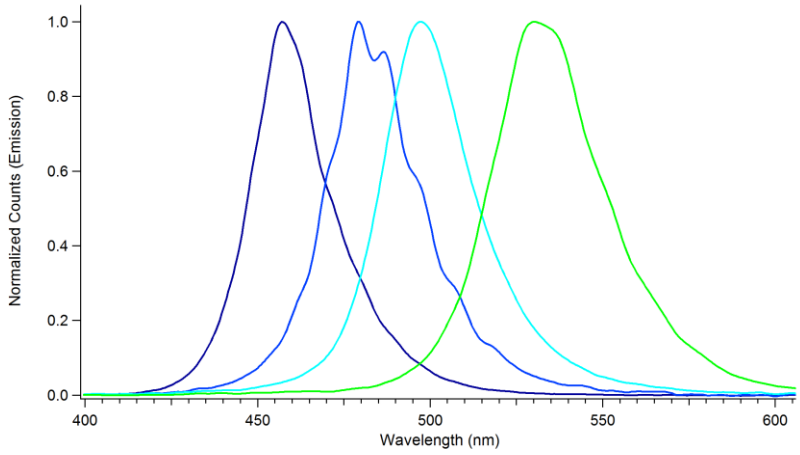

Figure 5.5: *Normalized emission spectra of LED's used in photolysis experiments. From left to right: Royal Blue (λ_{max}= 457), Blue (λ_{max}= 479), Cyan (λ_{max} = 498) and Green (λ_{max} = 530).*

The number of absorbed photons (I_A) was calculated using the irradiation time (t_{irr}), the measured radiant flux (P_0), and the sample absorbance at the excitation wavelength (A_{exc}). The approximation was made that the absorbance would not change during the course of irradiation. By overestimating the number of photons absorbed this approximation tends to underestimate quantum yield. (equations 5.6, 5.7 and 5.8)

$$I_A = P_A \cdot t_{irr} \qquad \textbf{(5.6)}$$

$$P_A = P_0 - P_T \qquad \textbf{(5.7)}$$

$$P_T = \frac{P_0}{10^{A_{exc}}} \qquad \textbf{(5.8)}$$

5.4.3 Photolysis of DTO-QD: Aerated, pH 9 aq. solutions of the purified DTO-QD550 conjugate were irradiated with 365 nm light. In this case, a systematic decrease in the 335 nm absorption band was observed which indicated that the surface-coordinated DTO was undergoing photodecomposition. The quantum yield for disappearance of this band (ϕ_{dis}) was 0.029 ± 0.008. Notably, this absorbance decrease was accompanied by recovery of the QD photoluminescence (figure 5.6). At higher photochemical conversion, the QD cores precipitated, owing to loss of the water-solvating surface ligands. Photolysis (365 nm) of a comparable solution of DTO alone (~70 μM) showed minimal photo-induced bleaching (appendix D2) and a much smaller ϕ_{dis} (0.004 ± 0.001).

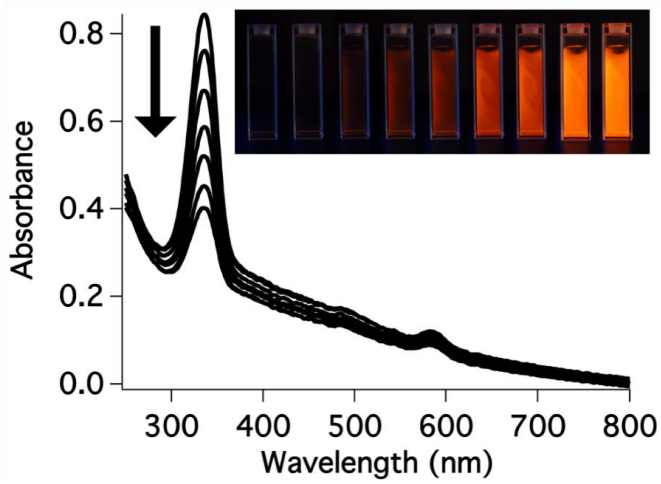

Figure 5.6: *Spectral changes for pH 9 solution of DTO-QD550 upon 365 nm excitation over the course of 120 s at 20 s intervals. Inset: Photograph showing photoluminescence return as photolysis proceeds.*

The difference between the DTO-QD conjugates and DTO itself is even more dramatic at longer irradiation wavelengths (λ_{irr}). When buffered solutions of DTO-QD550 were excited with light emitting diodes centered at 479, 498 or 530 nm (figure 5.5 above), bleaching of the 335 nm band occurred with comparable efficiency (ϕ_{dis} = 0.045 ± 0.005, 0.032 ± 0.003 and 0.039 ± 0.005 for these respective to that seen for λ_{irr} = 365 nm. Again, the photoluminescence of the QD cores was restored (appendix D3). In contrast, solutions of free DTO were unaffected owing to their optical transparency at these longer λ_{irr}, so there is little question that the QDs sensitize the photochemical decomposition of the surface bound DTO.

Similar sensitization of photodecomposition was observed with other DTO-QD conjugates although there were some differences in the quantum efficiencies. Respective ϕ_{dis} values of 0.016 ±0.003, 0.033 ±0.003 and 0.035 ±0.001 were measured for 498 nm irradiation

of DTO-QD510, DTO-QD550 and DTO-QD580 (figure 5.7); however, a larger data set would be needed before considering a possible systematic trend.

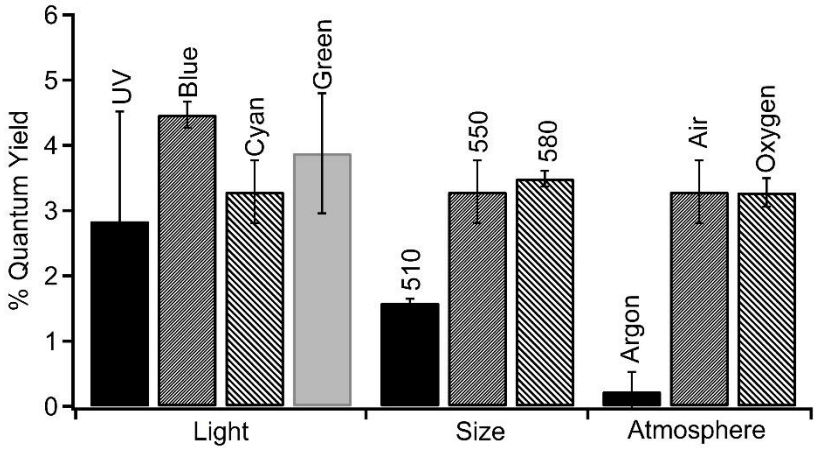

Figure 5.7: *Left: ϕ_{dis} values for the photolysis of DTO-QD550 conjugates at different λ_{irr} (UV = 365, Blue = 479, cyan = 498 and green = 530 nm). Center: ϕ_{dis} values for λ_{irr} 498 nm of DTO-QD510, DTO-QD550 and DTO-QD580. Right: ϕ_{dis} values for 498 nm photolysis of DTO-QD550 under Ar, air and O_2. All in pH 9 aq. solution.*

When the photoreactions were carried out under deaerated conditions, ϕ_{dis} values dropped precipitously. For example, 498 nm irradiation of DTO-QD550 solutions deaerated by extensive bubbling with argon gave $\phi_{dis} = 0.002 \pm 0.001$. However, an atmosphere of pure O_2 did not increase photoactivity ($\phi_{dis} = 0.033 \pm 0.001$) significantly above that seen in aerobic media. Thus, while the oxidant O_2 appears necessary for efficient net photodecomposition of coordinated DTO, this does not appear to be rate-limiting under normal conditions.

If these spectral changes do indeed reflect DTO photodecomposition, then other ligands in solution should coordinate to the resulting open surface sites. Thus, the QDs should be photocatalysts for oxidative decomposition of free DTO in solution. This reactivity was

demonstrated using an aerated pH 9 solution of DTO-QD550 to which a 2-fold excess of the K^+ salt of DTO (115 μM) had been added. Photolysis at 498 nm led to rapid decrease in the characteristic DTO absorbance at 335 nm (appendix D4), and a ϕ_{dis} = 0.052 ±0.006 was measured. Furthermore, the QDs remained in solution and showed little photoluminescence until the DTO was nearly consumed according to λ_{max} 335 nm. Thus, the system is indeed photocatalytic. Additionally, this confirms that the decomposition of DTO frees the QD surface from dithiolate coordination and suggests a strategy for syntheses of new quantum dot conjugates via incorporation of other ligands.

5.5 Analysis of DTO-QD Photoproducts

Although it has been speculated[36,37] that photooxidative decomposition of DTO would occur according to equation 5.1, CS_2 has not previously been detected as a photoproduct. To address this issue, we exhaustively photolyzed ($\lambda_{irr} \geq 479$ nm) aerated pH 9 solutions of DTO-QD550 in sealed, septa-capped vials. GC-MS analysis of headspace gases by Weck Laboratories (City of Industry, CA) showed that photolyzed samples gave dramatically larger amounts of CS_2 than the "dark" controls thereby confirming, qualitatively, formation of CS_2 as a photoproduct.

To our knowledge, CS_2 had not previously been directly detected as a photoproduct. To address this issue, we prepared aerated solutions (pH 9) of the DTO-QD550 conjugate in sealed, septa-capped vials that were exhaustively photolyzed at $\lambda_{irr} \geq 479$ nm or not irradiated (the "dark" controls). These were taken to the Weck Laboratories (City of Industry, CA) for analysis of headspace gas samples by GC-MS techniques. While the "dark" control displayed some CS_2 (a likely result of ambient light exposure during handling), all photolyzed samples

displayed dramatically larger quantities, confirming qualitatively formation of CS_2 as a photoproduct.

5.5.1 Detection of CS_2: Analytical procedures for determining CS_2 in solution are limited.[40] For this reason, A. W. DeMartino developed a quantitative method for this experiment based on the rapid reaction of CS_2 with amines[41] to form dithiocarbamates which have distinctive optical spectra with a strong absorption band in the ultraviolet.[42] During photolysis, the very volatile product CS_2 is swept from the solution by a stream of medical grade air into a cell containing methanol (3 mL) and n-octylamine (100µL). The resulting N-(n-octyl)dithiocarbamate displays a strong absorption band with a λ_{max} at 290 nm (e_{max} = $4.1x10^3$ M^{-1} cm^{-1}). The system was calibrated by injecting known quantities of CS_2 into the photolysis cell and determining the relative response. This procedure clearly confirms the formation of labile carbon disulfide as a photoproduct, although the amount of free CS_2 detected proved to be systematically about half that predicted if equation 5.1 were the only photoreaction represented by the photobleaching of the DTO peak at 335 nm. For example, 479 nm photolysis of a 3 mL pH 9 solution of DTO-QD550 for 15 min led to a decrease in the characteristic band at 335 nm corresponding to the photodecomposition of 260 nanomoles of DTO. However, only 130 nmol were transferred to the amine solution. Nonetheless, there is little question that very substantial quantities of CS_2 are produced by these photochemical events.

5.5.2 Quantitative Detection of CO_2: Much of the CO_2 generated in the pH 9 photolysis systems is likely to be trapped as a carbonate or bicarbonate. In this context, the CO_2 produced was determined before and after acidifying the photoproduct solution to ~pH 1 by analyzing the head space using a gas chromatograph equipped with a porous layer open tubular column

and a thermal conductivity detector. Consistent with the result found in the case of spectroscopic analysis for CS_2, the amount of CO_2 in the headspace generated by the photolysis was about half that predicted by equation 5.1 for the analysis before acidification and about 70% after acidification. For example, 479 nm photolysis of a 1 mL aqueous solution of DTO-QD_{550} containing 2 mM DTO in a sealed vial produced 0.951 mM CO_2 in the headspace before acidification, and 1.38 mM CO_2 in the headspace after acidification.

5.6 Mechanistic Speculations

The gaseous products and the requirement for O_2 as a co-reactant suggest that photolysis of surface coordinated DTO reversibly leads to transient species that are trapped by the external oxidant (scheme 5.1). Alternatively, it might be argued that photo-induced 2-electron transfer from DTO to the QD occurs either simultaneously or sequentially, and that the “charged” QDs are no longer photoactive until "discharged" by reacting with O_2 (scheme 5.2). The formation of the DTO radicals suggested by scheme 1 offers a possible explanation for the non-stoichiometric formation of CS_2 and CO_2, given that such species might dimerize to give a disulfide link-age. Regardless of the actual mechanism, the catalytic behavior shows that the QD sensitized photooxidation and cleavage of DTO facilitates removal and re-placement of the surface ligands. Future studies could attempt to differentiate the mechanistic possibilities.

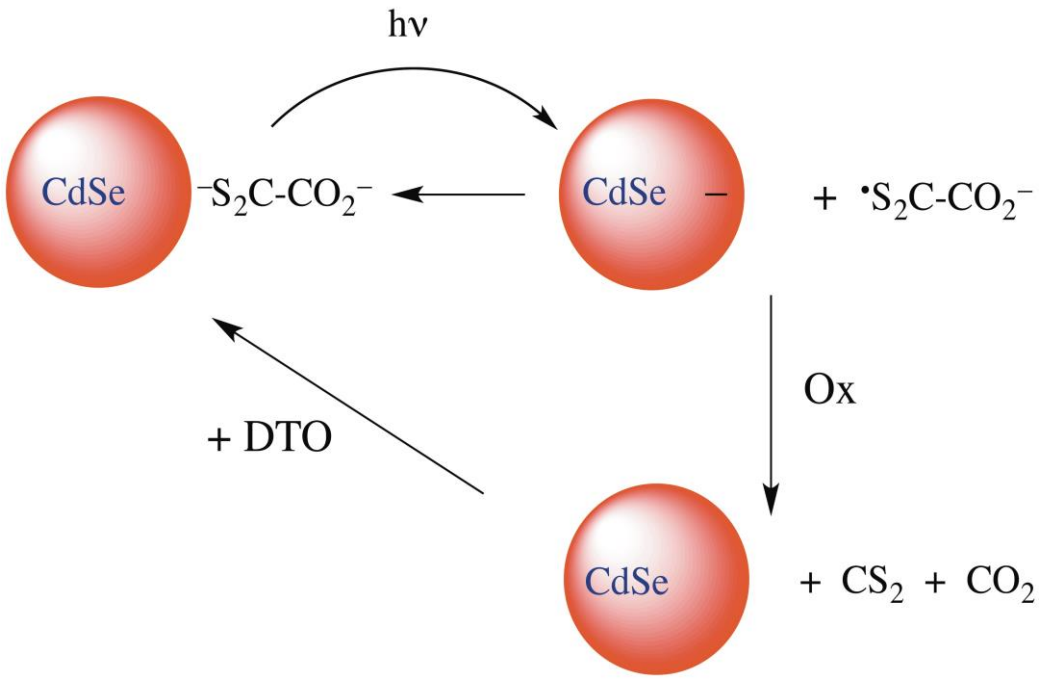

Scheme 5.1: *Possible photocatalysis involving an external oxidant.*

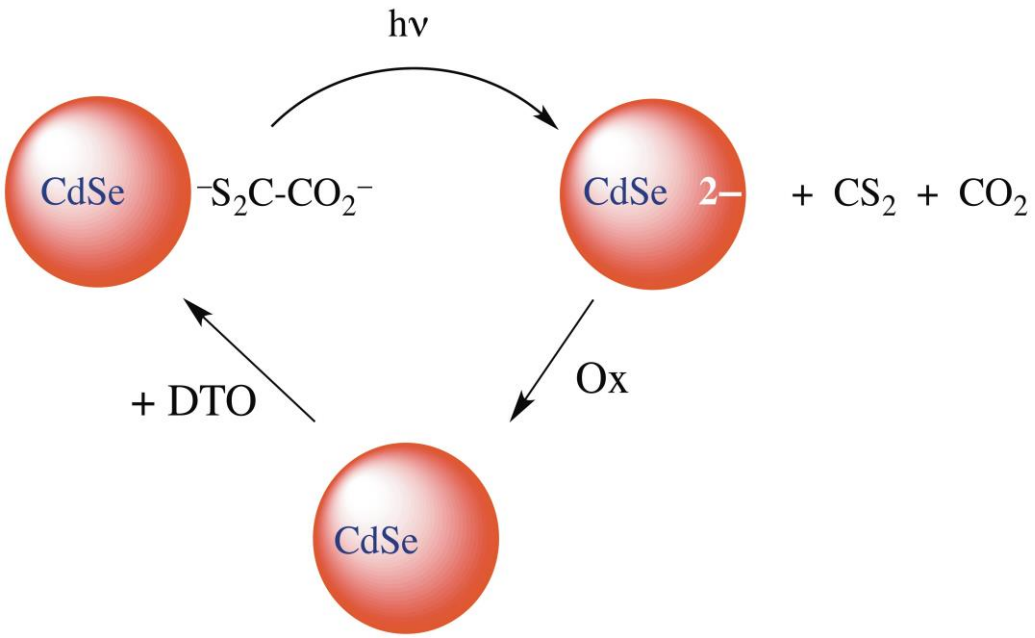

Scheme 5.2: *Photocatalysis occurring via quantum dot charging.*

5.7 Photocatalysis of tBuDTO-QD Conjugates

While DTO functionalization provides aqueous solubility, QD conjugates of tBuDTO remain soluble in organic media. Given that CO_2 formation must contribute to the driving force for equation 5.1, analogous oxidative activation of an O-ester such as tBuDTO may release a radical, as in equation 5.9.

$$S_2C\text{-}CO_2R^- \xrightarrow[\text{oxidant}]{h\nu,\ QD} CS_2 + CO_2 + R^{\bullet} \qquad \textbf{(5.9)}$$

Organic soluble conjugates were prepared as described in section 5.2 by exchanging tBuDTO for the myristate surface ligands of QD510. The spectrum of tBuDTO-QD510 displayed the strong absorption band at 350 nm characteristic of the DTO chromophore and an exciton peak at 523 nm red shifted from that of the core QD exciton peak. In addition, the conjugate was not luminescent, as seen for the QD conjugates with DTO. Photolysis of tBuDTO-QD510 with λ_{irr} 498 nm in aerated solution led to bleaching of the 350 nm DTO band but ϕ_{disr} values were small, 0.007 in toluene and 0.0024 in chloroform. Exhaustive photolysis led to photoluminescence recovery and a shift of the exciton peak to its original maximum (figure 5.8), while the QDs remained soluble. The analytical method described above demonstrated that CS_2 is clearly formed during this photoreaction but the yields are even lower (~12 %) than with analogous DTO conjugates.

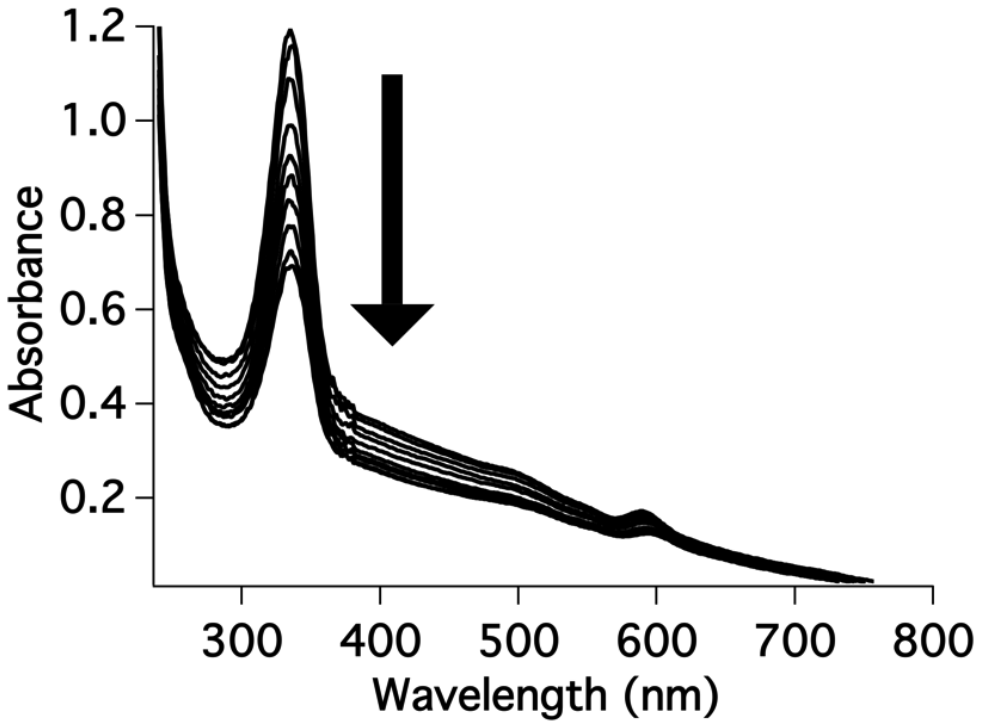

Figure 5.8: *Absorption spectra depicting the spectral changes under de-aerated conditions of QD_{551}-DTO conjugates over the course of 60 minutes of irradiation with a focused 10 mW LED centered at 498 nm. After 60 minutes, enough DTO remained to still quench the QD photoluminescence completely. The overall decrease in absorption was due to the gradual precipitation of QDs in the absence of DTO surface ligands. The quantum yield for DTO decomposition under deaerated conditions was calculated to be 0.4 percent.*

5.8 Summary of Photocatalyzed CS_2 Uncaging from DTO-QD Conjugates

In summary, photosensitive conjugates were prepared by displacing the native surface ligands on CdSe QDs with 1,1-dithiooxalate and with O-t-butyl-dithiooxalate. The resulting DTO-QD conjugates are water-soluble while the R-DTO conjugates are organic-soluble. For both the QD exciton bands are shifted to the red and photoluminescence is quenched.

Photolysis in aerated solutions leads to the photo-catalytic oxidative decomposition of these surface ligands with modest quantum yields. By using a colorimetric assay, it was shown in both cases that CS_2 is generated; this represents the first demonstrated photochemical release of this potentially therapeutic small molecule.

We propose that the photo-oxidation mechanism involves QD excitation-induced hole transfer to surface bound DTO. The efficiency is highly dependent upon the presence of another oxidant, O_2, which serves as the ultimate electron acceptor. The reaction not only decomposes the multiple DTOs bound to the QD surface, but the facile ligand exchange leads to a catalytic cycle for photo-oxidation of excess DTO free in solution. In addition, this offers a potential pathway for the systematic removal or replacement of QD surface ligands and syntheses of new QD-ligand conjugates through the use of light.

O-ester-DTO-QD conjugates undergo analogous photodecomposition. We propose that such a photocleavable ligand may allow the controlled release of organic radicals from QD surfaces. Future studies could be directed towards a better quantification of the products as well as expanding the photochemistry to a library of other esters in order to probe the utility of these as photo-cleavable surface anchors.

5.9 References for Photochemical Carbon Disulfide Production

1. L. C. Choi, A. P. Alivisatos, "From Artificial Atoms to Nanocrystal Molecules: Preparation and Properties of More Complex Nanostructures" *Annu. Rev. Phys. Chem.* **2010**, *61*, 369

2. I. L. Medintz, H. T. Uyeda, E. R. Goldman, H. Mattoussi "Quantum dot bioconjugates for imaging, labelling and sensing" *Nature Mat.* **2005**, *4*, 435.

3. A. C. S. Samia, X. Chen, C. Burda, "Semiconductor Quantum Dots for Photodynamic Therapy"*J. Am. Chem. Soc.* **2003**, *125*, 15736.

4. P. T. Burks, P. C. Ford, "Quantum dot photosensitizers. Interactions with transition metal centers" *Dalton Trans.* **2012**, *41*, 13030.

5. S. J. Sortino, "Photoactivated nanomaterials for biomedical release applications" *Mater. Chem.* **2012**, *22*, 301.

6. I. N. Robel, V. Subramanian, M. Kuno, P. V. Kamat, "Quantum dot solar cells. Harvesting light energy with CdSe nanocrystals molecularly linked to mesoscopic TiO_2 films" *J. Am. Chem. Soc.* **2006**, *128*, 2385.

7. T. P. A. Ruberu, C. N. Nelson, I. I. Slowing, J. J. Vela, "Selective Alcohol Dehydrogenation and Hydrogenolysis with Semiconductor-Metal Photocatalysts: Toward Solar-to-Chemical Energy Conversion of Biomass-Relevant Substrates" *Phys. Chem. Lett.* **2012**, *3*, 2798.

8. J. Zhao, M. A. Holmes, F. E. Osterloh, "Quantum Confinement Controls Photocatalysis: A Free Energy Analysis for Photocatalytic Proton Reduction at CdSe Nanocrystals" *ACS Nano* **2013**, *7*, 4316.

9. D. A. Wink, J. B. Mitchell, "NO and cancer" *Free Radical Biol. Med.* **2003**, *34*, 951-954.

10. D.A. Wink, Y. Vodovotz, J. Laval, F. Laval, M. W. Dewhirst, J. B. Mitchell, "The multifaceted roles of nitric oxide in cancer" *Carcinogenesis* **1998**, *19*, 711-721.

11. L. J. Ignarro, In ***Nitric Oxide: Biology and Pathobiology*** Academic Press: San Diego, **2000**.

12. L. Wu, R. Wang, "Carbon Monoxide: Endogenous Production, Physiological Functions, and Pharmacological Applications" *Pharmacol. Rev.* **2005**, *57*, 585-630.

13. R. Motterlini, "The therapeutic potential of carbon monoxide" *Nat. Rev. Drug. Discov.* **2010**, *9*, 728-743.

14. B. Mann, In ***Medicinal Organometallic Chemistry***; Jaouen, G. r., Metzler-Nolte, N., Eds.; Springer Berlin Heidelberg: **2010**; Vol. *32*, 247-285.

15. G. Yang, L. Wu, B. Jiang, W. Yang, J. Qi, K. Cao, Q. Meng, A. K. Mustafa, W. Mu, S. Zhang, S. H. Snyder, R. Wang, "H_2S as a Physiologic Vasorelaxant: Hypertension in Mice with Deletion of Cystathionine γ-Lyase" *Science* **2008**, *322*, 587-590.

16. C. Szabo "Hydrogen sulphide and its therapeutic potential" *Nat. Rev. Drug. Discov.* **2007**, *6*, 917-935.

17. R. Wang "Two's company, three's a crowd: can H_2S be the third endogenous gaseous transmitter?" *The FASEB Journal* **2002**, *16*, 1792-1798.

18. W. Zhao, J. Zhang, Y. Lu, R. Wang, "The vasorelaxant effect of H_2S as a novel endogenous gaseous KATP channel opener" *EMBO J* **2001**, *20*, 6008-6016.

19. K. K. Pandey, "Reactivities of carbonyl sulfide (COS), carbon disulfide (CS2) and carbon dioxide (CO2) With Transition Metal Complexes" *Coordination Chemistry Reviews* **1995**, *140*, 37-114.

20. R. O. Beauchamp, J. S. Bus, J. A. Popp, C. J. Boreiko, L. Goldberg, M J. McKenna, "A Critical Review of the Literature on Carbon Disulfide Toxicity" *Crc. Cr. Rev. Toxicol.* **1983**, *11*, 169-278.

21. W. M. Valentine, V. Amarnath, D. G. Graham, D. C. Anthony "Covalent cross-linking of proteins by carbon disulfide" *Chem. Res. Toxicol.* **1992**, *5*, 254-262.

22. R. Shreck, B. Meier, D. N. Mannel, W. Droge, P. A. Baeuerle "Dithiocarbamates as potent inhibitors of nuclear factor kappa B activation in intact cells" *J. Exp. Med.* **1992**, *175*, 1181-1194.

23. T. D. Gilmore, M. Herscovitch "Inhibitors of NF-[kappa]B signaling: 785 and counting" *Oncogene* **2006**, *25*, 6887-6899.

24. T. D.Gilmore "Introduction to NF-[kappa]B: players, pathways, perspectives" *Oncogene* **2006**, *25*, 6680-6684.

25. S. Caroldi, J. A. E. Jarvis, L. Magos, "Stimulation of dopamine-β-Hydroxylase in rat adrenals by repeated exposures to carbon disulfide" *Biochemical Pharmacology* **1984,** *33*, 1933-1936.

26. S Caroldi, J. A. E. Jarvis, L. Magos, "In vivo inhibition of dopamine-β-hydroxylase in rat adrenals during exposure to carbon disulfide" *Arch. Toxicol.* **1984,** *55*, 265-267.

27. I. Ali, W. A. Wani, K. Saleem, M. Hseih, "Design and synthesis of thalidomide based dithiocarbamate Cu(II), Ni(II), and Ru(III) complexes as anticancer agents" *Polyhedron* **2013,** *56,* 134–143.

28. S. D. Munger, T. Leinders-Zufall, L. M. McDougall, R. E. Cockerham, A. Schmid, P. Wandernoth, G. Wennemuth, M. Biel, F. Zufall, K R. Kelliher, "An olfactory subsystem that detects carbon disulfide and mediates food-related social learning" *Curr. Biol.* **2010,** *20,* 1438–1444.

29. R. W. Wood, "Neurobehavioral toxicity of carbon disulfide" *Neurobehav. Toxico.l Teratol.* **1981**, *3*, 397-405.

30. X. Tan, X. Peng, F. Wang, M. Joyeux, P. Hartemann, "Cardiovascular effects of carbon disulfide: meta-analysis of cohort studies" *Int. J. Hyg. Environ. Health* **2002,** *205*, 473-477

31. H. Huang, Y. Zhou, J. Ma, N. Wang, Z. Zhang, D. Ding, G. Chen, "Nitric oxide mediated effects on reproductive toxicity caused by carbon disulfide in male rats" *Environmental Toxicology and Pharmacology* **2012**, *34*, 679–687

32. M. Phillips, M. Sabas, J. Greenberg, "Increase pentane and carbon disulfide in breath of patients with schizophrenia" *J. Clin. Pathol.* **1993**, *46,* 861-864

33. O. Chen, X. Chen, Y. Yang, J. Lynch, H. Wu, J. Zhuang, Y. C. Cao, Y. C. "Synthesis of metal selenide nanocrystals using selenium dioxide as the selenium precursor" *Angew. Chem., Int. Ed.* **2008**, *47,* 8638-8641

34. F. Kurzer, A. Lawson "Thiobenzoylthioglycolic acid" *Org. Synth.* **1962**, *42*, 100-101

35. W. Stork, R. Mattes, "Alkali metal salts of monothio-, 1,1-dithio- and 1,1,2 trithiooxalic acid" *Angew. Chem., Int. Ed. Engl.* **1975**, *14*, 436-437

36. D. F. Zigler, E. Tordin, E. G. Wu, A. Iretskii, E. Cariati, P. C. Ford "Mononuclear copper (I) complexes of O-t-butyl-1,1-dithiooxalate and of O-t-butyl-perthio-1oxalate" *Inorganica Chimica Acta*, **2011**, *374,* 261-268

37. P. Strauch, B. Dempe, R. Kempe, W. Dietzsch, J. Sieler, J. E. Hoyer, "1,1-Dithiooxalsäurederivate als Liganden in Übergangmetallkomplexen: Struktur von OMethyl-1,1-dithiooxalato-bis(triphenylphosphin)kupfer(I) und –silber(I)" *Z. Anorg. Allg. Chem.* **1994**, *620*, 498-504

38. M. T. Frederick, V. A. Amin, E. A. Weiss "The optical properties of Strongly Coupled Quantum Dot-Ligand Systems" *J. Phys. Chem. Lett*. **2013**, *4,* 634

39. S. F. Wuister, C. de Mello Donego, A. J. Meijerink “Influence of thiol capping on the exciton luminescence and decay kinetics of CdTe and CdSe quantum dots” *Phys. Chem. B* **2004**, *108*, 17393-17397

40. W. K. Rogers, K. M. Wilson, C. E. "Methods for detecting disulfiram in biologic fluids: application in studies of compliance and effect of divalent cations on bioavailability" *Alcohol. Clin. Exp. Res.* **1978**, *2*, 375-380.

41. F. E. Critchfield, F. E. J. B. Johonson, "Reaction of carbon disulfide with primary and secondary aliphatic amines as analytical tool" *Anal. Chem.* **1956**, *28*, 430-436.

42. A. W. DeMartino “Carbon sisulfide: a potential small molecule bioregulator” Dissertation for University of California Santa Barbara, **2017**.

Appendix A – Supplemental Information for Chapter II

A1: Table of chemicals purchased for model compound studies including CAS number, and abbreviations used in the text.

CAS Number	Chemical Name	Abbreviation
100-39-4	m-cresol	
100-44-5	p-cresol	
100-51-6	benzyl alcohol	
100-66-3	anisole	
101-84-8	diphenyl ether	DPE
103-73-1	ethoxybenzene	
108-87-2	methylcyclohexane	
108-88-3	toluene	
108-93-0	cyclohexanol	
108-94-1	cyclohexanone	
108-95-2	phenol	
110-82-7	cyclohexane	
120-80-9	catechol	
124-18-5	decane	
1330-20-7	xylene *mixed isomers*	
576-26-1	2,6-xylenol	
583-59-5	2-methylcyclohexanol *cis-trans mixture*	
589-91-3	4-methylcyclohexanol *cis-trans mixture*	
591-23-1	3-methylcyclohexanol *cis-trans mixture*	
90-05-1	guaiacol	
91-16-7	veratrole	
946-80-5	benzyl phenyl ether	BPE
95-48-7	o-cresol	

A2: Workshet for the Synthesis Potassium 2-phenoxy-1-phenylethan-1-ol

Recipe for ~100 mmol of starting materials with bromoacetophenone as the limiting reagent. Worksheet by Chris Bernt, adapted from methods by J. M. Nichols et. Al.

Equipment to gather and clean before experiment

500 mL Round Bottom Flask	Reflux Condenser	Oil Bath
Hot Plate Stirrer	Stir Bar	Filter Flask
Buchner Funnel	Filter Paper	500 mL Filter Flask
500 mL Beaker	Ice Bucket	Separatory Funnel

Chemicals Needed

Phenol (108-95-2)	2-Bromoacetophenone (70-11-1)
Potassium Carbonate	Sodium Borohydride
Ethanol	Acetone
Tetrahydorfuran (THF)	Ether
Brine Solution (sat. NaCl)	

Part 1: Synthesis of 2-phenoxy-1-phenylethan-1-one

1.) Add 17.5 g potassium carbonate and a stir bar to a 1000 mL round bottom flask.

2.) Add 200 mL of acetone to the flask and swirl to mix (note, the K_2CO_3 won't completely dissolve).

3.) Add 19.5 g of 2-bromoacetophenone to the flask and stir until dissolved.

4.) Add 10 g (9.4 mL in liquid form) of phenol

5.) Attach reflux condenser and place in an oil bath. Heat to gentle reflux (B.P. ~ 56 °C) and reflux overnight.

6.) Set up a filter flask with Buchner funnel and filter paper. Filter yellow solution from reflux and discard solid.

7.) Evaporate acetone from filtered solution to collect a yellow solid. (*Note: The easiest method is to use the house vacuum and the collection flask itself; just leave the vacuum open and allow the solvent to evaporate. A rotary evaporator is probably more appropriate to properly collect and dispose of waste liquid*)

8.) To improve the product purity, dissolve the solid in a minimal amount of warm ethanol. (*Can be done in whatever vessel was used to remove the acetone*).

10.) Place in ice bath to form crystals (easier if solution is transferred to a beaker first).

11.) Filter crystals to collect a pale yellow solid and wash solid with ice cold ethanol to remove impurities. *To improve yields the liquids can be collected, reduced, and chilled again to obtain more crystals*. The resultant solid is the analogous ketone, 2-phenoxy-1-phenylethan-1-one

Part 2: Synthesis of 2-phenoxy-1-phenylethan-1-one

Reduction (for 30 mmol of ketone)

12.) Dissolve 6.37g (30 mmol) of the 2-phenoxy-1-phenylethan-1-one in 136 mL of THF.

13.) Add 34 mL of water for a final solution of 4:1 THF/H2O.

14.) Add 2.3g of sodium borohydride to this mixture portion wise then stir at room temp for 3 hours.

15.) While it is reducing prepare 200 mL each of saturated solutions of Ammonium Chloride and Sodium Chloride

_____g NH_4Cl
_____g NaCl

16.) After 3 hours quench reaction with ammonium chloride solution
17.) Pour Solution into large beaker and dilute with 200 mL of water
18.) Extract with 3 times with 200 ml of Ether. *Note, the ether layer will be on top so you'll need to save the aqueous layer in a beaker, collect the ether layer in a separate beaker, and pour the aqueous layer back into the sep. funnel for each extraction.*
19.) Wash the combined ether fractions twice with 100 ml of brine
20.) Dried the ether layer over $MgSO_4$ (add magnesium sulfate until it no longer clumps in the ether)
21.) Filter the ether solution to remove the drying agent.
22.) Evaporate the ether to collect the final product (see step 7 for options).
Can be recrystallized in ethanol to increase purity.

References
J. M. Nichols, L. M. Bishop, R. G. Bergman, J. A. Ellman, "Catalytic Bond Cleavage of 2-Aryloxy-1-arylethanols and Its Application to the Depolymerization of Lignin-Related Polymers" *J. Am. Chem. Soc.* 2010, *132*, 12554-12555.

A3: Workshet for the synthesis of copper doped porous metal oxide catalyst

Protocol for the Synthesis of copper doped porous metal oxide with a 3:1 Mg^{2+} to Al^{3+} mol ratio with 20% of the Mg^{2+} replaced by Cu^{2+} (Cu20PMO)

Molar ratio:
0.023 moles magnesium nitrate hexahydrate
0.007 moles copper nitrate trihydrate
0.01 moles aluminum nitrate nonahydrate

Mass of metal salts used:
$Mg(NO_3)_2 \cdot 6H_2O$: 6.15 g
$Al(NO_3)_3 \cdot 9H_2O$: 3.75 g
$Cu(NO_3)_2 \cdot 3H_2O$: 1.45 g

Steps for Preparation:
Dissolve 3.75 g of aluminum nitrate in 25 mL of water.
Dissolve 6.15 g of the magnesium nitrate and 1.45 g of copper nitrate in another 25 mL of water
Combine both solutions to form a 50 mL solution containing all three metal compounds
Dissolve about 1.06 g of sodium carbonate (Na_2CO_3) in 75 mL of deionized water in a 600 mL beaker
Prepare a 1 Molar NaOH solution. (16 g of NaOH in 400 mL of water)
Place the beaker containing the sodium carbonate solution on a hot plate.
Clamp a thermometer in the beaker to monitor the temperature.
Place a stir bar in the beaker and stir vigorously
The beaker should be heated to between 60-65°C.
Add the 50 mL solution containing the Mg, Al, and Cu drop by drop to the carbonate solution while heating and stirring.
Monitor the pH and keep it at 10 using the 1 molar NaOH solutions. Alternating aliquots of the metal solution and NaOH solution should be added drop by drop to the carbonate solution to keep the pH at 10.
Once the entire 50 mL solution containing the metals has been added cover the beaker and leave it stirring for a minimum of 4 more hours and cover the beaker using parafilm.
Leave the catalyst aging overnight between 60-65° C.

Steps for Washing:
Remove the catalyst from the heat
Filter the catalyst using a clean frit filter
Prepare a wash bath for the catalyst containing 1.00 g Na_2CO_3 in 500 mL in 500 mL of deionized water in an 800 mL beaker.
Add the filtered catalyst to the wash bath.
Stir the catalyst in the wash bath vigorously for a minimum of 2 hours (more time is better!!!!)
After the catalyst has been washed filter it again using a clean frit filter (clean the frit filter with acid bath for about 5 min)
When only a thin layer of water remains on top of the catalyst in the filter add deionized water to the catalyst to rinse it. Rinse it two times consecutive times.
Steps for Drying:
After the catalyst has been washed and rinsed place it in a crucible.
Place the crucible in the oven at 110°C for a minimum of 4 hours.
After the catalyst is dried remove a small sample to be analyzed
Place the catalyst back in the oven at 460° C for a minimum of 4 hours to be calcined.
After the catalyst is calcined remove it from the oven and place it in the desiccator to cool.
Grind the sample using a mortar and pestal.

A4: Theoretical ECN for calculations in GC/FID experiments.

Compound	Relative r.f.	ECN	aliphatic carbons	aromatic carbons	olefinic carbon	carbonyl carbon	ether oxygen	1°-OH oxygen	2°-OH oxygen
***Decane (Standard)**	**1.00**	**10.00**	**10**	**0**	**0**	**0**	**0**	**0**	**0**
1-phenyl-1,2 ethanediol	1.48	6.75	2	6	0	0	0	1	1
1-phenyl-1-propanone	1.25	8.00	2	6	0	1	0	0	0
2-phenoxy-1-phenylethan-1-ol	0.82	12.25	2	12	0	0	1	0	1
acetophenone	1.43	7.00	1	6	0	1	0	0	0
anisole	1.67	6.00	1	6	0	0	1	0	0
benzaldehyde	1.67	6.00	0	6	0	1	0	0	0
benzylphenyl ether	0.83	12.00	1	12	0	0	1	0	0
benzyl alcohol	1.54	6.50	1	6	0	0	0	1	0
cresol	1.54	6.50	1	6	0	0	0	1	0
cyclohexane	1.67	6.00	6	0	0	0	0	0	0
cyclohexanediol	2.22	4.50	6	0	0	0	0	0	2
cyclohexanol	1.90	5.25	6	0	0	0	0	0	1
cyclohexanone	2.00	5.00	5	0	0	1	0	0	0
cyclohexene	1.69	5.90	4	0	2	0	0	0	0
cyclohexylmethanol	1.54	6.50	7	0	0	0	0	1	0
cyclopentylmethanol	1.82	5.50	6	0	0	0	0	1	0
dimethylbenzene	1.25	8.00	2	6	0	0	0	0	0
dimethylcyclohexane	1.25	8.00	8	0	0	0	0	0	0
dimethylcyclohexanediol	1.54	6.50	8	0	0	0	0	0	2
dimethylcyclohexanol	1.38	7.25	2	6	0	0	0	0	1
dimethylcyclohexanone	1.43	7.00	2	5	0	1	0	0	0
dimethylphenol	1.38	7.25	2	6	0	0	0	0	1
diphenyl ether	0.91	11.00	0	12	0	0	1	0	0
ethoxybenzene	1.43	7.00	2	6	0	0	1	0	0
ethoxycyclohexane	1.43	7.00	8	0	0	0	1	0	0
guaiacol	1.90	5.25	1	6	0	0	1	0	1
methoxycyclohexane	1.67	6.00	7	0	0	0	1	0	0
methoxycyclohexanone	2.00	5.00	6	0	0	1	1	0	0
methoxymethyl-benzene	1.43	7.00	6	2	0	0	1	0	0
methylanisole	1.67	6.00	1	6	0	0	1	0	0
methylcyclohexane	1.43	7.00	7	0	0	0	0	0	0
methylcyclohexanediol	1.82	5.50	7	0	0	0	0	0	2
methylcyclohexanol	1.60	6.25	7	0	0	0	0	0	1
methylcyclohexanone	1.67	6.00	6	0	0	1	0	0	0
methylcyclohexene	1.45	6.90	5	0	2	0	0	0	0
methylmethoxybenzene	1.43	7.00	2	6	0	0	1	0	0

Compound	Relative r.f.	ECN	aliphatic carbons	aromatic carbons	olefinic carbon	carbonyl carbon	ether oxygen	1° -OH oxygen	2° -OH oxygen
methylmethoxycyclohexane	1.43	7.00	8	0	0	0	1	0	0
methylmethoxycyclohexanone	1.67	6.00	7	0	0	1	1	0	0
methoxyethylbenzene	1.25	8.00	3	6	0	0	1	0	0
phenol	1.90	5.25	0	6	0	0	0	0	1
phenylethanol	1.60	6.25	1	6	0	0	0	0	1
propylbenzene	1.11	9.00	3	6	0	0	0	0	0
toluene	1.43	7.00	1	6	0	0	0	0	0
trimethyl benzene	1.21	8.25	3	6	0	0	0	0	1
veratrol	1.67	6.00	2	6	0	0	2	0	0
unknown monomer	1.69	5.93	0.6	6	0	0	0	0	0.9
unknown dimer	0.79	12.70	1	12	0	0	0.3	0	0

Appendix B – Supplemental Information for Chapter III

B1: Analysis of product mixtures from the reaction of phenol

Analysis of product mixtures from the reaction of phenol over the copper-doped porous metal oxide catalyst. (310 °C, 3 mL MeOH, 100 mg Cu20PMO, 20 μL decane, 1 mmol substrate). *B1.1:* Reaction scheme showing calculated rate constants (k_{obs} in hr^{-1}) for conversion to specific products ($R^2 > 0.86$). *B1.2:* Temporal evolution of the product mixture reported in percent of starting substrate and calculated from FID response of the GC-MS-FID and calibrated against decane as an internal standard (see chapter 2). Material balance: 82% at 3 h, 78% at 6 h, and 73% at 24 h.

B1.1

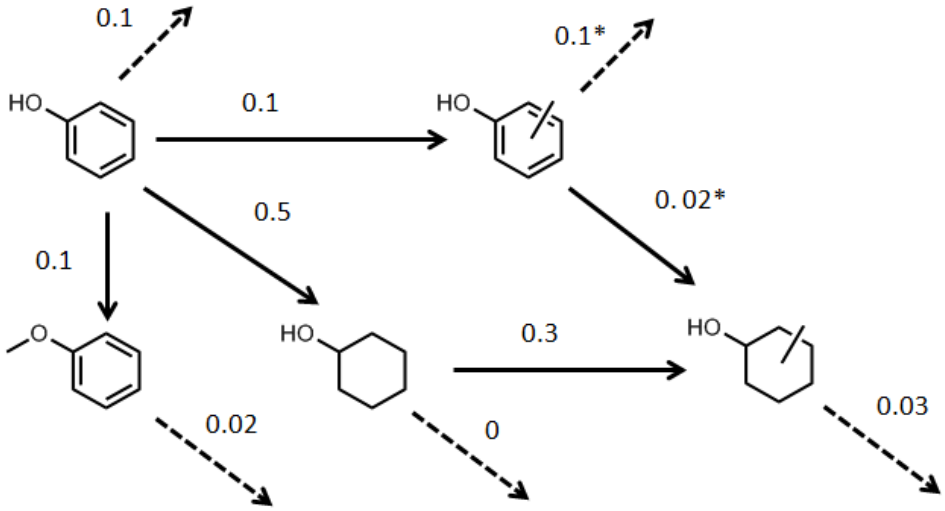

B1.2

Compound	1h	2h	3h	6h	9h	12h	18h
anisole	7.8	9.2	8.5	10.0	10.2	9.3	7.4
benzene	0.1	0.3	0.2	0.6	0.7	1.2	1.7
cresol	13.7	9.8	6.7	3.3	1.2	0.2	0.0
cyclohexane	0.0	0.2	0.3	0.6	0.7	1.0	1.1
cyclohexanol	18.4	29.4	28.3	13.7	9.0	6.3	2.8
cyclohexanone	0.9	1.1	1.1	0.4	0.3	0.3	0.0
dimethylbenzene	0.0	0.0	0.0	0.1	0.1	0.1	0.1
dimethylcyclohexane	0.0	0.0	0.0	0.2	0.4	0.7	1.5
dimethylcyclohexanol	0.5	1.7	2.8	5.4	7.4	11.1	12.1
dimethylphenol	2.0	2.7	2.8	3.6	3.2	2.0	0.8
methoxycyclohexane	0.1	0.4	0.5	0.7	0.9	1.8	3.0
methylanisol	0.8	1.4	1.7	2.4	2.8	2.9	2.6
methylcyclohexane	0.0	0.1	0.3	0.4	0.8	1.8	3.8
methylcyclohexanol	9.0	19.4	24.5	34.0	36.4	39.0	32.2
methylcyclohexanone	0.6	0.8	1.1	1.2	1.2	1.2	0.9
methylmethoxycyclohexane	0.0	0.1	0.2	0.3	0.5	1.5	3.8
methylmethoxycyclohexanone	0.1	0.3	0.3	0.5	0.6	0.5	0.6
phenol	45.8	7.9	3.0	0.4	0.0	0.0	0.0
toluene	0.0	0.1	0.1	0.3	0.3	0.5	0.6

B2: Analysis of product mixtures from the control reaction of phenol

B2: Analysis of product mixtures from the reaction of phenol over the un-doped porous metal oxide catalyst. (310 °C, 3 mL MeOH, 100 mg PMO, 20 μL decane, 1 mmol substrate). Product mixture reported in percent of starting substrate and calculated from FID response of the GC-FID and calibrated against decane as an internal standard (see above analysis section). Material balance: 86% at 18 h.

Compound	0 h	18 h
anisole	0	11.6
cresol	0	1.9
phenol	100	67.7

B3: Analysis of product mixtures from the reaction of cresol

Analysis of product mixtures from the reaction of cresol (methyl phenol) over the copper-doped porous metal oxide catalyst. (310 °C, 3 mL MeOH, 100 mg Cu20PMO, 20 μL decane, 1 mmol substrate) Temporal evolution of the product mixture reported in percent of starting substrate and calculated from FID response of the GC-MS-FID and calibrated against decane as an internal standard (see chapter 2). Material balance 93% at 4 h.

Compound	0	0.75	1	1.5	2	2.25	3	4
cresol	100.0	80.7	67.8	67.9	57.1	51.6	46.4	48.9
dimethylcyclohexanol	0.0	0.0	0.0	0.0	0.3	0.0	0.5	0.3
dimethylphenol	0.0	14.6	19.3	21.3	24.4	35.3	37.5	33.0
methylcyclohexanol	0.0	0.8	1.6	1.5	4.9	1.8	4.3	5.6
methylcyclohexanone	0.0	0.1	0.2	0.1	0.3	0.1	0.3	0.3
methylmethoxybenzene	0.0	0.9	1.5	1.8	3.4	3.6	4.4	4.7
trimethylbenzene	0.0	0.0	0.0	0.0	0.4	0.0	0.4	0.3

B4: Analysis of product mixtures from the reaction of guaiacol

Analysis of product mixtures from the reaction of guaiacol (2-methoxyphenol) over the copper-doped porous metal oxide catalyst. (310 °C, 3 mL MeOH, 100 mg Cu20PMO, 20 µL decane, 1 mmol substrate) *B4.1:* Reaction scheme showing calculated rate constants (k_{obs} in hr^{-1}) for conversion to specific products. ($R^2 > 0.89$) *B4.2:* Temporal evolution of the product mixture reported in percent of starting substrate and calculated from FID response of the GC-MS-FID and calibrated against decane as an internal standard (see chapter 2). Material balance >99% at 3 h, 83% at 6 h, 62% at 24 h.

B4.1

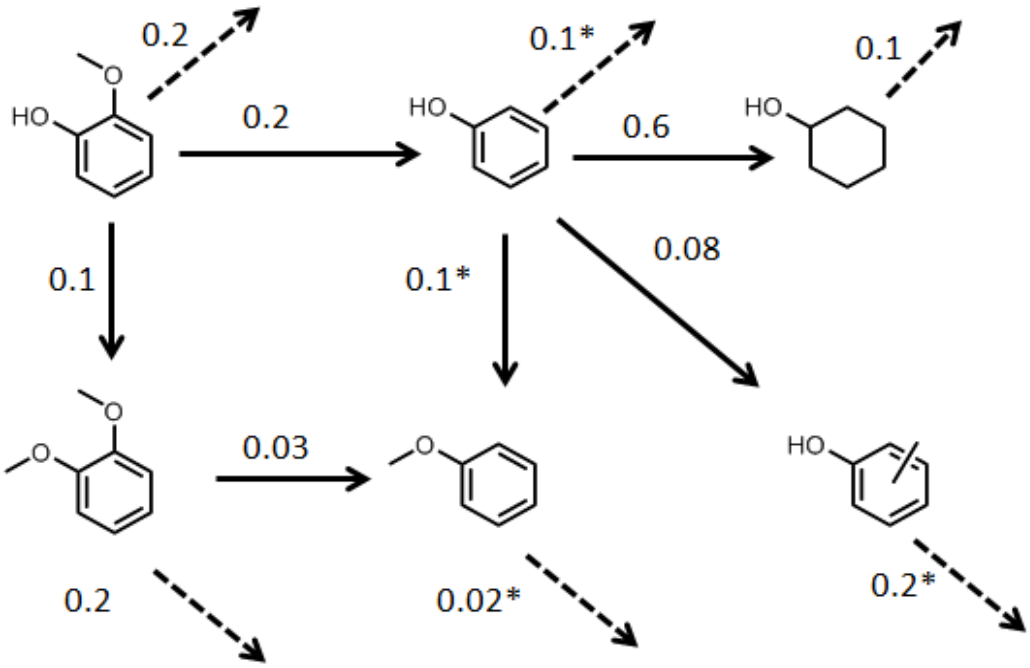

B4.2

Compound	1h	2h	3h	6h	9h	12h	18h	24h
anisole	0.0	0.5	2.2	4.4	5.8	6.7	7.7	4.7
benzene	0.0	0.0	0.0	0.2	0.4	0.7	2.0	0.5
cresol	1.2	1.5	3.7	1.7	0.1	0.0	0.0	0.0
cyclohexandiol	0.0	7.9	10.6	0.0	0.0	0.0	0.0	0.0
cyclohexane	0.0	0.1	1.0	3.4	3.0	3.7	4.2	3.3
cyclohexanol	0.0	3.0	14.9	18.8	10.2	8.3	3.0	7.1
cyclohexanone	0.0	0.1	0.7	1.6	1.1	1.1	1.1	0.7
cyclopentylmethanol	0.0	3.0	13.8	15.0	11.3	14.0	10.7	10.1
dimethylcyclohexane	0.0	0.0	0.1	0.5	0.5	0.7	1.8	0.5
dimethylcyclohexanol	0.1	1.4	4.1	3.2	3.7	4.5	4.7	4.0
dimethylphenol	0.5	1.8	2.0	1.0	0.3	0.3	0.0	0.2
guaiacol	87.1	42.8	8.1	0.0	0.0	0.0	0.0	0.0
methoxycyclohexane	0.0	0.1	0.7	2.1	2.6	3.4	5.0	2.0
methoxycyclohexanone	0.0	1.0	3.1	3.0	2.0	2.7	2.0	1.6
methylanisole	2.4	4.2	4.9	0.7	0.0	0.0	0.0	0.0
methylcyclohexane	0.0	0.1	0.3	1.3	1.8	2.3	4.5	1.9
methylcyclohexanol	0.0	0.6	5.0	14.1	18.3	20.6	20.5	21.6
methylcyclohexanone	0.0	0.0	0.3	1.0	0.5	0.7	0.7	0.7
phenol	2.1	8.7	10.5	0.2	0.0	0.0	0.0	0.0
toluene	0.0	0.0	0.1	0.2	0.2	0.4	0.4	0.2
veratrol	6.6	11.5	17.7	11.2	4.8	4.0	0.7	3.3

B5: Analysis of product mixtures from the reaction of anisole

Analysis of product mixtures from the reaction of anisole over the copper-doped porous metal oxide catalyst. (310 °C, 3 mL MeOH, 100 mg Cu20PMO, 20 μL decane, 1 mmol substrate). Temporal evolution of the product mixture reported in percent of starting substrate and calculated from response area of the GC-MS and calibrated against decane as an internal standard (see chapter 2). The response factor for compounds marked with a star was approximated by compounds with the same atomic composition. Material balance >99% at 4 h, >99% at 6 h.

compound	0h	1h	2h	3h	4h	6h
anisole	100.0	98.8	94.2	94.9	95.0	82.4
benzene	0.0	0.5	3.0	6.8	5.7	17.1
cyclohexane	0.0	0.0	0.0	0.0	0.2	0.9
cyclohexanol	0.0	0.0	0.1	0.4	0.5	0.7
methoxycyclohexane*	0.0	0.0	0.2	0.6	0.3	2.0

B6: Analysis of product mixtures from the reaction of ethoxybenzene

Analysis of product mixtures from the reaction of ethoxybenzene over porous metal oxide catalyst. (310 °C, 3 mL MeOH, 0.100 g Cu20PMO, 20 μL decane, 1 mmol substrate). Temporal evolution of the product mixture reported in percent of starting substrate and calculated from FID response of the GC-MS-FID and calibrated against decane as an internal standard (see chapter 2). Material balance >99% at 6 h.

Compound	3h	6h
benzene	1.1	6.4
cyclohexanol	0.3	1.1
ethoxybenzene	98.4	88.0
ethoxycyclohexane	0.3	2.9
methylcyclohexanol	0.0	0.7

B7: Analysis of product mixtures from the reaction of veratrol

Analysis of product mixtures from the reaction of veratrol over the copper-doped porous metal oxide catalyst. (310 °C, 3 mL MeOH, 100 mg Cu20PMO, 20 μL decane, 1 mmol substrate) Temporal evolution of the product mixture reported in percent of starting substrate and calculated from FID response of the GC-MS-FID and calibrated against decane as an internal standard (see above analysis section). Material balance 98% at 3 h, 71% at 18 h.

Compound	1h	3h	12h	18h
anisole	10.7	39.7	45.2	27.3
benzene	0.1	2.1	12.5	18.1
cyclohexane	0.3	0.9	3.1	3.4
cyclohexanol	0.5	3.1	1.9	1.1
dimethylcyclohexanol	0.2	1.1	1.7	1.6
methoxycyclohexane	0.1	1.0	7.6	13.2
methylcyclohexane	0.0	0.3	1.2	2.2
methylcyclohexanol	0.4	2.6	4.7	3.8
toluene	0.0	0.1	0.4	0.7
veratrol	87.8	47.5	2.8	0.2

B8: Analysis of product mixtures from the reaction of benzyl phenyl ether

Analysis of product mixtures from the reaction of benzyl phenyl ether over the copper-doped porous metal oxide catalyst. (310 °C, 3 mL MeOH, 50 mg Cu20PMO, 20 μL decane, 1 mmol substrate). Temporal evolution of the product mixture reported in percent of starting substrate and calculated from response area of the GC-MS and calibrated against decane as an internal standard (see chapter 2). Note, since benzyl phenyl ether conversion results in two products the total percent of starting substrate at complete conversion would be 200% with total conservation. Therefore, the material balance was calculated by dividing the summed moles of products by twice the initial moles of benzyl phenyl ether. The calculated material balances are thus 88% at 4 h, 97% at 6 h, 82% at 18 h. Note that toluene is >90% of that expected even at 18 h while phenol and phenolic products are lower.

compound	0h	1h	2h	3h	4h	6h	8h	12h	18h
benzylphenyl ether	100	15	1	0	0	0	0	0	0
phenol	0	76	60	24	3	0	0	0	0
toluene	0	81	91	96	92	88	88	93	90
phenol derived aromatics	0	8	19	20	18	15	20	13	16
phenol derived alkanes	0	6	26	39	63	72	60	64	59
unassigned products	0	0	1	10	12	13	15	15	18

B9: Analysis of product mixtures from the control reaction of benzyl phenyl ether

Analysis of product mixtures from the reaction of benzyl phenyl ether over the un-doped porous metal oxide catalyst. (310 °C, 3 mL MeOH, 50 mg PMO, 20 μL decane, ca. 1 mmol substrate). Product mixture reported in percent of starting substrate and calculated from FID response of the GC-FID and calibrated against decane as an internal standard (see chapter 2). The "dimeric" products were products whose M.W. as indicated by GC-MS suggested two rings. The response factor for these were based on an ECN of 12.5. Material balance: 76% at 3 h, 58% at 18 h with the caveat noted above in B8.

compound	0h	1h	3h	6h	18h	24h
anisole	0	0	0.3	0.7	8.1	5.1
benzyl alcohol	0	0.5	1.1	1.8	4.6	2.9
benzyl phenyl ether	100	75.3	48.3	41	1.3	0.4
cresol	0	0.1	0.7	1.8	10.1	8.4
methylanisole	0	0.3	0.5	0.8	2.6	1
phenol	0	3	13.7	21.8	6.3	13.2
toluene	0	2.8	17.6	24.7	44.5	47.9
xylenol	0	0	0.1	0.3	4.6	2.8
dimeric products	0	1.9	11.6	16.6	16.7	20.1

B10: Analysis of product mixture from the reaction of 2-phenoxy-1-phenylethan-1-one

Analysis of product mixture from the reaction of 2-phenoxy-1-phenylethan-1-one over porous metal oxide catalyst (310 °C, 3 mL MeOH, 100 mg Cu20PMO, 20 μL decane, 1 mmol substrate). Product mixture reported in mol percent of products detected and calculated from FID response of the GC-MS-FID and calibrated against decane as an internal standard.

Compound	6h
benzene	0.5
cresol	3.5
cyclohexane	0.5
cyclohexanol	14.1
dimethylcyclohexanol	1.4
dimethylphenol	3.5
ethylbenzene	34.7
methoxycyclohexane	0.5
methylanisole	1.5
methylcyclohexane	0.4
methylcyclohexanol	19.9
methylcyclohexanone	0.7
propylbenzene	16.8
toluene	1.9

B11: Analysis of product mixtures from the reaction of cyclohexanol

Analysis of product mixtures from the reaction of cyclohexanol over the copper-doped porous metal oxide catalyst. (310 °C, 3 mL MeOH, 100 mg Cu20PMO, 20 µL decane, 1 mmol substrate). Temporal evolution of the product mixture reported in percent of starting substrate and calculated from response area of the GC-MS and calibrated against decane as an internal standard (see chapter 2). The response factor for compounds marked with a star was approximated by compounds with the same atomic composition. Material balance >99% at 3 h, >99% at 6 h.

compound	0	1	2	3	4.15	6
cyclohexane	0.0	0.2	0.7	0.9	1.6	2.1
cyclohexanol	100.0	88.0	66.3	73.9	47.9	39.8
methylcyclohexanol	0.0	13.8	28.3	30.9	48.0	58.3
other compounds*	0.0	0.6	1.8	2.2	4.0	5.2

B12: Comprehensive reaction network of mono-aromatics over the copper-doped porous metal oxide catalyst.

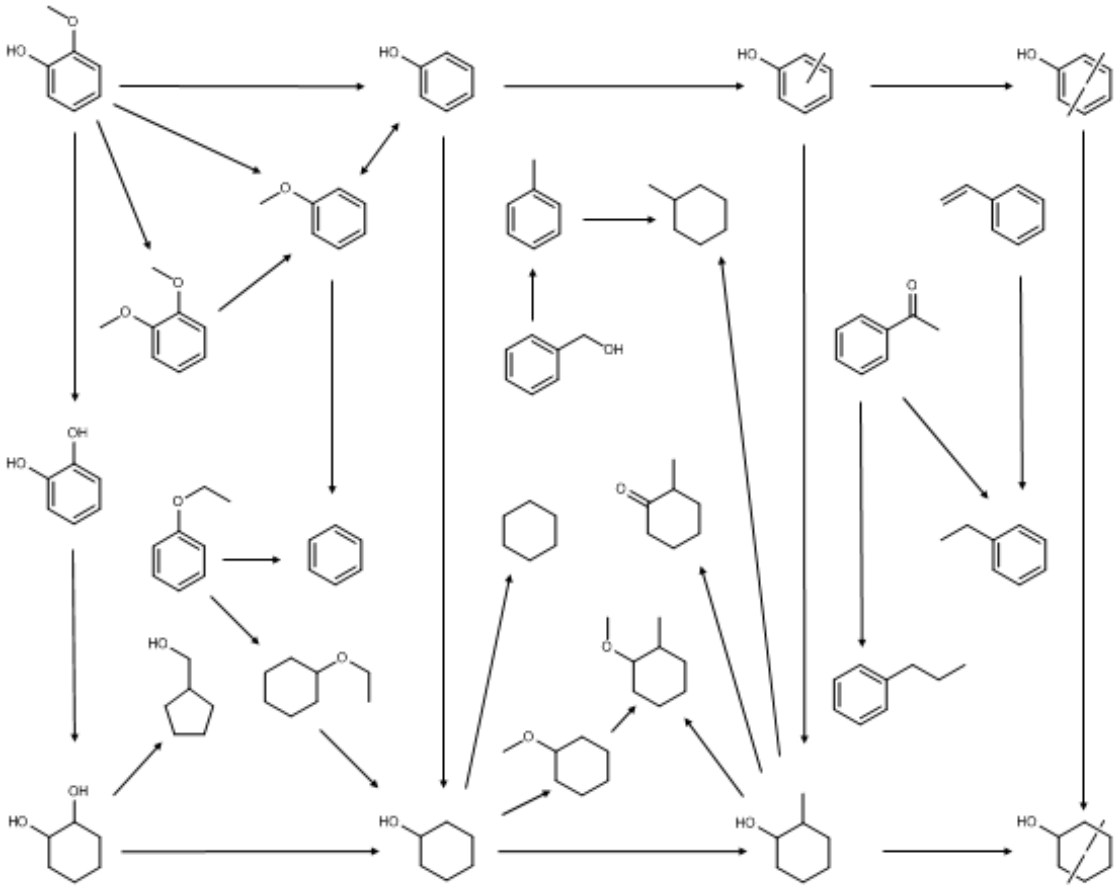

Appendix C – Supplemental Information for Chapter IV

C1: Analysis of product mixtures from the reaction of 2-phenoxy-1-phenylethan-1-ol

Analysis of product mixtures from the reaction of 2-phenoxy-1-phenylethan-1-ol (PPE) over the copper-doped porous metal oxide catalyst at 290-320 °C for shorter experimental runs (up to 90 min). Conditions: 3.0 mL MeOH, 50 mg Cu20PMO, 20 µL decane, ~1 mmol substrate. Temporal evolution of the product mixture is reported in µmol and calculated from response area of the GC-FID peaks and calibrated against decane as an internal standard. See chapter 2 for further details of the analytical methods.

2-phenoxy-1-phenylethan-1-ol, 50 mg Cu20PMO, 280 °C						
compound	**0 min**	**15 min**	**30 min**	**45 min**	**60 min**	**90 min**
1-phenylethanol	0	0	10	166	274	391
1-phenylpropanol	0	0	3	31	75	124
1-phenylpropanone	0	0	13	63	106	95
2-phenoxy-1-phenylethan-1-ol	1432	1414	1218	747	391	195
acetophenone	0	0	57	307	381	279
cresol	0	0	1	13	33	79
ethylbenzene	0	0	2	25	50	200
phenol	0	1	87	574	845	1138

2-phenoxy-1-phenylethan-1-ol, 50 mg Cu20PMO, 290 °C						
compound	**0 min**	**15 min**	**30 min**	**45 min**	**60 min**	**90 min**
1-phenylethanol	0	0	58	312	379	280
1-phenylpropanol	0	0	9	55	85	90
1-phenylpropanone	0	0	29	72	78	45
2-phenoxy-1-phenylethan-1-ol	1446	1462	1042	332	158	196
acetophenone	0	0	181	402	328	153
cresol	0	0	4	26	53	112
ethylbenzene	0	0	9	71	157	395
phenol	0	2	282	875	1051	1223

2-phenoxy-1-phenylethan-1-ol, 50 mg Cu20PMO, 300 °C						
compound	**0 min**	**15 min**	**30 min**	**45 min**	**60 min**	**90 min**
1-phenylethanol	0	0	204	390	312	181
1-phenylpropanol	0	0	8	32	47	50
1-phenylpropanone	0	0	15	35	54	32
2-phenoxy-1-phenylethan-1-ol	1468	1471	789	257	244	206
acetophenone	0	0	225	311	280	110
cresol	0	0	5	27	51	112
cyclohexanol	0	0	0	4	11	36
ethylbenzene	0	0	27	174	300	549
phenol	0	2	464	949	1071	1141
xylenol	0	0	2	4	6	9

2-phenoxy-1-phenylethan-1-ol, 50 mg Cu20PMO, 310 °C						
compound	**0 min**	**15 min**	**30 min**	**45 min**	**60 min**	**90 min**
1-phenylethanol	0	1	108	246	211	84
1-phenylpropanol	0	0	24	67	80	33
1-phenylpropanone	0	0	77	90	74	21
2-phenoxy-1-phenylethan-1-ol	1423	1489	658	234	85	16
acetophenone	0	1	354	332	214	58
cresol	0	0	18	58	100	166
cyclohexanol	0	0	1	7	17	53
ethylbenzene	0	0	35	175	307	538
methoxyethylbenzene	0	0	0	3	11	24
phenol	0	5	601	992	1101	1146
xylenol	0	0	112	175	173	60

2-phenoxy-1-phenylethan-1-ol, 50 mg Cu20PMO, 320 °C						
compound	**0 min**	**15 min**	**30 min**	**45 min**	**60 min**	**90 min**
1-phenylethanol	0	31	379	279	115	6
1-phenylpropanol	0	0	21	23	10	0
1-phenylpropanone	0	9	30	18	8	1
2-phenoxy-1-phenylethan-1-ol	1491	1255	216	26	11	7
acetophenone	0	63	396	171	65	8
cresol	0	1	28	73	108	129
cyclohexanol	0	0	4	24	49	87
ethylbenzene	0	3	166	499	689	778
methoxyethylbenzene	0	0	0	2	3	4
phenol	0	112	1002	1112	1047	664
xylenol	0	1	7	8	10	15

C2: Summary of rate constants (hr^{-1}) for the conversion of PPE

Summary of rate constants (hr^{-1}) for the conversion of PPE over the copper-doped porous metal oxide catalyst at 280-320 °C for shorter experimental runs (up to 90 min). Conditions: 3 mL MeOH, 50 mg Cu20PMO, 20 μL decane, 1 mmol substrate.

Temp (°C)	280	290	300	310	320	Ea
k_{HDG} (hr^{-1})	1.9 ± 0.3	2.3 ± 0.4	2.7 ± 0.3	3.5 ± 0.1	7.1 ± 0.13	83 ± 18

C3: Analysis of product mixtures from 6 h time course reactions of BPE

Analysis of product mixtures from the reaction of benzyl-phenyl ether (BPE) over the copper-doped porous metal oxide catalyst at 280-310 °C for up longer experimental runs (up to 360 min). Conditions: 3 mL MeOH, 50 mg Cu20PMO, 20 μL decane, 1 mmol substrate. Temporal evolution of the product mixture reported in μmol and calculated from response area of the GC-FID peaks and calibrated against decane as an internal standard. See chapter 2 for further details of the analytical methods.

benzylphenyl ether, 50 mg Cu20PMO, 280 °C							
compound	**0 min**	**60 min**	**120 min**	**180 min**	**240 min**	**300 min**	**360 min**
anisole	0	8	36	56	60	71	109
BPE	1055	182	11	0	0	0	0
cresol	0	29	92	118	121	123	138
cyclohexane	3	3	3	4	4	6	8
cyclohexanol	0	19	115	224	328	417	547
methylanisole	0	0	1	2	2	3	9
methylcyclohexanol	0	0	9	21	32	48	107
phenol	0	869	962	737	551	392	174
toluene	0	874	939	963	950	962	1075
xylenol	0	0	3	6	8	9	20

benzylphenyl ether, 50 mg Cu20PMO, 290 °C							
compound	**0 min**	**60 min**	**120 min**	**180 min**	**240 min**	**300 min**	**360 min**
anisole	0	19	68	53	117	102	71
BPE	1105	139	3	0	0	0	0
cresol	0	51	132	162	145	94	53
cylcohexanol	0	47	174	336	554	535	547
methylcylcohexanol	0	1	29	46	159	170	195
phenol	2	947	748	373	148	78	16
toluene	0	911	985	886	1033	1014	846
xylenol	0	0	9	64	27	18	15

benzylphenyl ether, 50 mg Cu20PMO, 300 °C						
compound	**0 min**	**60 min**	**180 min**	**240 min**	**300 min**	**360 min**
anisole	0	22	206	98	99	126
BPE	1213	110	5	2	0	0
cresol	0	68	204	123	120	88
cyclohexane	0	4	6	5	4	7
cyclohexanol	0	21	65	580	662	485
methylanisole	0	0	86	9	12	21
methylcyclohexanol	0	0	154	145	238	324
phenol	0	649	15	128	53	12
toluene	0	714	1291	990	794	969
xylenol	0	4	325	19	27	38

benzylphenyl ether, 50 mg Cu20PMO, 310 °C							
compound	**0 min**	**60 min**	**120 min**	**180 min**	**240 min**	**300 min**	**360 min**
anisole	0	42	60	80	84	93	91
BPE	1090	31	15	1	0	0	0
cresol	0	79	85	98	81	71	54
cyclohexane	0	2	4	6	5	5	6
cyclohexanol	0	137	322	461	499	557	510
methylanisole	0	1	3	5	6	9	9
methylcyclohexanol	0	14	58	92	148	204	239
phenol	0	826	522	279	175	57	39
toluene	0	916	961	1000	1012	1006	1040
xylenol	0	3	7	10	12	15	14

C4: Analysis of product mixtures from 2 h time course reactions of BPE

Analysis of product mixtures from the reaction of benzyl-phenyl ether (BPE) over the copper-doped porous metal oxide catalyst at 280-320 °C for shorter experimental runs (up to 120 min). Conditions: 3.0 mL MeOH, 50 mg Cu20PMO, 20 μL decane, 1 mmol substrate. Temporal evolution of the product mixture reported in reported in μmol and calculated from response area of the GC-FID peaks and calibrated against decane as an internal standard. See chapter 2 for further details of the analytical methods.

benzylphenyl ether, 50 mg Cu20PMO, 280 °C					
compound	**0 min**	**30 min**	**60 min**	**90 min**	**120 min**
BPE	942	721	735	410	40
cresol	0	9	33	46	91
cyclohexanol	0	1	4	15	76
phenol	0	211	295	324	549
toluene	0	280	334	522	930

benzylphenyl ether, 50 mg Cu20PMO, 290 °C					
compound	**0 min**	**30 min**	**60 min**	**90 min**	**120 min**
BPE	911	620	310	148	18
cresol	0	18	59	85	133
cyclohexanol	0	3	23	77	107
phenol	0	271	392	452	534
toluene	0	312	604	766	918

benzylphenyl ether, 50 mg Cu20PMO, 300 °C					
compound	**0 min**	**30 min**	**60 min**	**90 min**	**120 min**
BPE	983	601	261	60	3
cresol	0	30	79	120	163
cyclohexanol	0	8	35	81	173
phenol	0	395	504	498	455
toluene	0	370	655	821	860

benzylphenyl ether, 50 mg Cu20PMO, 310 °C					
compound	**0 min**	**30 min**	**60 min**	**90 min**	**120 min**
BPE	859	507	90	49	1
cresol	0	28	102	112	163
cyclohexanol	0	7	73	84	161
phenol	0	281	546	408	296
toluene	0	382	810	783	800

benzylphenyl ether, 50 mg Cu20PMO, 320 °C					
compound	**0 min**	**30 min**	**60 min**	**90 min**	**120 min**
BPE	899	327	24	0	0
cresol	0	56	132	133	127
cyclohexanol	0	27	122	185	214
phenol	0	491	527	231	150
toluene	0	600	861	868	796

C5: Summary of rate constants (hr^{-1}) for the conversion of BPE

Summary of rate constants (hr^{-1}) for the conversion of BPE over the copper-doped porous metal oxide catalyst at 280-320 °C for up to 120 min (3 mL MeOH, 50 mg Cu20PMO, 20 μL decane, 1 mmol substrate).

Temp (°C)	280	290	300	310	320	Ea
k_{HDG} (hr^{-1})	1.0 ± 0.2	1.5 ± 0.1	1.9 ± 0.1	2.5 ± 0.2	4.2 ± 0.1	91 ± 8.0

C6: Analysis of the product mixtures from the reactions of phenol

Analysis of product mixtures from the reaction of phenol over the copper-doped porous metal oxide catalyst at 290-320 °C for shorter experimental runs (up to 120 min). Conditions: 3.0 mL MeOH, 50 mg Cu20PMO, 20 μL decane, 1 mmol substrate. Temporal evolution of the product mixture reported in μmol and calculated from response area of the GC-FID peaks and calibrated against decane as an internal standard. See chapter 2 for further details of the analytical methods.

phenol, 50 mg Cu20PMO, 280 °C					
compound	**0 min**	**30 min**	**60 min**	**90 min**	**120 min**
anisole	0	1	5	24	41
cresol	0	28	79	124	174
cyclohexanol	0	0	7	32	27
methylcyclohexanol	0	0	1	5	7
phenol	1118	1040	926	853	569
xylenol	0	0	2	7	24

phenol, 50 mg Cu20PMO, 290 °C					
compound	**0 min**	**30 min**	**60 min**	**90 min**	**120 min**
anisole	0	2	17	38	56
cresol	0	51	116	170	194
cyclohexanol	0	0	20	62	107
methylcyclohexanol	0	0	3	14	28
phenol	1265	1209	950	876	692
xylenol	0	1	5	12	19

phenol, 50 mg Cu20PMO, 300 °C					
compound	**0 min**	**30 min**	**60 min**	**90 min**	**120 min**
anisole	0	4	41	74	86
cresol	0	51	148	172	148
cyclohexanol	0	0	81	245	287
methylcyclohexanol	0	0	20	66	97
phenol	1070	991	859	561	304
xylenol	0	1	10	17	20

phenol, 50 mg Cu20PMO, 310 °C					
compound	**0 min**	**30 min**	**60 min**	**90 min**	**120 min**
anisole	0	7	46	84	94
cresol	0	66	144	181	105
cyclohexanol	0	2	106	297	296
methylcyclohexanol	0	1	31	113	179
phenol	1055	952	687	413	106
xylenol	0	2	11	23	24

phenol, 50 mg Cu20PMO, 320 °C					
compound	**0 min**	**30 min**	**60 min**	**90 min**	**120 min**
anisole	0	22	67	102	104
cresol	0	82	146	141	87
cyclohexanol	0	12	157	314	303
methylcyclohexanol	0	6	61	210	296
phenol	961	835	472	164	52
xylenol	0	4	15	30	29

C7: Summary of rate constants (hr^{-1}) for the conversion of phenol

Summary of rate constants (hr^{-1}) for the conversion of PHE over the copper-doped porous metal oxide catalyst at 280-320 °C for up to 120 min. These include hydrogenation k_{HYD}, O-methylation k_{OMe}, and aryl methylation k_{AMe} (3 mL MeOH, 50 mg Cu20PMO, 20 μL decane, 1 mmol substrate).

Temp (°C)	280	290	300	310	320	Ea
k_{HYD} (hr^{-1})	0.023 ± 0.016	0.088 ± 0.013	0.27 ± 0.042	0.41 ± 0.14	0.70 ± 0.16	228 ± 30
k_{OMe} (hr^{-1})	0.023 ± 0.016	0.054 ± 0.013	0.059 ± 0.042	0.084 ± 0.057	0.12 ± 0.069	109 ± 17
k_{AMe} (hr^{-1})	0.12 ± 0.016	0.16 ± 0.013	0.19 ± 0.079	0.27 ± 0.15	0.28 ± 0.17	61 ± 6.1

C8: Analysis of product mixtures from reactions of dihydrobenzofuran

Analysis of product mixtures from the reaction of 2,3-dihydrobenzofuran (DHBF) over the copper-doped porous metal oxide catalyst at 290-330 °C for longer experimental runs (up to 18 h). Conditions: 3.0 mL MeOH, 50 mg Cu20PMO, 20 μL decane, 1 mmol substrate. Temporal evolution of the product mixture reported in μmol and calculated from response area of the GC-FID peaks and calibrated against decane as an internal standard. See chapter 2 for further details of the analytical methods.

1 mmol DHBF, 50 mg Cu20PMO, 290 °C								
compound	**0h**	**1h**	**2h**	**3h**	**4h**	**6h**	**12h**	**18h**
2-ethylcyclohexanol	0	0	7	17	27	52	171	228
2-ethylphenol	0	13	17	49	56	70	84	87
DHBF	1242	1222	1136	891	882	768	554	523
ethylbenzene	0	0	0	13	25	49	132	112
ethylcyclohexane	0	0	0	0	0	0	6	12

1 mmol DHBF, 50 mg Cu20PMO, 300 °C								
compound	**0h**	**1h**	**2h**	**3h**	**4h**	**6h**	**12h**	**18h**
2-ethylcyclohexanol	0	3	7	20	40	110	206	272
2-ethylphenol	0	1	29	67	71	95	94	53
DHBF	1163	1155	969	860	761	719	586	296
ethylbenzene	0	0	0	21	34	80	131	227
ethylcyclohexane	0	0	0	0	0	0	7	21

1 mmol DHBF, 50 mg Cu20PMO, 320 °C								
compound	**0h**	**1h**	**2h**	**3h**	**4h**	**6h**	**12h**	**18h**
2-ethylcyclohexanol	0	10	105	184	204	229	433	457
2-ethylphenol	0	34	118	104	90	64	46	23
DHBF	1261	1213	908	586	537	410	141	41
ethylbenzene	0	0	56	135	153	206	342	371
ethylcyclohexane	0	0	0	6	6	13	53	91

1 mmol DHBF, 50 mg Cu20PMO, 330 °C								
compound	**0h**	**1h**	**2h**	**3h**	**4h**	**6h**	**12h**	**18h**
2-ethylcyclohexanol	0	55	143	204	300	299	568	651
2-ethylphenol	0	83	105	61	58	53	28	35
DHBF	1054	992	652	350	227	297	37	13
ethylbenzene	0	30	98	206	263	290	389	400
ethylcyclohexane	0	0	4	17	29	28	92	142

C9: Summary of rate constants (hr^{-1}) for the conversion of dihydrobenzofuran

Summary of rate constants (hr^{-1}) for the conversion of DHBF over the copper-doped porous metal oxide catalyst at 280-320 °C for up to 18 h. (3 mL MeOH, 50 mg Cu20PMO, 20 μL decane, 1 mmol substrate).

Temp (°C)	290	300	320	330	Ea
k_{HDG} (hr^{-1})	0.068 ± 0.008	0.078 ± 0.008	0.21 ± 0.02	0.31 ± 0.04	113 ± 13
2-ethylphenol hydrogenation (hr^{-1})	0.19 ± 0.1	0.22 ± 0.1	0.59 ± 0.2	0.90 ± 0.3	115 ± 12
2-ethylphenol HDO (hr-1)	0.14 ± 0.1	0.17 ± 0.1	0.47 ± 0.1	0.66 ± 0.2	118 ± 11

C10: Analysis of methanol conversion and gas mixtures from the reaction of methanol

Analysis of methanol conversion and gas mixtures from the reaction of methanol (MeOH) over the copper-doped porous metal oxide catalyst at 280-320 °C for experimental runs up to 195 min. Conditions: 3.0 mL MeOH, 50 mg Cu20PMO. Total volume of reaction gas at atmospheric pressure and room temperature (mL) as determined by water displacement apparatus (SI figure S1). MeOH conversion in mmol based off of total mass lost to gasses. Temporal evolution of the product mixture reported in mmol of gas from response area of the GC-TCD.

3 mL MeOH, 50 mg Cu20PMO, 280 °C							
time (min)	**15**	**45**	**75**	**105**	**135**	**165**	**195**
gas volume (mL)	0	20	95	150	210	250	285
MeOH converted	0.12	0.53	1.40	2.09	2.93	3.40	3.96
hydrogen	0.00	0.25	1.93	4.23	6.02	6.38	6.70
carbon monoxide	0.00	0.01	0.30	0.98	1.98	2.49	2.99
methane	0.00	0.00	0.00	0.01	0.03	0.05	0.07
carbon dioxide	0.01	0.06	0.31	0.47	0.58	0.66	0.85

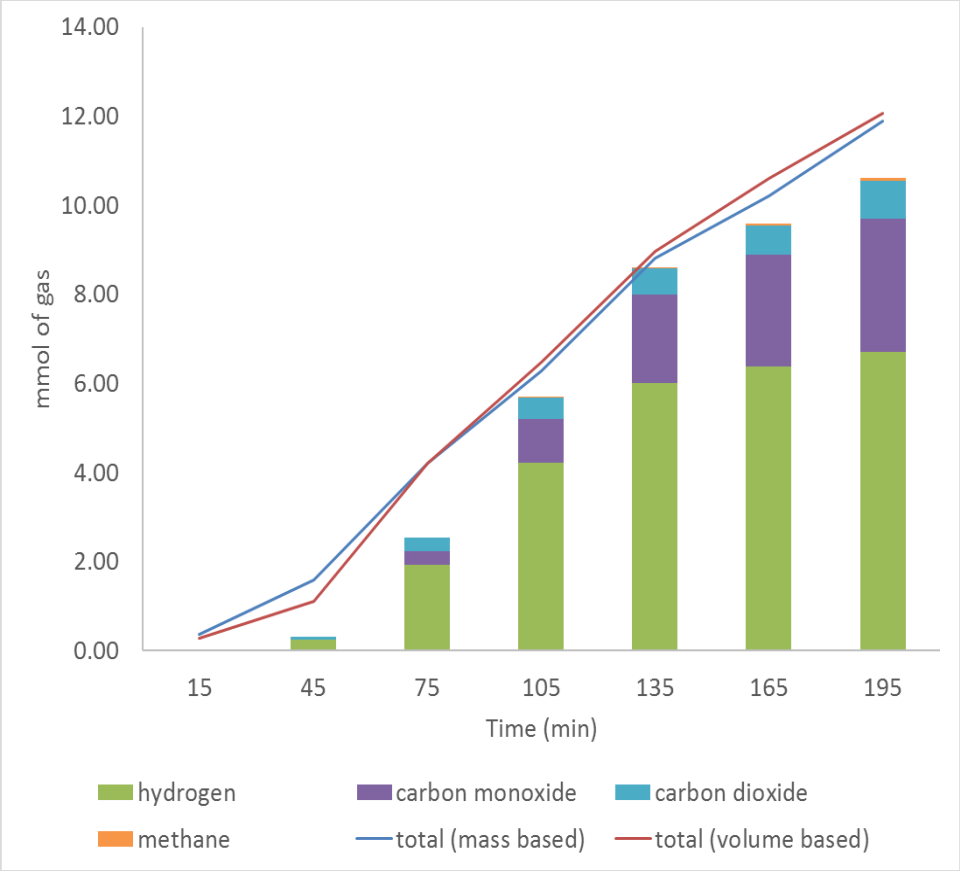

3 mL MeOH, 50 mg Cu20PMO, 290 °C							
time (min)	**15**	**45**	**75**	**105**	**135**	**165**	**195**
gas volume (mL)	0	55	135	230	300	330	355
MeOH converted	0.00	0.62	1.81	3.15	3.90	4.68	--
hydrogen	0.00	1.08	3.54	6.28	7.46	8.81	7.64
carbon monoxide	0.01	0.06	0.75	2.17	3.34	4.18	3.81
methane	0.00	0.00	0.01	0.03	0.07	0.11	0.13
carbon dioxide	0.01	0.21	0.47	0.74	0.84	1.13	1.18

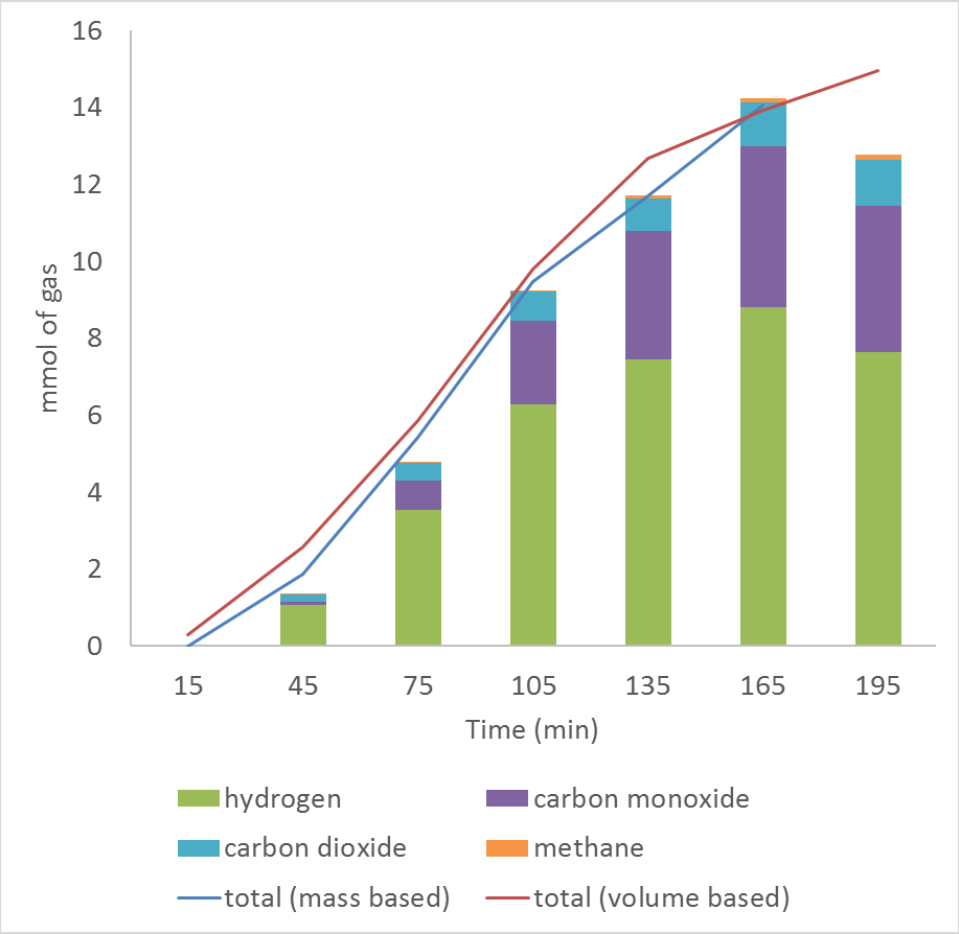

3 mL MeOH, 50 mg Cu20PMO, 300 °C							
time (min)	**15**	**45**	**75**	**105**	**135**	**165**	**195**
gas volume (mL)	0	110	255	360	410	440	460
MeOH converted	0.00	1.37	3.59	5.06	6.24	6.18	6.71
hydrogen	0.00	3.21	5.70	9.26	7.81	11.76	12.19
carbon monoxide	0.01	0.52	2.80	4.88	4.94	6.29	5.86
methane	0.00	0.01	0.05	0.14	0.18	0.28	0.29
carbon dioxide	0.00	0.31	0.74	1.29	1.24	1.89	1.29

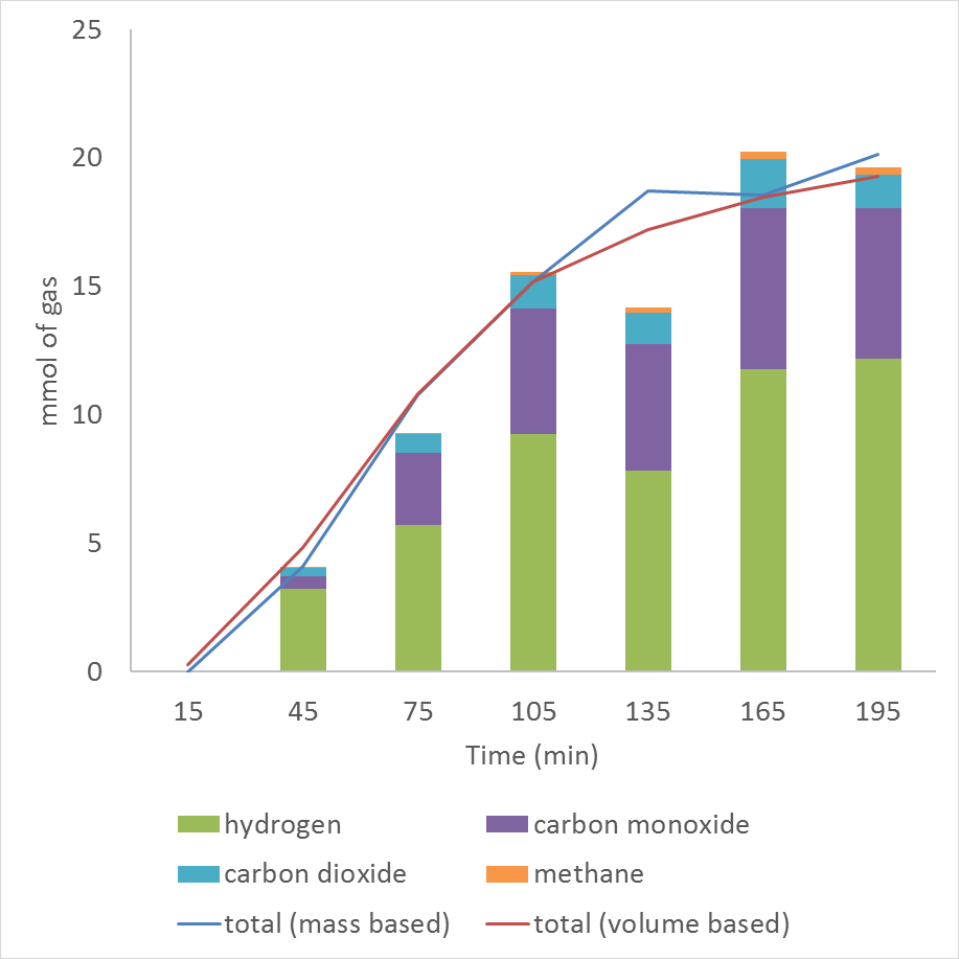

3 mL MeOH, 50 mg Cu20PMO, 310 °C							
time (min)	**15**	**45**	**75**	**105**	**135**	**165**	**195**
gas volume (mL)	0	140	310	420	475	510	530
MeOH converted	0.19	1.50	4.40	6.18	6.74	6.77	7.99
hydrogen	0.00	3.87	7.97	8.74	10.45	13.43	12.66
carbon monoxide	0.01	0.85	4.18	5.13	6.66	6.50	6.81
methane	0.00	0.01	0.10	0.18	0.34	0.31	0.50
carbon dioxide	0.01	0.33	1.62	2.07	3.10	1.29	3.82

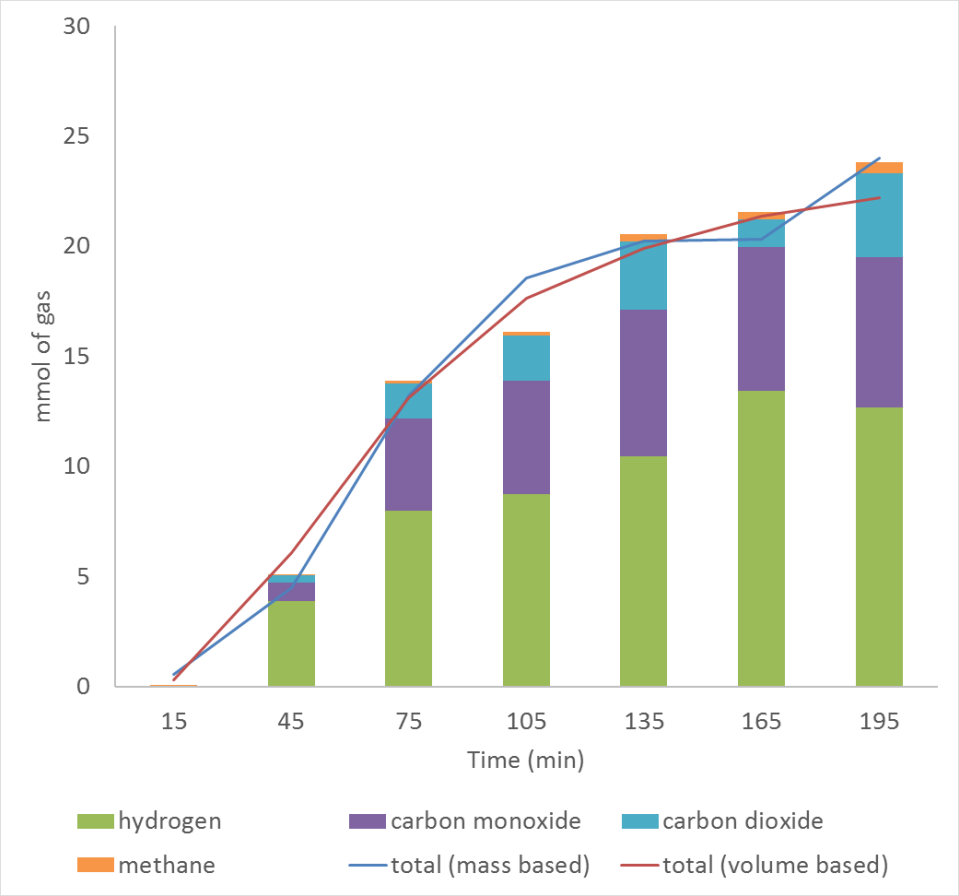

3 mL MeOH, 50 mg Cu20PMO, 320 °C						
time (min)	**15**	**45**	**75**	**105**	**135**	**195**
gas volume (mL)	0	180	370	485	545	570
MeOH converted	0.00	2.22	5.59	6.84	8.02	8.99
hydrogen	0.00	4.88	8.15	12.97	15.42	13.03
carbon monoxide	0.00	1.52	5.22	6.73	7.42	6.38
methane	0.00	0.02	0.16	0.23	0.35	0.45
carbon dioxide	0.01	0.41	2.47	1.20	1.42	1.63

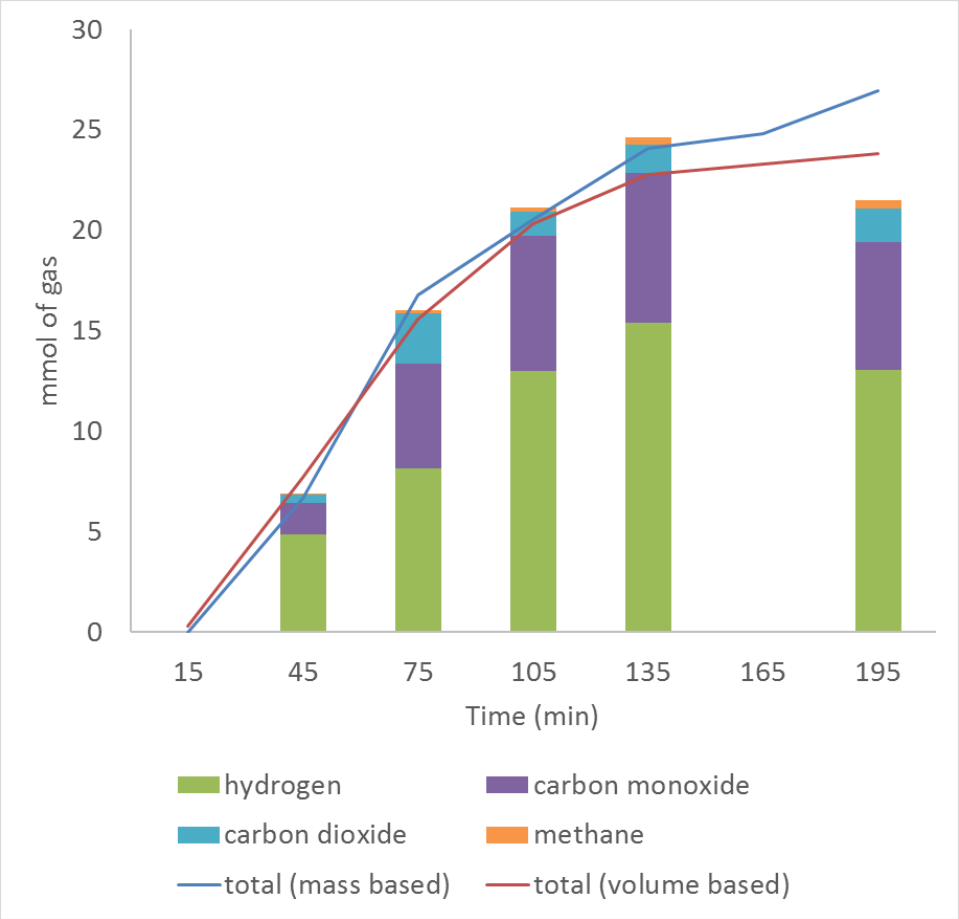

Appendix D – Supplemental Information for Chapter V

D1: Diameters and exciton peak maxima for the various QDs and QD conjugates

Exciton peak maxima for the various QDs and QD conjugates investigated as well as the diameters estimated by Jasieniak et al[*] based on the exciton absorption peak of the QDs with native ligands.

QD Sample	*Exciton peak of QD (nm)*	*Exciton peak of QD-DTO (nm)*	*Exciton peak of QD-tbuDTO (nm)*	*Estimated QD diameter (nm)*
1	509	530	523	2.5
2	513	535	533	2.6
3	551	590	*	3.2
4	554	595	*	3.3
5	580	595	*	3.9

* No data collected

[*] J. Jasieniak, L. Smith, J. van Embsen, P. Mulvaney, "Re-examination of the size- dependent absorption properties of CdSe quantum dots" *J.Phys. Chem. C.* **2009**, *113*, 19468-19474

D2: Spectral changes of DTO under 365 nm irradiation

Absorption spectra changes of DTO in 50 mM sodium borate buffer (pH 9) under 365 nm irradiation over the course of 500 s at 120 s intervals. The quantum yield of DTO decomposition under these conditions was measured to be 0.37±0.06 %.

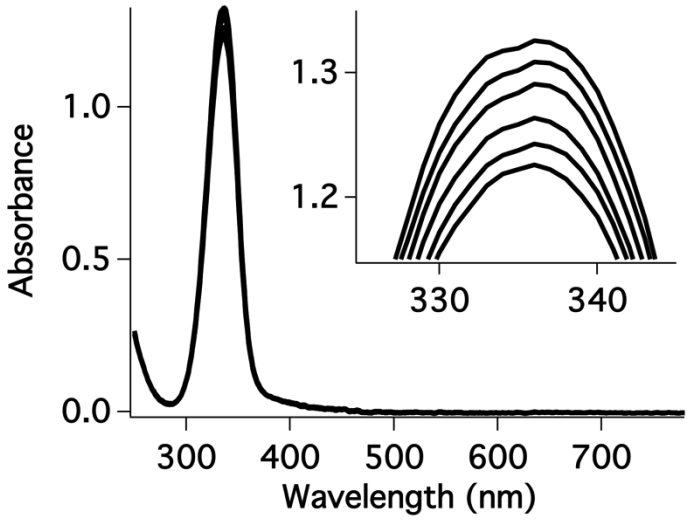

D3: Spectral changes for DTO-QD_{551} during phtolysis at 498 nm

Spectral changes for DTO-QD_{551} conjugates in aerated buffer solution during photolysis with a focused 10 mW LED centered at 498 nm. *Top*: Absorption spectra of DTO-QD_{551} over the course of 15 min. (5 min intervals) irradiation showing the bleach of the DTO peak at 335 nm (ϕ_{dis} = 0.033). The decrease in absorption was accompanied by precipitation of QDs. *Bottom*: Corresponding PL changes during the same 15 min. photolysis. Dotted line represents the completely quenched PL prior to photolysis. Minimal photoluminescence was detected after the first 5 min of photolysis (not shown): however, the PL dramatically increased after 10 and 15 min. photolysis, when ~90 percent of the DTO had decomposed.

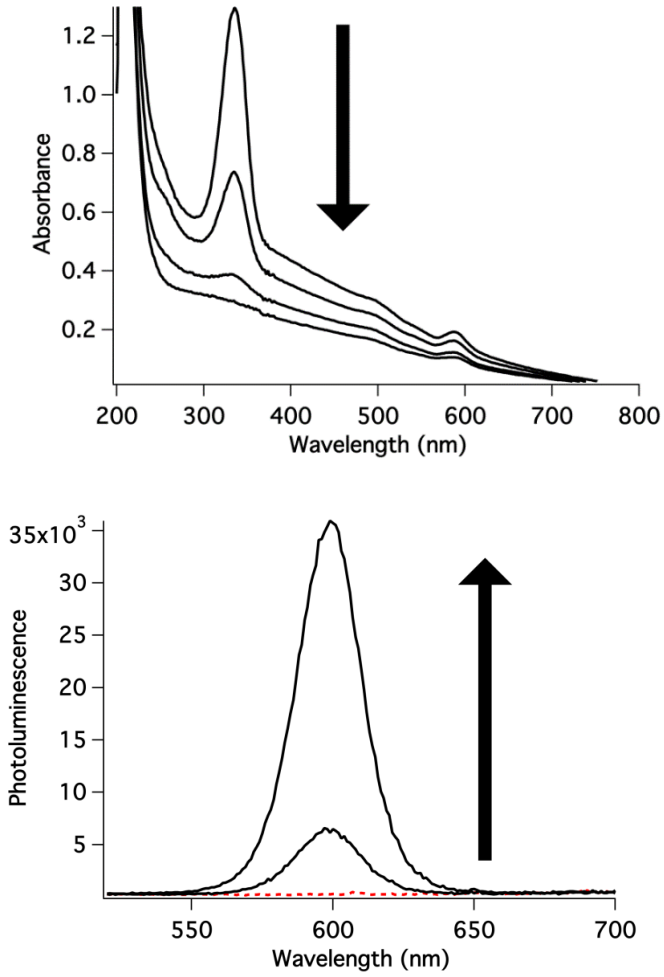

D4: Photolysis QD509-DTO conjugates in the presence of excess DTO

Photolysis QD_{509}-DTO conjugates in the presence of excess DTO in sodium borate buffer (pH 9) upon 498 nm irradiation from a UV lamp. Within 50 minutes, the DTO peak at 335 nm lost 96% of its intensity, suggesting the QDs catalytically accelerated the DTO decomposition.